NMR AND MUSHROOMS

imaging post harvest senescence

1ste promotor :	prof. dr. T.J. Schaafsma
	hoogleraar in de moleculaire fysica
	Wageningen Universiteit
2de promotor :	prof. dr. L.J.L.D. Van Griensven
	hoogleraar in de mycologie
	Katholieke Universiteit Nijmegen
Co-promotor	dr. H. Van As
	universitair hoofddocent verbonden aan het
	Departement Biomoleculaire Wetenschappen

H.C.W. Donker

NMR AND MUSHROOMS

imaging post harvest senescence

Proefschrift
ter verkrijging van de graad van doctor
op gezag van de rector magnificus
van Wageningen Universiteit,
dr. C.M. Karssen,
in het openbaar te verdedigen
op woensdag 8 december 1999
des namiddags te vier uur in de Aula.

ISN 972187

Stellingen

1. De functie van koolstofdioxide bij de knopvorming van champignons vraagt nader onderzoek.

   Flegg, P.B., Spencer, D.M. & Wood, D.A. (eds.); The biology and technology of the cultivated mushroom; John Wiley & Sons, Chichester (1985), p71, p158.

2. Ten onrechte wordt door Millard et. al. een fysiologische interpretatie gegeven aan T_2 waarden die verkregen zijn uit NMR-imaging experimenten.

   Millard, M.M., Veisz, O.B., Krizek, D.T. & Line, M.; Thermodynamic analysis of the physical state of water during freezing in plant tissue, based on the temperature dependence of proton spin-spin relaxation; Plant Cell Environ. (1996); 19: 33-42.

3. Het analyseren van het verval van NMR signalen met behulp van een som van exponentiële functies zonder voorkennis van het monster of de experimentele methode is als het vergelijken van de vorm van een champignon met die van een nucleaire explosie.

4. Het sommeren van exponenten is een éénrichtings functie wanneer het aantal samenstellende exponenten onbekend is en daarom geschikt voor cryptografische toepassing.

5. De opdracht van Lord Baden-Powell of Gilwell om de wereld beter achter te laten dan zij aangetroffen wordt, wordt binnen scouting slechts op één, onbaatzuchtige, manier uitgelegd.

   Lord Baden-Powell of Gilwell; The last message; in: Scouting for boys, C. Arthur Pearson Ltd., London (1947), p. 220.

6. De kwaliteit van wetenschappelijke publicaties is te verhogen indien de namen van de auteurs van een manuscript niet aan de beoordelende referent bekend gemaakt worden.

7. Vertrouwen op computers voor cruciale berekeningen of data-opslag is niets anders dan het in den blinde delegeren van verantwoordelijkheden aan onbekende programmeurs en systeem ontwikkelaars die onvoldoende doordrongen zijn van de waarde van die berekeningen of data.

8. Een belangrijke oorzaak van het fileprobleem is het prevaleren van het belang van het individu boven het belang van de samenleving.

9. Ervaring komt alleen dan wanneer eerst daarvoor de noodzaak bestaan heeft.

H.C.W. Donker
NMR and Mushrooms, imaging post harvest senescence
Wageningen, 8 december 1999.

The road goes ever on
Down from the door where it began.
Now far ahead the road has gone,
And I must follow, if I can,
Pursuing it with eager feet,
Until it joins some larger way
Where many paths and errands meet.
And whither then? I cannot say.

The road goes ever on
Down from the door where it began.
Now far ahead the road has gone,
Let others follow it who can!
Let them a journey new begin.
But I at last with weary feet,
Will turn towards the lighted inn,
My evening-rest and sleep to meet.

The road goes ever on
Down from the door where it began.
Still round the corner there may wait
A new road or a secret gate;
And though I oft have passed them by,
A day will come at last when I
Shall take the hidden paths that run
West of the moon, east of the sun.

free after Bilbo Baggins

ter nagedachtenis aan opa

VOORWOORD

Voor u ligt het proefschrift dat ik schreef na een periode van 4 jaar bij de vakgroep Moleculaire Fysica van de Landbouw Universiteit te Wageningen en in menig avond-uurtje daarna. Dit proefschrift kwam niet zomaar tot stand. Veel ondersteuning kwam van collega's, vrienden en familie, van wie ik graag een paar bij naam wil noemen.

Tjeerd Schaafsma wil ik danken voor de begeleiding van het project. Tjeerd wist in de schaarse momenten van overleg meer creatieve gedachten aan te reiken dan ik in weken zelf bedacht kon hebben.

Henk Van As wil ik bedanken voor zijn nimmer aflatend luisterend oor. Ik kon altijd een beroep op Henk doen, hetgeen ik zeer gewaardeerd heb. Hij wist met een paar woorden meestal direct tot de kern van een probleem door te dringen om daar dan enthousiast mee aan het werk te gaan.

Wat meer op afstand, maar daarom niet minder waardevol was de samenwerking met professor Van Griensven van het Proefstation voor de Champignoncultuur. Van hem kwam altijd een kritische noot wanneer het over de fysiologie van de champignon ging.

Hommo Edzes is een grote stimulans geweest in het project met zijn grondige kennis van de 20 MHz imager en de bijbehorende software. Arnold Jans heeft in de beginperiode het projekt begeleid. Helaas mocht hij het einde van het project niet meer mee maken. Hij wist altijd op creatieve wijze voorwaarden te scheppen die anders nog wel eens moeilijk gerealiseerd hadden kunnen worden.

En dan zijn er alle collega's die met hun aanwezigheid mijn tijd op de vakgroep tot een aangename tijd gemaakt hebben; in het bijzonder Wybo Palstra, Angelien Snaar, Shirley van der Wiel, Marc Polm, Dagmar van Dusschoten en Arjan Snijder.

Buiten de L.U.W. heb ik altijd met veel plezier met diverse mensen samengewerkt. In het begin met Fred Huf, die nauw betrokken is geweest bij het opzetten van het project en later met Bram Boekestein en Arjan Lommen. De laatste drie zijn verbonden aan het RIKILT, waar ook de essentiële financiële middelen vandaan kwamen om dit onderzoek uit te kunnen voeren. Naast de samenwerking met het RIKILT dient ook de samenwerking met het ATO niet onvermeld te blijven. Arnold Braaksma maakte dat ik op diverse facetten van het project een adequate gesprekspartner in het ATO vond.

Mijn ouders hebben me altijd met raad en daad bijgestaan. Zij weten welke lijdensweg het schrijven van een proefschrift kan zijn, omdat ze het van zo dichtbij meegemaakt hebben. Zonder jullie nimmer aflatende steun was dit proefschrift waarschijnlijk niet ontstaan.

Als laatste wil ik Mariska bedanken. De afgelopen jaren waren voor mij soms moeilijke jaren maar bij jou vond ik menig maal de rust om weer verder te gaan. Bovendien wist je me vaak te overtuigen van de betrekkelijkheid van mijn werk. Ik hoop daar nog lang van te mogen genieten.

Iedereen heel hartelijk bedankt.

Hank Donker

ISBN 90-5808-136-2

Reprinted from:

Post Harvest Biology and Technology, 10, H.C.W. Donker & A. Braaksma, Changes in metabolite concentrations detected by ^{13}C-NMR in the senescing mushroom (*Agaricus bisporus*), Pages No. 127-134, Copyright (1997),

Magnetic Resonance Imaging, 14, H.C.W. Donker, H. Van As, H.T. Edzes & A.W.H. Jans, NMR Imaging of white button mushroom (*Agaricus bisporus*) at various magnetic fields, Pages No. 1205-1215, Copyright (1996),

Magnetic Resonance Imaging, 15, H.C.W. Donker, H. Van As, H.J Snijder & H.T. Edzes, Quantitative ^{1}H-NMR imaging of water in white button mushrooms (*Agaricus bisporus*), Pages No. 113-121, Copyright (1997)

and

Biochimica et Biophysica Acta, 1427, H.C.W. Donker & H. Van As, Cell water balance of white button mushrooms (*Agaricus bisporus*) during its post-harvest lifetime studied by quantitative magnetic resonance imaging, Pages No. 287-297, Copyright (1999),

with permission from Elsevier Science.

CONTENTS

1 INTRODUCTION

APPLICATION OF NMR AND NMR-IMAGING TO POST-HARVEST PHYSIOLOGY OF *AGARICUS BISPORUS*

1.1 Aims and goals of the Thesis research

The mushroom *Agaricus bisporus* is known for its traditional human consumption. Although the absolute production volume is more or less stable at present, other fungi enter the consumer market and become serious competitors. This intensifies the need to control post-harvest quality deterioration of this fragile agricultural crop. Since quality deterioration of mushrooms is hard to monitor and strongly related to the water distribution, this work attempts to use Nuclear Magnetic Resonance and Magnetic Resonance Imaging (NMR/MRI) techniques to investigate deteriorating mushrooms after harvest. This has to result either in the possibility to apply MRI as a reference technique for fast screening methods of mushrooms, which can be used at auctions for quality control or in the laboratory for strain improvement. Since the application of NMR/MRI techniques is new in the field of quality studies on mushrooms, the possibilities of the technique are explored, aimed at the quantitative understanding of the observed NMR data and insight in the influences of the physiology of the mushroom on the obtained data.

In the this Chapter, a brief introduction to both the physiology of a senescing mushroom and the application of NMR/MRI in plant studies is presented.

1.2 Physiology of Agaricus bisporus

1.2.1 History

> This plant is of so very singular a growth and temperature, that unless a proper idea of its nature and habit is attained and the peculiar methods and precautions pursued in the process of its propagation and culture, little success will ensue.
> The whole management of it remarkably differs from that of every other species of the vegetable kingdom; and it is most liable of any to fail without a very strict observance and care in the different stages of its cultivation.
>
> Abercrombie 1779

These warning lines appeared in 1779 in the introduction of John Abercrombie's treatise on the nature and cultivation of the garden mushroom. He was one of the firsts to describe the commercial production of mushrooms (1).

Mushrooms were cultivated outdoors until 1810, when a French gardener, Chambry, began to cultivate mushrooms in underground quarries in Paris. He thus introduced a production system, which produced the entire year. In Germany, mushrooms were grown in specially constructed houses 'warmed by fire-heat'. Such an environment was too dry for successful growing of mushrooms as a commercial crop, however.

It is generally accepted that protected cropping of mushrooms was pioneered in caves in France. However, the forerunners of modern mushroom houses were developed in England. Mushroom production quickly became established in various countries of Europe and soon spread to the USA. Large scale mushroom production is now centred in Western Europe and in North America. In South-East Asia, especially China, South Korea and Taiwan, many small enterprises together produce a vast amount of mushrooms.

Cultivation of mushrooms in the Netherlands developed after 1945, starting in caves in the south of Limburg. At that time, the productivity was extremely low and the prices were high, making mushroom growing economically interesting. Decreasing prices and failing production conditions caused the initial expansion to stop.

However, this period laid the foundation for the development of mushroom growing in the Netherlands later this century, characterised by well organised co-operative compost and casing production, an adequate educational system and facilities for applied research.

After 1967, mushroom growing in the Netherlands focused mainly on producing mushrooms for industrial purposes. The preserving-industry exported mainly to Western Germany. Alternative consumer markets were explored for the fresh product since 1985, because competition from Asian mushroom producing countries intensified. By the year 1988, the annual production in the Netherlands had grown to $120*10^6$ kg. During the years 1985-1995 mushroom production in the Netherlands increased with an average annual growth rate of 8%. In 1998, about $250*10^6$ kg of mushrooms was produced in the Netherlands. Until 1991, this growth was mainly realised by increasing the cropping area, later by intensifying of the cropping cycle due to the introduction of bulk processes in the production of compost (2).

A diversification in the production of edible fungi has come up during the past years. Together with an increasing consumer's quality awareness, it is expected that diversification of the mushroom industry will continue in many other western countries and the United States.

Because of rapid deterioration of the crop quality during storage, there is increasing need for more knowledge of the product. Until now, this knowledge was fragmentary and mainly focused on the growing conditions (1,3-11).

Knowledge of post-harvest senescence of the sporophore (Fig. 1) is essential in order to produce an export product of a guaranteed quality and/or process mushrooms with minimal losses due to deterioration.

1.2.2 Taxonomy

By far the most important commercially grown fungus in the Netherlands is *Agaricus bisporus*. This fungus is part of the class *Basidiomycetes* (12). Together with the *Ascomycetes* they form the group of "higher" fungi which contains almost all the fungi cultivated for the production of sporophores or fruitbodies (Fig. 1). The distinction between these two classes of fungi is based on the way spores are

produced. The *Ascomycetes* form spores in sack-like structures, the asci, which eventually excrete spores at full maturity. The *Basidiomycetes* however grow their spores on the basidia (Fig. 1), full-sized cells with tubular structures, which usually develop four spores.

Most edible fungi belong to one of the genera included in the taxonomical order of the Agaricales. The *Basidiomycetes* are differentiated according to the structure and localisation of the basidia. Normally a basidium carries four spores. *Agaricus bisporus* carries only two mostly heterokaryotic spores per basidium (Fig. 1), thereby giving the species its name.

From our point of view the genus *Agaricus* is by far the most important, because it contains the species *Agaricus bisporus*, the common white button mushroom, which is the object of research of this Thesis.

1.2.3 Normal life-cycle

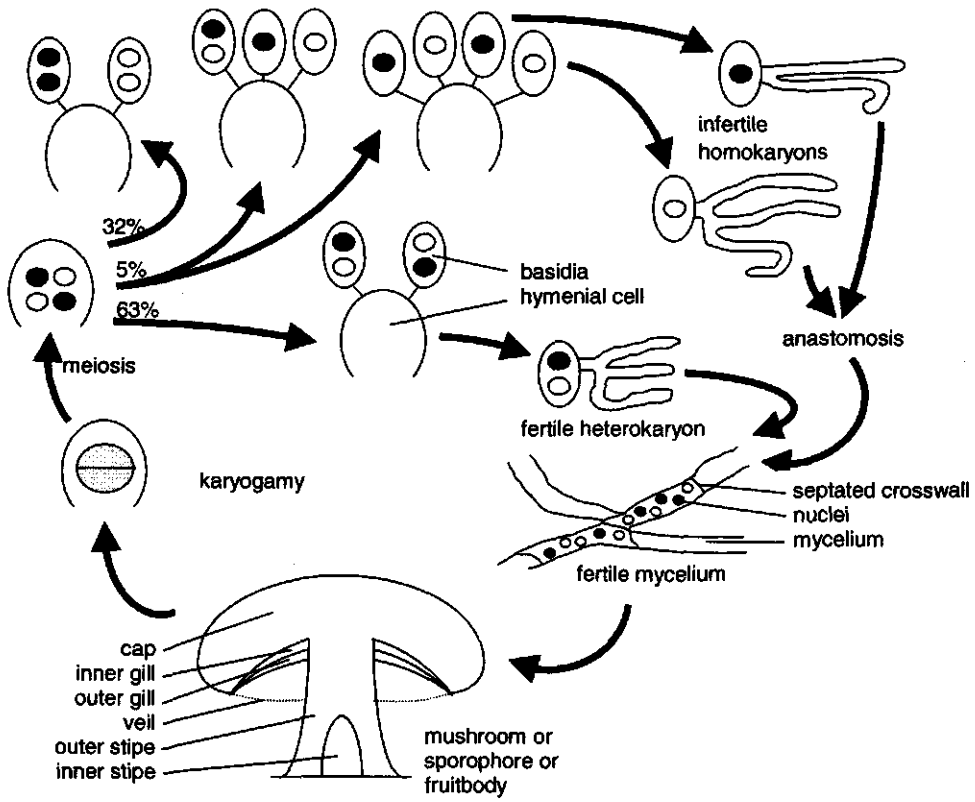

Figure 1, Life-cycle of *Agaricus bisporus* taking into account both random migration of nuclei and typical frequencies of aberrant basidia (1).

The commercial interest in *Agaricus bisporus* is focused only on one stage in the life cycle of this fungus: the formation of fruitbodies. The formation of fruitbodies or sporophores in the casing soil on the mycelium overgrown substrate is induced by changing climatic conditions. The major function of the fruitbody is shedding of spores for reproduction. The description of the life cycle is started with spore germination (1,13-15).

Spore germination seems a rather inefficient process. *In vitro* it will only take place if sufficient spores are present on a virgin substrate or in the presence of specific volatile compounds, like isovaleric acid (14,16,17). In evolutionary terms, the survival value of this dependence presumably lies in the fact that whole ranges of different fungi produce the necessary volatiles for spore germination. This makes *Agaricus bisporus* spore germination independent of substrate already overgrown by *Agaricus bisporus* mycelium (1). Under production conditions, increased CO_2 concentration often suffices for spore germination.

From the germinated spores, mycelium develops. Mycelial growth is apical over its substrate and, in the wild, subjected to all sorts of constraints, ranging from physical barriers to biological barriers like competition by micro-organisms. Mycelium consists of radially growing hyphal filaments, which cover the substrate.

Because fungi are stricktly heterotrophic, metabolic requirements have to be obtained from organic substrates particularly consisting of a composted mixture of wheat straw and horse manure. Four classes of chemical compounds are required for fungal growth:

- Carbon compounds, often monomeric or polymeric sugars,
- Nitrogen compounds, either inorganic or organic,
- Essential inorganic elements, like phosphorus, potassium and iron,
- Vitamins such as thiamine and biotin.

The fungus *Agaricus bisporus* is able to convert polysaccharides like cellulose and hemicelluloses into monosaccharides, which can be used as metabolic resources. For this purpose, the hyphae excrete endocellulase, xylanase and proteases. These enzymes break down xylan, pectin, and other polysaccharides to monosaccharides (15,18-22). However before these polysaccharides can be converted, lignine has to be broken down. The question is still open whether those enzymes are produced by the mycelium itself or by bacteria or other fungi.

Nitrogen can both be supplied as inorganic or organic nitrogen sources, such as urea, ammonium salts, alanine, asparagine, glycine and glutamine. Nitrate can not be used as a nitrogen source (1,23,24). The other essential inorganic elements required for fungal growth of *Agaricus bisporus* can be separated in micro- and macro-nutrients. The macro-nutrients are needed at concentrations $\geq 10^{-3}$ M in the substrate. These elements are potassium, phosphorus, magnesium, sulphur and calcium. The micro-nutrients, which are needed in concentrations $\leq 10^{-6}$ M in the substrate, are iron, copper, manganese, zinc and molybdenum. These elements are generally believed to be essential for all kinds of fungi (1,13).

The requirements for vitamins and other essential compounds for mycelial growth are less well understood. On a sterile medium *Agaricus bisporus* needs biotin and thiamine but not sodium pantothenate, nicotinic acid amide or inositol. Since mycelial growth on compost is a symbiotic process, these essential vitamins can also be supplied by micro-organisms present in the compost (11,25-27).

Other essential conditions for optimal mycelial growth are a moisture content of 63%-68%, a pH of 6-7.5, an ammonia concentration of less than 10 ppm and a temperature of 295-298 K (1).

The CO_2 concentration required for optimal mycelial growth is still a matter of scientific debate. Several metabolic pathways for the fixation of CO_2 have already been suggested since *Agaricus bisporus* does not grow at concentrations less than 200 ppm although CO_2 fixation is not to be expected in an organism lacking chloroplasts. The optimal CO_2 concentration for vegetative growth is between 1000 and 5500 ppm. Growing mycelium is likely to require CO_2 to maintain the level of the citric acid cycle intermediates (anaplerotic replenishment). In practice, CO_2 levels are not controlled during vegetative growth.

More elaborate reviews of mycelial growth on either synthetic or commercial substrates are given by Flegg *et al* and Griffin *et al* (1,13).

Primordium formation has been suggested to be induced by the mycelial production of self-inhibitory compounds (1). It takes place on a casing layer placed on top of the compost. The casing layer forms a water barrier for the compost. It is important that the casing layer level and depth are uniform in order to achieve an even growth of the mycelium into the casing. In commercial practice, primordium formation is initiated with a controlled temperature shock caused by ventilation.

After primordia formation is initiated, fruitbodies are grown in flushes. A flush is the simultaneous development of primordia to fully-grown harvestable fruitbodies. Usually three to four flushes can be harvested from the same substrate before exhaustion. Flushes appear at regular intervals of about eight days. The interval between later flushes increases, probably due to partial exhaustion of the substrate (28,29). In two to three days, the primordia develop to mushrooms of about 2.5 cm height and 3 cm cap diameter. These dimensions are acceptable for high quality mushrooms and are therefore ready to be harvested.

The fruitbody of *Agaricus bisporus*, the main subject of this work, is composed of three main regions: stipe, cap and gill. Spores develop on the gill (Fig. 1). The functions of the cap and stipe are subordinate to the function of the gill since the gill is crucial in the shedding of sphores.

In the earliest stage, the primordium has a diameter of about 1 mm (1,30,31), and consists of a densely packed aggregation of hyphae. The hyphae in this stage are randomly oriented and not yet differentiated. When the primordium has reached a diameter of 6 mm, differentiation into the subsequent tissue types has already taken place (32). From this stage onward, the development involves expansion of the cap and gill, maturation of the spores and rapid elongation of the stipe. In the earliest developmental stages, the gill is covered by a veil. This veil allows an undisturbed

development of the gill. When the spores are ready to be shed, this veil breaks and spores are excreted. Breaking of the veil is caused by opening of the cap. In the meantime, the stipe elongates, elevating the cap and gill. Depending on the consumers need, the mushroom is harvested just before or just after breaking of the veil.

When the mushroom is not harvested at this stage, the cap opens to a flat disk of about 6 cm diameter and the stipe stretches to about 7 to 10 cm, though the actual dimensions depend on the cultivating conditions. At this developmental stage, the configuration for spore shedding from the matured gills is optimal. After spore shedding, the fruitbody dies off (33).

1.2.4 Post-harvest physiology

After harvest, the mushroom is deprived of its resources, normally supplied by the substrate, though it is still progammed to excrete spores, as if it had not been harvested. The rate at which it respires, grows and dies off after harvest affects the mushroom quality, determined by the stage of the fruitbody at the moment of harvest (33,34). Therefore, an important objective of studies on the post-harvest physiology of mushrooms has been to determine how the rates of the various physiological changes can be affected to manipulate the quality and shelf life according to the consumers need. This resulted in studies of e.g. the loss of food value (35-38) and off-flavour compounds (39-44).

In general, a clean, wholesome product is required, i.e. a white solid mushroom free from compost and casing material, unblemished and without off-flavours (35,45,46). Mechanical solidity and crispness are of special interest, however the underlying causes of these two quality parameters are barely understood.

Quality deterioration after harvest have been subject of numerous studies, focussing on:

- Post-harvest browning and the role of tyrosinase (47-56),
- Storage conditions (1,57-61),
- The presence Cytokinins (62),
- Diseases and pests, like watery stipe and La France disease (1,63-67),
- Membrane composition and cell wall structure (68-71),
- Accumulation of polyphosphate (72).

Regardless of the stage at which it is picked, a mushroom consists of a mass of hyphae aggregated together to form a fruitbody. The solidity of a fruitbody is the result of its turgidity, the molecular cell-wall structure and the ultrastructure of the object under study. Osmotica and respirative resources are required for all post-harvest processes, which together determine the senescence of the fruitbody. These are in essence processes of starvation, which have the physiological state of the fruitbody at harvest as their reference point (1,33,49,73).

Proteolytic activity has been observed in the harvested mushroom (1,44,60,61,74-77). When the mushroom is deprived of metabolic resources, molecular structures in cell organelles are broken down to form free amino acids. These amino acids can subsequently be respired to supply the mushroom

with energy for gill maturation, spore formation, cap opening and eventually stipe elongation (44,76,78-80). In the harvested fruitbody, some carbohydrates are also present, which can also function as metabolic resources during the post-harvest life of the fruitbody (1,30,81-86).

Figure 2, Structure of the surface of a mushroom cap (1,87,88).

On the other hand, the post-harvest physiology of the fruitbody is strongly affected by its water balance. The aggregated mycelium threads contain from 90 to 93% water and have 25 to 60% free space between the hyphae, as shown in Figure 2 (1,87-92). The extracellular spaces allow this water to evaporate freely, especially since the hyphae are not protected against evaporation of water. The transpiration rates were earlier recognised to be important in the development of a high quality product (93).

The water balance is closely related to the tissue ultrastructure. The interhyphal cavities permit free exchange of water vapour and other gases from the interior of the fruitbody to the surrounding atmosphere. The water vapour in these cavities is in thermodynamic equilibrium with liquid water on the outside of the cell walls, which are hydrophilic (94), as is demonstrated by the concave water surface close to the mushroom and the slow uptake of water of a submerged mushroom. The hydrophilic cell walls together with the changing dimensions of the interhyphal cavities cause capillary uptake of water between the mycelium threads to varying extent, thereby blocking free interchange of gases. It is therefore clear that the water balance and ultrastructure are in a delicate equilibrium, with major effects on the post-harvest senescence.

The hyphae in the outer stipe are oriented along the stipe and closely packed. The hyphae in the cap are randomly oriented and loosely packed. This orientation of the hyphal threads takes place during differentiation of the primordium (32-34). The randomly oriented hyphal threads, which form the cap, originate from the inside of the primordium, whereas the oriented hyphal threads in the outer stipe and the gill are generated from the outer side of the primordium (95). The first stages of cell differentiation

in the primordium are the formation of cavities due to morphogenetic cell death, followed by the formation of the gill (32).

The gill is made up of trama, sub-hymenia and hymenia (95). The trama are an extension of the oriented hyphal threads, originating from the outer stipe and stretch out from the outer stipe to grow down into the gill. Here they differentiate to form the sub-hymenium, which develops into hymenium. The hymenial cells are on the outside of the gills, where they produce the spores on two basidia per hymenial cell (1, 95).

Post-harvest senescence results in the development of various tissue types. In the gill this results in hymenial cells producing spores; in the outer stipe vacuolizing stretching cells are formed, which induce stipe elongation (1,69,70,96), whereas in the cap cell-stretching induces cap opening. Overall, it results in a dying fruitbody with a tissue density of 0.6 to 0.7 g/ml in the outer stipe and gill, and 0.5 g/ml or less in the cap and core of the stipe.

Osmotica are required to attract water to locations where cells stretch to open the cap and elongate the stipe. The upper stipe is known to contain stretching cells. To induce opening of the cap another region with stretching cells has to be present in the fruitbody. This region may be the gill or the region in the cap just behind the gill.

Mannitol is the most abundant metabolite present in the fruitbody of *Agaricus bisporus*, except for water. This compound makes up about 1% of the fresh weight of the fruitbody and is formed from fructose. The equilibrium of this reaction is towards the synthesis of mannitol, especially at high NADP/NADPH ratio's (1,43,97,98). This is the non-starving situation, typical for mycelium in the substrate or the fruitbodies before harvest (1,81,98,99). In the harvested fruitbody, mannitol is likely to have a function in the osmoregulation because of its high abundance. As a carbohydrate, it can also be used as a respirative resource (1,84,98,100,101).

The NADP/NADPH ratio is different for the various parts of the fruitbody. Moreover, the need for osmotic pressure is non-uniformly distributed. The function of mannitol is therefore location-dependent resulting in mannitol gradients (1, 73), induced by differing respiration rates for different parts of the fruitbody.

It depends on the cell compartment in which mannitol is present (most likely the vacuole) and on the permeability of membranes for mannitol whether it can be redistributed (1,73,102). If mannitol itself cannot be redistributed and fructose can, then mannitol can first be oxidised to fructose, which can be transported instead of mannitol. So far, the precise mechanism for the redistribution of mannitol is unknown.

Translocation of respirative resources or osmotica is required, to allow spore excretion (1,74,101). The relation between the distribution of water and metabolites in the senescing fruitbody is not known, however. This work therefore attempts to clarify this relation, using NMR spectroscopy and NMR imaging (MRI). ^{13}C-NMR spectroscopy of extracts is used to study metabolites and ^{1}H-MRI is applied to observe the distribution of water over the fruitbody.

1.3 NMR/MRI applied to plants

1.3.1 Introduction to plant NMR/MRI

The scientific use of *in vivo* Nuclear Magnetic Resonance (NMR) started with the acquisition of a ^{1}H-NMR signal from the finger of F. Bloch in the late 40's (103). NMR soon appeared to be a powerful tool for structural analysis of molecules with a mass of up to several kilo-Dalton's. Later, in the early 1970's, it was realised that, using magnetic field gradients, images of the spatial distribution of nuclear spins could be made (103-105). Especially imaging of the ^{1}H nuclei of water evolved as a novel method for medical imaging. Presently, NMR spectroscopy is routinely applied in a broad range of molecular studies and NMR imaging or MRI (Magnetic Resonance Imaging) is the image building technique of soft tissues in medical examinations. More applications in both fields are presented regularly (103,104,106-120).

Right from the beginning of the development of MRI, agricultural products have always been interesting to image (121). The advantage of agricultural products is the absence of actively moving tissue parts, offering image quality unrestrained by experimental duration. Plants and especially fruits are therefore adequate phantom samples for medical imaging experiments. Their disadvantage is the wide diversity of tissue types even at a cellular level, with all the impacts on image contrast. This resulted in two NMR/MRI plant research lines.

The first line is characterised by the application of manufacturer provided NMR/MRI protocols on harvested crops ("fruit and veg" research, (108)). These investigations are often performed on standard equipment and usually result in snap-shot imaging of morphologies and or pathologies in crops, not too much caring about the attainable MRI contrast. Measurements are often performed by botanists and biologists having good knowledge of the plant tissue under study and trying new imaging techniques.

The second line of NMR/MRI plant research goes to great depth to develop MRI methods suitable for theoretically derived parameter imaging of intact plants, to understand the acquired contrast quantitatively. These investigations are often pursued on dedicated NMR/MRI equipment adapted to plant research purposes and performed by biophysicists and biochemists.

Both research lines are equally valuable to the field, though their mutual understanding can sometimes be poor (108). The remaining part of this introduction gives an overview of both types of work performed in the field of NMR/MRI plant studies preceded by some considerations about NMR spectroscopy on plant tissue. However, before going down into more details, a description of NMR fundamentals, most relevant for this Thesis is presented.

1.3.2 Theoretical background

1.3.2.1 Nuclear spins in a magnetic field

A large number of atomic nuclei have a magnetic dipole moment proportional to their angular momentum with a proportionality constant, known as the gyromagnetic ratio, γ. Solving the Hamiltonian in the presence of an external static magnetic field, $\vec{B}_0$, results in energy levels (103,104,111,122):

$$U = -\gamma\hbar\vec{B}_0 m_I \qquad [1]$$

with $m_I = (-I, -I+1 , -I+2 , ... , -2+I , -1+I , I)$ and $\hbar = 1.0546 \cdot 10^{-34}$ Js .

Nuclei with a nuclear spin quantum number $I = ½$ can orient their magnetic moment either parallel or anti-parallel to an external magnetic field, $\vec{B}_0$. This corresponds to two energy levels, $m_I = \pm ½$ (Fig.3). ^1H and ^{13}C are such nuclei and no other nuclei will be considered in this Thesis ($\gamma = +26.751 \cdot 10^7$ and $+6.7263 \cdot 10^7$ rad T^{-1} s^{-1} respectively).

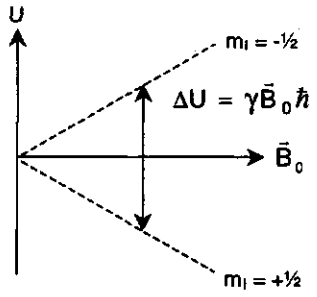

Figure 3, Energy levels $U = \pm\gamma\vec{B}_0 m_I\hbar$ for a nucleus with $I = ½$ and $\gamma > 0$. The transition between the two levels, giving rise to the NMR signal, is indicated by the double arrow.

In the absence of internal magnetic fields, the magnetic moments of the spins precess around the external magnetic field vector $\vec{B}_0$, with the Larmor frequency ω_0 given by:

$$\omega_0 = \gamma \vec{B}_0 = \Delta U / \hbar \qquad [2]$$

Because γ is nucleus specific, so is ω_0.

The distribution of spins over the two energy levels follows the Boltzmann equation:

$$n_- / n_+ = \exp (- \Delta U / kT) \qquad [3]$$

where n_- and n_+ represent the number of spins in either one of the states $m_I = \pm \frac{1}{2}$ in a volume element, k is the Boltzmann constant, $1.381 \cdot 10^{-23}$ JK^{-1}, and T represents the absolute temperature of the sample.

For the many atoms in a sample, magnetic moments of the individual spins add up to macroscopic magnetization $\vec{M}_0$:

$$\vec{M}_0 = (n_- + n_+) \ (\gamma\hbar)^2 \ I(I+1) \ \vec{B}_0 / 3kT \qquad [4]$$

The observed nuclei are surrounded by electrons and other nuclei with non-zero magnetic moments. In addition, the magnetic surrounding of the observed nuclei may be fluctuating due to molecular translational and/or rotational diffusion. Each of these effects influence the local magnetic field at the observed nucleus. To discriminate between pools of nuclei the concept "ensemble" is introduced.

Two (or more) nuclei belong to the same ensemble when they behave identically in an NMR experiment, i.e. when no fundamental NMR parameter has a significantly different value. This is possible when two nuclei experience identical magnetic environments with corresponding time-dependences of this environment. A sample may contain from just one single spin ensemble up to a continuous distribution of ensembles. Each ensemble has a magnetic moment $\vec{M}_0$, which can be manipulated and detected.

If a system is considered in which all spin ensembles have the same Larmor frequency and a $\vec{B}_0$ field is applied with a superimposed field gradient $\vec{G}$, linearly dependent on the position $\vec{r}$, the observed resonance frequencies represent the spatial position of spin ensembles.

$$\omega(r) = \gamma (\vec{B}_0' + \vec{G} \bullet \vec{r}) \qquad [5]$$

where $\vec{r} = \vec{i} \cdot x + \vec{j} \cdot y + \vec{k} \cdot z$ defines the location of the nuclear spins in the sample and $\vec{B}_0'$ now contains the external as well as the internal magnetic fields. Equation 5 is the basis of Magnetic Resonance Imaging (MRI).

1.3.2.2 Creation of detectable magnetisation

$\vec{M}_0$ can be manipulated by applying a second magnetic field, $\vec{B}_1$, perpendicular to $\vec{B}_0$ and oscillating at the Larmor frequency. The $\vec{B}_1$ field causes $\vec{M}_0$ to precess away from the $\vec{B}_0$ direction, thereby creating a component of $\vec{M}_0$ in the x,y-plane perpendicular to $\vec{B}_0$ and rotating with the Larmor frequency ω_0.

If a frame of reference is defined in which the z-axis is parallel with the positive $\vec{B}_0$ direction and the x- and y-axis are thought to rotate around the z-axis with precisely the Larmor frequency and sense of rotation (the so-called rotating frame of reference), the components of $\vec{M}_0$ in the x,y-plane ($\vec{M}_{x,y}$) become stationary in the rotating frame.

Application of a pulsed $\vec{B}_1$ field provides a way to rotate $\vec{M}_0$ with respect to the rotating frame of reference. The possibility to change the number, timing, duration, amplitude and phase of the $\vec{B}_1$ pulses, leads to a wide variation of NMR experiments. $\vec{M}_0$ can thus be manipulated with an almost infinite combination of $\vec{B}_1$ field pulses, called pulse sequences.

Many elaborate pulse sequences have been developed, most of them containing one or more of only two types of $\vec{B}_1$ pulses, a 90° pulse and a 180° pulse (Figure 4). A 90° pulse rotates $\vec{M}$ over 90° around the x- or y-axis in the rotating frame when no other $\vec{B}_1$ pulses have been applied recently (<30 s). A 180° pulse inverts the entire spin system under this condition. $\vec{M}_{x,y}$ can be detected, providing data for further analysis.

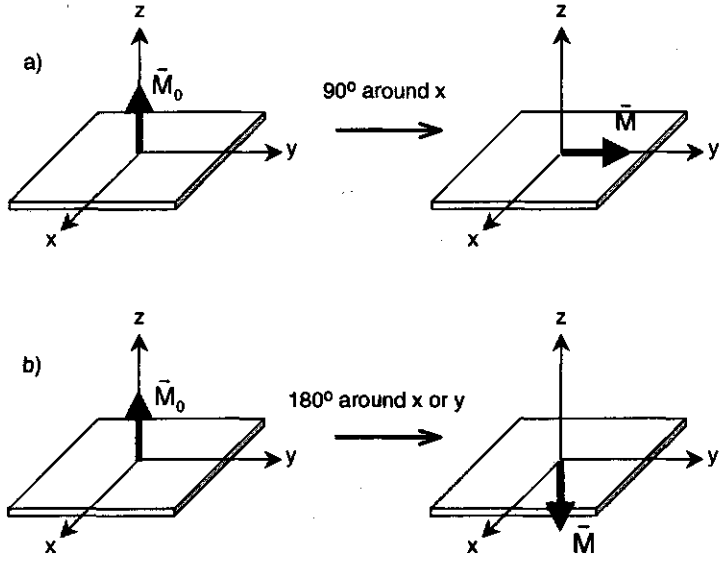

Figure 4, A vector diagram showing the result of the two simplest NMR experiments: a) a 90° pulse along the x-axis and b) a 180° pulse, of a spin ensemble in the rotating frame of reference.

In general, there are three ways to detect $\vec{M}_{x,y}$ i.e. by a free induction decay (fid), a spin-echo and a stimulated echo (104). A free induction decay originates from $\vec{M}_{x,y}$ created by a single 90° pulse; a spin-echo originates from one 90° pulse and one 180° pulse. The 90° pulse creates $\vec{M}_{x,y}$. This magnetisation loses its x,y-coherence. The 180° pulse refocuses this magnetisation, after which it can be detected. A stimulated echo is the result of at least three pulses. The first two pulses create $\vec{M}_z$ magnetisation via $\vec{M}_{x,y}$, where the last pulse, which is usually a 90° pulse, returns this magnetisation back to $\vec{M}_{x,y}$. This technique is used to store $\vec{M}_{x,y}$ at one moment in time for later recall. Stimulated echo's can also be induced by improper tuned pulse sequences and can therefore be unwanted. Full

details of pulse sequences and their variants can be found in standard textbooks (103,104,111). Here it is more important to consider the influences on NMR experiments in experimental practice.

Five parameters are of major importance for the detection of NMR signals:

- spin density, ρ,
  (number of spins per volume element),
- chemical shift, δ,
  (shift of Larmor frequency compared to a reference resonance, expressed in parts pro million),
- spin-spin coupling constant, J
  (splitting of a resonance caused by coupling with one or more other spins),
- spin-lattice relaxation time, T_1,
  (spin lattice or longitudinal relaxation time),
- spin-spin relaxation time, T_2,
  (spin-spin or transversal relaxation time).

The detected signal intensity is proportional to ρ. Under proper measuring conditions, NMR experiments can therefore be quantitative. However, the quantitative information is easily distorted and precise knowledge of the origin of an NMR signal is required for reliable quantification, as will be demonstrated in this Thesis.

The Larmor frequency of spin ensembles is shifted by shielding effects of the electronic environment around the individual nuclear spin. This gives rise to a chemical shift δ, expressed in ppm, resulting in the ability to discriminate spin ensembles by their resonance frequency. NMR spectroscopy of several kinds of nuclei in molecules for structure identification has originated from this principle. Externally applied magnetic $\vec{B}_0$ field gradients also generate a shift of the Larmor frequency. This shift forms the basis for MRI according to equation 5.

Spin-spin coupling is of major importance in NMR. Spin-spin interactions can be either directly through space or via one or more chemical bonds and modulate the resonance frequencies of spin ensembles. These correlations can provide essential information for structure elucidation of (bio-) molecules. For protons in a water molecule, spin-spin coupling vanishes because the protons in the water molecule are identical.

T_1 and T_2 relaxation require a more thorough description in the context of this Thesis. Two paragraphs are therefore presented to describe the phenomenon relaxation and to describe relaxation in the context of plant imaging.

1.3.2.3 Nuclear magnetic resonance relaxation

When $\vec{M}_{x,y}$ has been created and the $\vec{B}_1$ field is switched off, the spin system starts to return to the equilibrium state by relaxation. Relaxation of spins can be distinguished as relaxation parallel to $\vec{B}_0$, with a characteristic relaxation time T_1, the longitudinal or spin-lattice relaxation time and a relaxation time T_2, the transversal or spin-spin relaxation time, perpendicular to $\vec{B}_0$. T_1 relaxation represents the

in-growth of the magnetisation $\bar{M}$ along the positive z-axis after having been rotated away from the positive z-axis i.e. the return of the magnetic moment to the thermal equilibrium value $\bar{M}_0$, Figure 5a. T_2 relaxation can be represented by the loss of a net magnetisation in the x,y-plane, by random spreading (dephasing) of magnetic moments in this plane, Figure 5b.

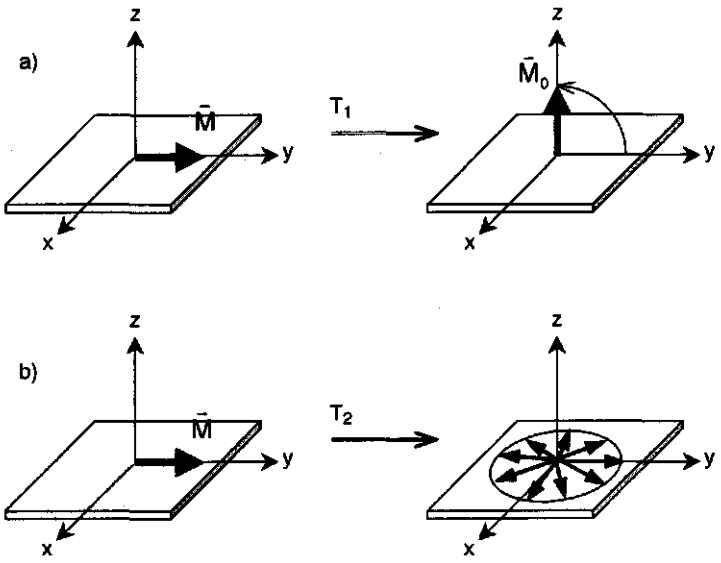

Figure 5, Simplified visualisation of a) T_1 and b) T_2 relaxation of a single spin ensemble in the rotating frame of reference.

Bloch (103,104) proposed a set of two differential equations as a phenomenological description of relaxation:

$$\frac{d\bar{M}_z}{dt} = \frac{\left(\bar{M}_z - \bar{M}_0\right)}{T_1} \qquad [6]$$

$$\frac{d\bar{M}_{x,y}}{dt} = \frac{\left(\bar{M}_{x,y}\right)}{T_2} \qquad [7]$$

As a result of T_1 relaxation the nuclear spins have a finite lifetime in a given spin state. Therefore, there is an inherent uncertainty in the resonance frequency, $\Delta\omega_0 \geq 1/T_1$, and therefore an inherent "lifetime" broadening, $\Delta\omega_0$, by this amount. Thus all processes that contribute to T_1 also affect T_2, and it turns out that T_2 cannot be longer than T_1 (103,104).

This inherent uncertainty in the resonance frequency is however not the linewidth which is eventually detected, $\Delta\omega = 1/T_{2,observed}$. Influences of the chemical environment of the observed nucleus,

$1/T_{2,internal}$, and inherent limitations of the detection of a signal, $1/T_{2,external}$, influence T_2 and thus add to the overall line width according to:

$$\frac{1}{T_{observed}} = \frac{1}{T_{nucleus}} + \frac{1}{T_{internal}} + \frac{1}{T_{external}} \qquad [8]$$

assuming fast exchange and a homogeneous sample.

Since this equation is also valid for T_1, T's do not have an index indicating either T_1 or T_2.

The influences of the chemical environment will be discussed next. The experimental limitations of the detection of a signal are adequately described elsewhere (103,104,108). In practice, each spin ensemble has its own T_1 and T_2. One and the same sample can therefore have various values of T_1 and T_2, corresponding to the spin ensembles it contains.

Relaxation is only caused by magnetic interactions of individual nuclear spins and is therefore in essence a process at the molecular level. The most important interactions causing T_1 and T_2 relaxation are

- dipole-dipole interactions,
- shielding anisotropy,
- spin-rotation interactions,
- scalar interactions,
- interactions with unpaired electrons.

Dipole-dipole interactions are of the same type as those observed macroscopically between two bar magnets. The interactions are modulated by a) molecular tumbling and/or b) translational diffusion.

a) Shielding of a nucleus by the surrounding electron configuration varies with the molecular orientation in the $\vec{B}_0$ field, except for sites of very high symmetry. Molecular tumbling therefore modulates the local magnetic field and thus causes relaxation. Coherent molecular rotation represents an angular momentum and generates a magnetic field, which can couple with nuclear spins (spin-rotation coupling), inducing a magnetic field at the nucleus. Scalar inter-molecular spin-spin interactions result from indirect coupling of two spins in one and the same molecule through the electronic spins of that molecule. This type of interactions usually affects T_2 more than T_1. Interactions with unpaired electrons are either dipolar or scalar and can originate from electron exchange or spin-lattice relaxation of the electronic spin itself. Because of the high magnetic moment of free electrons, interactions with unpaired electrons result in fast nuclear spin relaxation.

The intra-molecular nuclear-spin dipole-dipole-, intra-molecular shielding anisotropy- and the intra-molecular unpaired-electron interactions depend on the molecular tumbling rate, characterised by the rotational correlation time, τ_c, and are therefore strongly influenced by the molecular dynamics of the investigated system.

b) The inter-molecular dipole-dipole interactions are characterised by the translational self-diffusion coefficient of the molecule D.

Considering the above mentioned interactions, it can be understood that each spin ensemble has its own characteristic T_1 and T_2, determined by the molecular translational and rotational motion, the molecular structure and the electronic distribution around the observed nucleus. Even for one of the simpler spin systems, the protons in a water molecule, variation in macroscopic factors in a biological sample may induce single spin ensembles to be split up in many different ones, resulting in multi-exponential relaxation. Typical macroscopic effects, causing multi-exponential relaxation, are:

- sub-cellular compartmentation,
- cellular heterogeneity,
- relaxation-sinks at boundaries of homogeneous compartments,
- restricted self-diffusion of molecules in compartments with small dimensions,
- magnetic susceptibility differences between different regions in a sample.

The combined effects result in a mathematical description of relaxation by:

$$\vec{M}(t) = \sum_j \vec{M}_{t=0,j}\left(1 - \exp\left(-t/T_{1,j}\right)\right) \qquad [9]$$

$$\vec{M}(t) = \sum_j \vec{M}_{t=0,j} \exp\left(-t/T_{2,j}\right) \qquad [10]$$

where j denotes a particular spin ensemble in a sample.

Multi-exponential decay of magnetisation will be reduced to double or even single exponential decay if mixing of spin states occurs at a time scale shorter than the time-interval used to measure relaxation. Mixing can be caused by:

- exchange of nuclei of two or more ensembles over membranes,
- exchange between different compartments,
- chemical reactions,
- molecular (self)-diffusion.

Identification of individual exponentials from decay curves, according to equations 9 and 10, is often difficult, since it depends on the signal-to-noise ratio, the dwell-time and the number of data points in relation to the relaxation times to be separated and the interpretational model for a particular sample (123-126).

The main questions for each NMR experiment therefore are:

- What are the individual spin ensembles?
- What are their characteristic parameters?
- How can these parameters be identified?

Only after these questions have been answered, a meaningful interpretation of NMR data can be made.

1.3.2.4 NMR in compartmented plant tissue

Now the theoretical context of NMR/MRI studies has been set under the assumption of homogeneous samples, the influence of plant tissue on NMR/MRI signals requires a closer consideration before

typical studies can be addressed. At the same time, the information content of MRI techniques can be compared to the information content of microscopic techniques.

The various cellular compartments of a schematic plant-cell are presented in Figure 6.

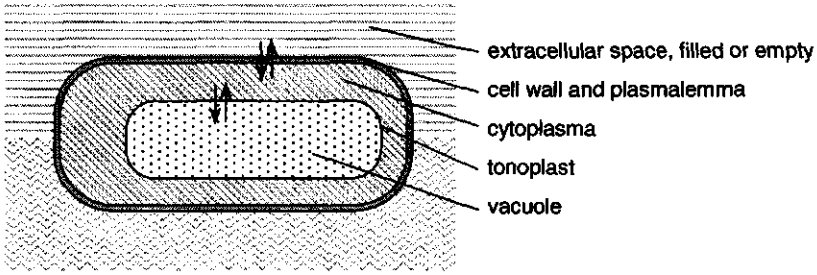

Figure 6, Schematic drawing of a plant cell, without i.e. chloroplasts (127).

In plant tissue at a cellular level three major compartments can be recognised:

- cytoplasma, filled with many sub-cellular compartments like the nucleus, ribosomes, endoplasmatic reticulum and sometimes chloroplasts or carbohydrate granules together with (paramagnetic) ions, polymeric sugars, proteins and water,
- vacuole, reservoir for sugar monomers and –polymers, (paramagnetic) ions and water,
- extracellular space, partially filled with water and plant nutrients or with air. Depending on the thickness and porosity of the cell wall, the cell wall can be considered as a separate compartment.

When plant tissue is placed in NMR/MRI equipment, magnetisation of all present spin ensembles is induced. The number of spin ensembles strongly depends on the (ultra)-structure of the sample and on the experimental set-up. Since the water proton is the most important nucleus studied in this Thesis, the influences of plant tissue structure on the NMR signal of the water proton will now be discussed.

Since the proton concentration is usually orders of magnitude higher than the concentration of other protons in plant tissue, almost all signal in the ^1H spectrum of plant tissue originates from the water proton. δ therefore does not offer an option to discriminate between spin ensembles. However, the relaxation behaviour of these water protons is heavily influenced by the (ultra)-structure of plant tissue. Here some of these influences are discussed.

In principle, all influences that are going to be discussed hold for both T_1 and T_2. However, since the timescale of T_2 processes is much shorter than for T_1 processes, T_2 decay in plant tissue can be multi-exponential (108). In this Thesis the Bloch equations (equation 9 and 10) are chosen as the fitting model for relaxation decay. It has however to be kept in mind that these equations are only a phenomenological descriptions of relaxation. Relaxation decay can also be non-exponential.

The number of spin ensembles present in a sample is hard to predict prior to the experiment. Because of the general constitution, geometry, size and fractional volume of plant cell compartments compared

to the resolution of the applied MRI imaging technique, observed NMR relaxation times are to varying extents influenced by:

- the applied magnetic field, $\vec{B}_0$ (128-138),
- the pixel resolution and the dimensions of the object under study (104,108,139,140),
- the state of water, being bound- or free water (104,136-138,141,142),
- the anisotropic rotational motion of water on hydrophilic macromolecules, (110,143)
- relaxation sinks near walls (the Brownstein and Tarr model (136,137)),
- the influence of solutes (118,144,145) and chemical exchange between water and chemically shifted solute protons (146),
- the presence of paramagnetic species (103),
- the sub-cellular compartmentation (127),
- the compartment size (147) and cellular compartmentation (114,127,148-150),
- the local field gradients (104) caused by magnetic susceptibility local inhomogeneities e.g. air spaces (150),
- the cellular heterogeneity (127) and the tissue ultrastructure (151),
- the membrane permeability (147,152,153).

T_1 (130-132) and T_2 (133-138) are influenced by the absolute value of $\vec{B}_0$. As a result of this dependence relaxation time values measured at different $\vec{B}_0$'s can not be compared one to one. On top of that, $\vec{B}_0$ inhomogeneities are the first to influence relaxation. Every $\vec{B}_0$ imperfection results in a broadening of the NMR signal. Some of these broadening effects can not be undone when their origin is laid in random motion of spins through these $\vec{B}_0$ imperfections. $\vec{B}_0$ inhomogeneities are therefore unwanted.

Diffusion of water protons over a distance Δr is unavoidable during data-acquisition resulting in a maximum spatial resolution. The optimum resolution is achieved when the hardware set-up is optimised for the T_2 values of the sample. Depending on the experimental set-up the resolution limiting factor can be either T_2, D or Δr, assuming a constant signal to noise ratio and no other hardware limitations (104,108).

The earliest explanations of multi-exponential relaxation used the concepts of bound- and free water. In this model two phases are distinguished: free water with a rotational correlation time $\tau_c = 10^{-12}$ s and water in close proximity with solid surfaces or macromolecules with $\tau_c = 10^{-8}$ s. Both phases have their characteristic relaxation times. There is however exchange of protons between the two phases, which can be slow or fast. In biological samples the transition between bound and free water is not sharp so that the two-phase description is often too simple (104).

In the limit of fast exchange, relaxation is mono-exponential and in the limit of slow exchange the result is multi-exponential relaxation. At intermediate exchange rates the simple model of mono- and multi-exponential decay breaks down, resulting in non-exponential decay. In general, T_1 of free water protons is sufficiently long compared to the fast exchange rates, therefore resulting in overall relaxation times according to equation 8. This leads to a proportionality between the bound water

fraction and the reciprocal T_1. For T_2 this proportionality does not apply since T_2 is faster compared to the exchange rates, entering the intermediate exchange rate region with non-exponential relaxation behaviour (141).
The model of free and bound water can be extended to three phases with a so-called structured water phase (110). However, the three-phase model also assumes fast exchange and therefore only holds for T_1.

Anisotropic water motion is responsible for the shortening of T_2 relative to T_1 caused by macromolecular structures in biological tissues (110). The selective influence of anisotropic motion on T_2 originates from an additional term in the expression for T_2 relaxation relative to T_1 relaxation. ((104), eq. 2.66 and 2.70). This term is averaged out by rapid isotropic molecular motion but contributes significantly to bound water moving anisotropically at macromolecular structures.
All these influences on relaxation time strongly depend on exchange between two phases in a sample. Brownstein and Tarr were among the first to present a model for the influence of geometry and self diffusion near walls on relaxation (136,137). Their model is based on T_1 for fast diffusive exchanging spins between two phases in a sample. They came up with an expression for T_1 for intact compartment boundaries. In general however, compartmental boundaries are not uniform in composition nor completely "reflective" (152,153) nor do they have a perfect spherical, cylindrical or planar shape. Most studies trying to apply the Brownstein and Tar model to plant tissue assume the plasmalemma and the cell wall to be the relaxation sink described in the model. However, plant cells are compartmented in more than one way. They have one or more vacuoles with a volume fraction depending on the developmental stage and carbohydrate granules that can fill a substantial part of a plant cell. In addition, these boundaries may exhibit selective exchange of water or can be absent for parts of the compartment.

For the last ten years the influence of sugar concentration on water proton relaxation in fruits is increasingly explored as a possible cause for changed water dynamics (118,144). The results of these studies imply however that relaxation parameters obtained from phantom studies do not directly relate to observed changes of relaxation parameters in intact fruits. The cell structure and magnetic field strength need to be taken into account for a proper interpretation of the observed relaxation processes.

Paramagnetic ions produce large fluctuating dipolar magnetic fields that accelerate nuclear relaxation (110). Therefore, T_2 can easily be reduced to non-observable values near paramagnetic species. When the paramagnetic ions are naturally present in the sample, they may need to be removed before detectable T_2 values can be obtained (>10 ms). However, when these ions are absent, the infiltration of a paramagnetic solution is a proven technique to suppress the signal from cellular compartments,

which are accessible to the infiltrate. Various compartments in apple tissue were distinguished by this method (127,128).

The extra cellular space can be filled either with an aqueous solution of plant nutrients or with air. When the extra cellular space is filled with air, large differences in diamagnetic susceptibility create local magnetic field gradients. When water protons diffuse through local gradients their resonance frequency randomly shifts, resulting in an additional decrease of T_2.

The last factor, which is important in this discussion, is the volume element size at which the relaxation mechanisms are studied in relation to the size of the plant cells. If the volume element size is reduced too much, the observed relaxation mechanisms do not originate from representative tissue samples. The results can easily be affected by the developmental stage of individual cells. Plant tissue is not necessarily uniform at the cellular level in all its developmental aspects of tissues which may appear macroscopically rather uniform. In special cases it is even possible to observe T_2 contrast in images of one and the same tissue type while no differences in light microscopy images are observed (117,143).

Taken these considerations together, it can be concluded that MRI has intrinsic limitations for the maximum spatial resolution, which can be achieved. There are however many different NMR/MRI methods to probe the compartmentation of heterogeneous systems. Some of these methods rely on the intrinsic properties of the system whereas others depend on the effects induced by external agents. A number of these methods are empirically based while others are dominated by an imposed theoretical model; but all these methods are likely to be affected to some extent by exchange processes. In comparison with the overwhelming structural detail in an electron micrograph, the NMR/MRI methods for compartmental analysis may at first sight appear rather primitive. However, the diversity of NMR methods and the fact that it is possible to probe solutes, solvent and surfaces non-invasively in appropriate cases, ensures that NMR/MRI can fulfil a successful complementary role in characterising the properties of compartments in plant tissue (116,148).

1.3.3 NMR/MRI in plant studies

1.3.3.1 NMR Spectroscopy in plant studies

First, the options to discriminate spin ensembles by their chemical shift δ will be discussed. This kind of NMR spectroscopy provides chemical shift information averaged over the complete sample.
Although NMR spectroscopy can be applied to a variety of nuclei (111-114,154-158), some nuclei are easier studied than other nuclei are. The parameters which, among others, make a particular nucleus more suitable for spectroscopy than an other nucleus are the resonance frequency range of the particular nucleus (chemical shift range), its natural abundance, sensitivity (the gyromagnetic ratio) and

relaxational behaviour. These parameters together determine whether a nucleus is suitable for a study to determine the desired information.

The ^{13}C nucleus offers a broad chemical shift range. The advantage of ^{13}C is the presence of this nucleus in many different metabolically interesting compounds. The natural abundance of the ^{13}C nucleus is however low (< 1%). This requires therefore a long data acquisition time and/or a high concentration of the observed nucleus.

^{13}C-NMR spectroscopy has been used in too many applications to review in this Introduction. One application, relevant for this Thesis, is the identification of metabolites in extracts of biological samples. Copious reviews have been published about ^{13}C-NMR spectroscopy, containing valuable information on chemical shifts and coupling constants. This information makes it possible to use ^{13}C spectroscopy for the quantification of metabolites in extracts (159-161). However, one of the major issues in extract studies is the quantitative relation between the integrated area under a particular resonance transition in a spectrum and the concentration of the related compound in the sample. This relation can be severely distorted by both the applied sample preparation technique (162) and the instrumentation parameters (159). Quantitative spectroscopic analysis of ^{13}C-NMR spectra is used in this Thesis to analyse metabolites in extracts of mushroom tissues.

Alternative nuclei can also be considered for spectroscopy or chemical shift selective imaging, including NMR spectroscopy of plants (111,114,128,148,156,163,164). Various methods have been described to assign MR resonances to cellular compartments, with or without the aid of shift reagents. Although the concentrations of the nuclei in spectroscopic studies can be substantially lower than the concentrations required for (spectroscopic) imaging, these studies indicate directions for future plant research using MRI.

1.3.3.2 Spectroscopic imaging

The combination of NMR spectroscopy and NMR imaging can be used to generate maps of chemical shift ranges. This kind of work is called chemical selective imaging or spectroscopic imaging.

Apart from water protons, samples contain non-water protons. Non-water protons can be used for imaging purposes whenever their signal can be distinguished from that of the water-protons. This can either be based on a sufficient chemical shift difference and/or a T_1 difference (104,106). In all cases, the concentration difference between both types of protons must be overcome. In plant tissue, the water-proton concentration is high (25 to 100 M or 22 to 90% water (m/m)), thereby making the differentiation difficult. In practice, differentiation can only successfully be applied to fruits, nuts and seeds. Macromolecular protons do not contribute to the NMR signal because their low molecular tumbling rate reduces T_2 to non-observable values. When the interest is focussed on a specific part of a sample, volume-selective spectroscopy can also be considered.

The main metabolic routes can be studied using ^{13}C imaging. In spite of the low natural abundance (± 1%), ^{13}C nuclei can be studied by applying quantum filtering techniques combined with isotopic labelling (165,166). These spectroscopic filtering techniques excite only protons directly bound to ^{13}C

nuclei, thereby suppressing the dominant water-proton signal (CYCLOCROP, (167)). The technique originates from NMR spectroscopy and since a vast variety of spectroscopic techniques exists, a whole new field of imaging techniques is still to be explored.

Some chemical shift selective (CHESS) imaging studies of plant tissue are known so far (106,166,168-174). These focus on water *vs.* oil and water *vs.* sugar distributions. Differences of 0.6 ppm in the proton spectrum between for instance water and unsaturated fattic-acids have been mapped at magnetic field strengths of 11.7 T (106).

1.3.3.3 Morphological imaging

Now the identification of spin ensembles by chemical shift differences is discussed, we will move to the identification of spin ensembles by relaxation time differences.

Following its introduction, MRI was primarily developed for medical application. However, the technique was also soon recognised as being able to contribute to the examination of the quality, histology, histochemistry and structural characteristics of pre- and post-harvest fruits and vegetables. Although the requirement for plants to grow under the natural influence of gravity and light are usually not met and spatial resolution is orders of magnitude less than with light microscopy, MRI has the advantage of being non-invasive and non-destructive. This makes MRI particularly suitable to follow a time sequence of events in an intact living system.

Studies performed with standard medical MRI protocols provide image contrast in a minimum acquisition time but without an easy analytical relation between the signal intensity and the fundamental NMR parameters ($\rho(^1H)$, T_1, T_2). It is interesting to see the huge variety of objects which have been studied this way. A few examples out of a total of at least 30 are: apple, avocados, banana and beans.

Investigated processes are: bruising, (de-)hydration, core breakdown, freezing, fungal infection, germination, growth dynamics, insect affection, pathogens distribution, phloem- and xylem flow, post-harvest treatment, riping, rotting, symbiosis between root nodules and bacteria, water content and water/oil distribution. Details are described elsewhere (104,106-108,115,116,175,179-183).

In the same way, MRI has been used in food research and production. These studies result in very diverse applications of MRI like peanut butter penetration in sandwiches and meat/fat ratio's in slaughter animals (175-177).

The application of MRI as a morphology imaging technique usually provides interesting information on sequential events but it does not reveal the relation between the observed contrast and the underlying biophysical processes like exchange, diffusion and compartmentation.

Signal intensity in these images is a function of a combination of various MRI parameters, among which T_1 (178), T_2 and the distribution of ρ are the most important (175,179-185). These images are therefore always called "parameter weighted" images. The applied imaging pulse sequence determines the weighting of the various parameters in the resulting image. Simple imaging pulse

sequences often allow the elimination of the influence of one parameter, but rarely give pure, single parameter, images (186). More elaborate sequences have therefore been developed. Together with suitable data analyses, they provide single-parameter MRI images, necessary for advanced "functional" imaging studies, e.g. to generate pure water distributions or pure T_2 images.

1.3.3.4 Relaxation imaging

Relaxation time weighted studies and quantitative relaxation time studies will be discussed next.

T_1 image contrast is traditionally acquired with saturation recovery or with inversion recovery techniques. These techniques have the disadvantage of long acquisition times, especially when T_1 maps are required. Since the time-scale of T_1 relaxation is usually long compared to chemical exchange, mixing or diffusional processes, multi- exponential decay is averaged out to mono-exponential decay. T_1 in plant tissue is approximately proportional to the water content. This relation is often explained in terms of the amount of bound and free water contributing to the observed MR signal (104,141,178,187). However, when alternative climatic conditions are applied to a sample, T_1 can be influenced for instance because of increased concentrations of soluble metabolites (145).

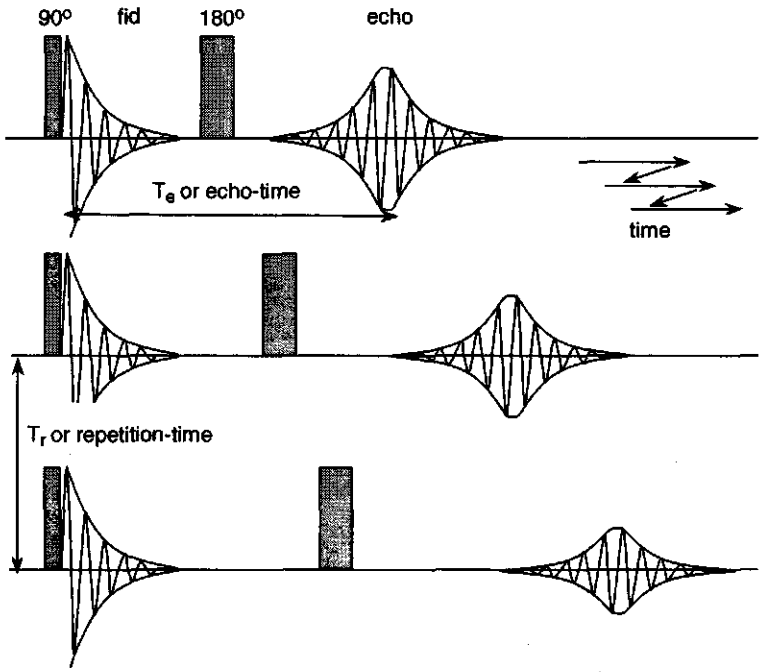

Figure 7, Hahn echo pulse sequence (188). One 180° pulse with different T_e's for each echo in the decaying signal is characteristic for this pulse sequence.

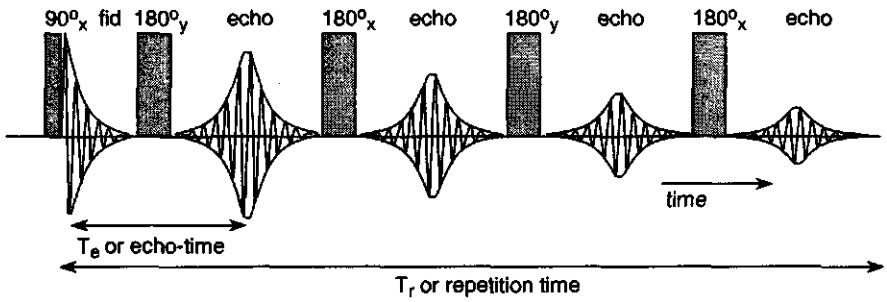

Figure 8, Carr-Purcel-Meiboom-Gill pulse sequence (CPMG sequence) (189,190). Multiple 180° pulses with constant T_e's between each echo characterise this pulse sequence.

There are two major methods for acquiring imaging data containing T_2 decay: the Hahn-echo (single spin-echo) technique with varying echo-times and a CPMG-like imaging technique with a constant echo-time and a varying number of echo's (cf. Fig. 7 and 8 respectively). The first technique has the disadvantage of introducing diffusion influences in the decay. The second technique refocuses these diffusion artefacts and, thereby, provides pure T_2 decay information (104).

The most suitable pulse sequence for determination of T_2 is the CPMG-sequence (187-191) (also denoted multiple spin-echo imaging) together with (multi-) exponential data analysis (125). Originally, this pulse sequence was not developed for imaging purposes, but spatially resolved, it is a powerful means to separate T_2 effects from the spin-density effects in an NMR image (139,192).

The optimum experimental conditions for quantitative T_2 imaging of plants are low magnetic field strength (< 2 T), a medium pixel resolution and a short T_e in a CPMG-like pulse sequence, provided T_r is sufficiently longer than T_1 (191-194).

When these conditions are met, T_2 decay is obtained. T_2 decay of water protons is strongly determined by the physiology of spin-ensemble(s) which is (are) being observed. Short T_2 values generally relate to bound water in the fast exchange limit. This can be water bound to macromolecules or (almost) freezing water. On the other hand, long T_2 values relate to free water. This can be a pool of bulk water or water in a vacuole.

More advanced techniques attempt to combine the measurement of the diffusion constant D with the elucidation of multi-exponential T_2 decay. The advance of these techniques is the extra dimension added to T_2 decay analysis. By separating fractions with different D-values, T_2 fractions can be separated, which otherwise could not be distinguished (149,195-197).

Various successful attempts have been made to assign multi-exponential T_2 decay to proton-pools in (homogeneous) plant samples. Since quantitative multi-exponential T_2 imaging is a relatively new technique, these examples are usually not spatially resolved.

Double exponential T_2 decay was in one case assigned to symplasmic and apoplasmic water in leafs of barley seedlings (187). In an other study short T_2 values (0.8 ms) were assigned to cell wall water;

medium T_2 values (40 ms) to late wood and long T_2 values (160 ms) to early wood of the red cedar (142,198). For apple parenchyma tissue, short T_2 values were assigned to cell wall water, medium T_2 values to cytoplasmatic water and long T_2 values to vacuolar water (127). Nevertheless, in again an other study, T_2 showed CPMG pulse spacing dependence for parenchyma tissue of courgettes, onion and apple (146). These studies discuss the traditional free- and bound-water approach for T_2 relaxation mechanisms. Multi-exponential T_2 decay was found to depend on fast chemical exchange of protons between water and hydroxylic protons, tonoplast and plasmalemma permeability and cell morphology.

In non-spatially resolved T_2 studies, diffusive attenuation due to imaging gradients does not occur. Short T_2 values are not further reduced and can therefore be distinguished from longer T_2 values. When however T_2 maps are required, diffusive attenuation is unavoidable. This was recognised by Edzes et al. who suggests T_2-maps of plant tissue to be acquired with medium pixel resolution and low magnetic field strengths (139). Diffusive attenuation is likely to be the reason why multi-exponential T_2 decay image analysis in plant-tissue is still in its infancy.

The identification of compartments in tissue depends strongly on the quality of the available data and the applied fitting algorithm (cf. chapter 1.3.2.3, (114,123,124,148)). Furthermore, compartments become hard to distinguish when the T_2 values are vary similar and/or when the amplitudes ratio becomes too large ($A_a > 4 * A_b$).

1.3.3.5 Functional Imaging

Functional plant imaging can be described as the imaging of spatially defined physiological processes in plants (115). The common characteristics of these studies are that they all focus on physiological changes of parts of plants using advanced imaging or data processing techniques. These techniques attempt to translate NMR parameters to physiological relevant plant parameters. The focus of these studies is the relation between NMR parameters and physiological parameters, which distinguish these studies from morphological imaging studies. Such a translation requires thorough understanding of the observed relaxation mechanism, an analytical relation between an NMR parameter and the physiological parameter of interest and total control over the relevant environmental conditions of the object under study. There are several excellent reviews (107-109,111,115).

Though mushrooms are no plants and the number of NMR/MRI studies on mushrooms is rather limited, the NMR/MRI results on the major anatomical features of plants will be discussed next. Two major differences between plant tissue and mushroom tissue are the higher degree of differentiation of plant cells and the loosely woven ultrastructure of hyphal threads in mushrooms. However the hyphal threads in mushrooms are also vacuolised and have a cell wall (cf. chapter 1.2).

Roots and nodules *in vivo* proved to be suitable for functional MRI studies. The main experimental difficulties are the presence of paramagnetic species and susceptibility inhomogeneities in the sample. When these difficulties can be overcome either by STRAFI-imaging (199) or by modifying or removing

the substrate, MRI offers good opportunities for studying the distribution and transport of water and perhaps carbohydrates in optically opaque root/soil systems (108).
Stems are well known for phloem and xylem studies. The cylindrical symmetry of the sample allows thicker slices for a better signal to noise ratio. The difficulty of these studies is always the positioning of the probe without damaging either roots or branches. If a stable experimental set-up can be realised, various kinds of physiological processes can be studied, i.e. the development of parenchymous and vascular tissue, bi-directional flow studies (115,117,200-202) and the influence of stress on the tissue properties. In one particular case, T_2 has been related to thermodynamic parameters (203,204). It is however arguable whether the claimed thermodynamical Gibbs energies can be obtained from T_2 values which only range from 10 to 30 ms and are likely to be caused by diffusion through the imaging gradients (139).

Leaves are interesting to study because these are the location of photosynthesis. However, their dimensions are generally difficult to fit in a MRI probe. Additionally, the MR-signal can be orientation dependent (205,206). This is an opportunity when properly understood but a nuisance at the assignment of spin ensembles to physiologically meaningful proton-pools. Because of the inhomogeneous structure of leaves, the MR-signal is likely to be affected by susceptibility differences.

Until now, very few MRI studies of flower development have appeared (108). These studies report single-exponential decay with T_2 between 8 and 15 ms. This T_2 range is rather small and requires considerable sample and imaging control. The results are likely to be easily affected by water state changes in the sample and susceptibility differences between the various tissue types in a flower, and therefore need careful interpretation.

Since fruits are important for human consumption, the number of studies is accordingly (108). These studies range from monitoring deterioration, fungal infection and bruising to the reconstruction of the vascular system. Especially those processes, which induce increasing amounts of extracellular water, are interesting because they result in increasing tissue T_2's by elimination of susceptibility inhomogeneities, due to disruption of cell structures. A good example is the difference between mealy apples and non-affected apples. When T_2 images of those apples are studied, the only significant difference appears to be the minimum T_2 value. However, the authors fail to conclude that the observed T_2 reduction in mealy apples is likely caused by increased susceptibility inhomogeneities (119).
Fruits, together with seeds ands nuts, contain large quantities of solutes. When the concentration of the solutes is sufficiently high, chemically selective imaging techniques become feasible, provided T_2's of the solutes are sufficiently long. These techniques open the field of monitoring fruit ripening in terms of changing metabolic activity (118,207). An other option is surface rendering techniques to reveal vasculature structures in fruits (208,209).

Seedlings allow an integral approach of the entire plant at resolutions, approaching cell dimensions. Especially the non-invasive monitoring of germination, differentiation and growth of seedlings is valuable in the field of plant crop development. Water relocations can be visualised in complete systems (115,117,200,208,209).

Summarizing these functional imaging studies, it is evident that plant MRI requires full understanding of the effects of the tissue ultrastructure on the observed MRI contrast. Since the ultrastructure of mushrooms can not be compared to the ultrastructure of plants described in the above-mentioned studies, a rigorous study to the origin of MRI contrast in mushrooms is an important aspect of this Thesis.

1.4 Thesis outline

In this Chapter, an introduction to the post-harvest physiology of the mushroom has been presented, resulting in the conclusion that the relation between the redistribution of water and the redistribution of metabolites, in the mushroom after harvest, needs further research. Furthermore, it is discussed that MRI contrast can not *a priori* be understood, especially because the ultrastructure of mushrooms differs significantly from that of most plants. The application of ^{13}C-NMR spectroscopy on extracts, ^{1}H-NMR imaging of intact mushrooms, and the interpretation of ^{1}H-NMR images of mushrooms are used to obtain information on the mushroom ultrastructure and the effects of storage on the metabolite contents.

Chapter 2 presents the results of a study on the redistribution of the most important metabolites in the mushroom. ^{13}C-NMR spectroscopy is applied to extracts of parts of the mushroom to elucidate storage dependent changes. Chapter 3 reports the results of an investigation of the optimum magnetic field for imaging of mushrooms. In this Chapter, the observed contrast in the NMR images is linked to the ultrastructure of the mushroom. This study is expanded in Chapter 4. Here the effects of the ultrastructure on proton relaxation times are quantified.

The results of the Chapters 3 and 4 find further application in Chapter 5, where the quantitative redistribution of water in the mushroom during storage is described and related to the metabolic changes reported in Chapter 2. In Chapter 6 the conclusions of the various Chapters are summarised and discussed in view of future research.

1.5 References

1) Flegg, P.B., Spencer, D.M. & Wood, D.A. (eds.); The biology and technology of the cultivated mushroom; John Wiley & Sons, Chichester (1985).

2) Van Roestel, A.J.J. & Adriaansen, R.A.J.; Mushroom Production and Consumption in the Netherlands 1985-1995. An Economic survey; De Champignoncultuur (1996); 40:5.

3) Kalberer, P.P.; Influence of the depth of the casing layer and the harvesting time on changes of the water content of the casing layer and the substrate caused by the first flush of mushrooms; Sci. Hort. (1983); 21: 9-18.

4) Kalberer, P.P.; Influence of the depth of the casing layer on the water extraction from casing soil and substrate by the sporophores, on the yield and on the dry matter content of fruit bodies of the first three flushes of the cultivated mushroom, *Agaricus bisporus* ; Sci. Hort. (1985); 27: 33-43.

5) Kalberer, P.P.; Water potentials of casing and substrate and osmotic potentials of fruit bodies of *Agaricus bisporus* ; Sci. Hort. (1987); 32: 175-182.

6) Kalberer, P.P.; Water relations of the Mushroom culture *Agaricus bisporus* study of a single break; Sci. Hort. (1990); 41: 277-283.

7) Flegg, P.B.; The water requirement of the mushroom crop; Sci. Hort. (1974); 2: 237-247.

8) Flegg, P.B.; The response of the mushroom crop to the pattern of watering; Sci. Hort. (1975); 3: 137-142.

9) Gibbons, W.R., Maher, A.A. & Todd, R.L.; Button mushroom production in synthetic compost derived from Agricultural wastes; Bioresource Techn. (1991); 38: 65-77.

10) Parrish, G.K., Beelman, R.B. & Kneebone, L.R.; Relationship between Yield and Mannitol content during the crop cycle of cultivated mushrooms; Hort. Sci. (1976); 11: 32-33.

11) Randle, P.; Mushroom yield response to the supplementation of synthetic compost at spawning; Sci. Hort. (1986); 29: 309-315.

12) Chang, S.T. & Hayes, W.A. (eds.); The Biology and Cultivation of Edible Mushrooms; Academic Press, New York (1978).

13) Griffin, D.H.; Fungal Physiology; John Wiley & Sons, New York (1981).

14) Rast, D. & Stauble, E.J.; Mode of action of isovaleric acid in stimulating the germination of *Agaricus bisporus* spores; New Phytol. (1970); 69: 557-566.

15) Straatsma, G., Gerrits, J.P.G., Gerrits, T.M., Op den Camp, H.J.M. & Van Griensven, L.J.L.D.; Growth Kinetics of *Agaricus bisporus* Mycelium on Solid Substrate (Mushroom Compost); J. Gen. Microbiol. (1991); 137: 1471-1477.

16) Rast, D., Greuter, B., Lendemann, J. & Zobrist, P.; The biochemistry of dormancy and germination of the Agaricus bisporus spore; Mushroom Sci. (1976); 9: 59-75.

17) Rast, D., Stäuble, E.J. & Zobrist, P.; The Krebs cycle and control of dormancy in Agaricus bisporus spore; New Phytol. (1976); 76:469-477.

18) Kalisz, H.M., Wood, D.A. & Moore, D.; Production, regulation and release of extracellular proteinase activity in basidiomycete fungi; Tr. Br. Mycol. Soc. (1987); 88: 221-227.

19) Claydon, N., Allan, M. & Wood, D.A.; Fruit body biomass regulated production of extracellular endocellulase during periodic fruiting by *Agaricus bisporus* ; Tr. Br. Mycol. Soc. (1988); 90: 85-90.

20) Durrant, A.J., Wood, D.A. & Cain, R.B.; Lignocellulose Biodegradation by *Agaricus bisporus* during solid substrate fermentation; J. Gen. Microbiol. (1991); 137: 751-755.

21) Matcham, S.E., Wood, D.A.; Purification of *Agaricus bisporus* Extracellular Laccase from Mushroom Compost; Biotech. Lett. (1992); 14: 297-300.

22) Wood, D.A., Claydon, N., Dudley, K.J., Stephens, S.K. & Allan, M.; Cellulase production in the life cycle of cultivated mushroom, *Agaricus bisporus* ; Aubert, J.P., Benguin, P. & Millet, J. (eds.); Biochem. Gen. Cellulose Degr. (1988); 53-70.

23) Baars, J.J.P., Op den Camp, H.J.M., van der Drift, C., Vogels, G.D. & Van Griensven, L.J.L.D.; the nitrogen metabolism of Agaricus bisporus; Mushroom science XIV, Proceedings of the 14th international congress on the science and cultivation of edible fungi, Oxford, (1995); 2: 811-818.

24) Kersten, M.A.S.H.; Baars, J.J.P., Op den Camp, H.J.M., Vogels, G.D., Van Griensven, L.J.L.D. & Elliott, T.J.; properties of the main nitrogen metabolising enzymes of Agaricus bisporus; Mushroom

science XIV, Proceedings of the 14th international congress on the science and cultivation of edible fungi, Oxford, (1995); 2: 803-810.

25) Straatsma, G.; Een belangrijke thermofiele schimmel in champignoncompost; De Champignoncultuur (1989); 33: 39-41.

26) Gerrits, J.P.G., Potyka, I. & Gams, W.; Mesofiele schimmels in champignon compost; De Champignoncultuur (1989); 33: 435-439.

27) Ross, R.C. & Harris, P.J.; The significance of thermophylic fungi in mushroom compost preparation; Sci. Hort. (1983); 20: 61-70.

28) Hammond, J.B.W. & Nichols, R.; Carbohydrate metabolism in *Agaricus bisporus* Changes in non-structural carbohydrates during periodic fruiting (flushing); New Phytol. (1979); 83: 723-730.

29) Hammond, J.B.W.; Variation in enzyme activity during periodic fruiting of *Agaricus bisporus* ; New Phytol. (1981); 89: 419-428.

30) Hammond, J.B.W. & Nichols, R.; Carbohydrate metabolism in *Agaricus bisporus* (Lange) Sing.: Changes in soluble carbohydrates during growth of mycelium and sporophore; J. Gen. Microbiol. (1976); 93: 309-320.

31) Kissmeyer-Nielsen, E., McClendon, J.H. & Woodmansee, C.W.; Changes in amino acids and urea in the cultivated mushroom, *Agaricus bisporus* , as influenced by nutrient supplementation of the compost during the growth cycle; J. Agric. Food Chem. (1966); 14: 633-636.

32) Umar, M.H. & Van Griensven, L.J.L.D.; Morphogenetic cell death in developing primordia of *Agaricus bisporus*; Mycologia (1997); 89: 274-277.

33) Umar, M.H. & Van Griensven, L.J.L.D.; Morphological studies on the life span, developmental stages, senescence and death of fruit bodies of *Agaricus bisporus*; Mycol. Res. (1997); 101: 1409-1422.

34) Umar, M.H. & Van Griensven, L.J.L.D.; Morphological research: developmental stages of *Agaricus bisporus*; De Champignoncultuur (1997); 41(3): 47-53.

35) Haddad, N.A. & Hayes, W.A.; Composition and food value of mushrooms; Hayes, W.A. & Atkins, F.C. (eds.); Quality in Mushrooms (1978); 18-29.

36) Beelman, R. B.; Variability in the composition and nutritional value of the cultivated mushroom *Agaricus bisporus* ; Mushroom News (1989); 37(7): 17-26.

37) van der Meer, M. A.; De samenstelling van geteelde champignon I; De Champignoncultuur (1987); 31: 331-347.

38) van der Meer, M. A.; De samenstelling van geteelde champignon II; De Champignoncultuur (1987); 31: 447-465.

39) Maga, J.M.; Mushroom Flavor; J. Agric. Food Chem. (1981); 29: 1-4.

40) Chen, C.C. & Wu, C.M.; Studies on the enzymic reduction of 1-octen-3one in mushroom (*Agaricus bisporus*); J. Agric. Food Chem. (1984); 32: 1342-1344.

41) Chen, C.C. & Wu, C.M.; Volatile components of mushroom (*Agaricus bisporus*); J. Food Sci. (1984); 49: 1208-1209.

42) Tsai, C.Y., Chen, C.C. & Wu, L.C.; Biochemical changes in *Agaricus bisporus* with age; Mushroom Sci. (1976); 1974: 9, Pt. 1, 357-370.

43) Minamide, T., Iwata, T. & Habu, T.; Studies on physiological, chemical properties and post-harvest keeping quality of mushrooms IX. Changes in soluble carbohydrates and keeping the freshness of mushrooms (*Agaricus bisporus* sing.) after harvest; Bull. Univ. Osaka Pref. Ser. B (1985); 37: 5-12.

44) Minamide, T. & Iwata, T.; Studies on physiological and chemical properties and postharvest keeping quality of mushrooms, XI Effect of storage temperature on the taste compounds, and protease and nucleic acid-degrading enzymes activities of mushrooms (*Agaricus bisporus*).; Bull. Univ. Osaka Pref. Ser. B. (1986); 38: 3-11.

45) Van Griensven, L.J.L.D.; Kwaliteit van champignons; De Champignoncultuur (1985); 29: 147-155.

46) Van Griensven, L.J.L.D.; Kwaliteit van champignons II; De Champignoncultuur (1985); 29: 263-275.

47) Andrawis, A. & Kahn, V.; Inactivation of mushroom tyrosinase by hydrogen peroxide; Phytochem. (1985); 24: 397-405.

48) Boyer, R.F., Mascotti, D.P. & Schori, B.E.; Ferroxidase activity of mushroom tyrosinase; Phytochem. (1986); 25: 1281-1283.

49) Burton, K.S.; Quality - investigations into mushroom browning; Mushroom J. (1985); 158: 68-70.

50) Burton, K.S.; The effects of pre- and post-harvest development on mushroom tyrosinase; J. Hortic. Sci. (1988); 63: 255-260.

51) Geels, F.P., Hesen, L.P.W., Rutjens, A.J. & Van Griensven, L.J.L.D.; Bruinverkleuring bij champignons; De Champignoncultuur (1992); 36: 343-349.

52) Ingebrigsten, J. & Flurkey, W.F.; Affinity and hydrophobic chromatography of mushroom tyrosinase; Phytochem. (1988); 27: 1593-1599.

53) Kahn, V.; Effect of proteins, protein hydrolyzates and amino acids on o-Dihydroxyphenolase activity of polyphenol oxidase of mushroom,avocado, and banana; J. Food Sci. (1985); 50: 111-115.

54) Kumar, M. & Flurkey, W.H.; Activity/Isoenzymes and Purity of Mushroom Tyrosinase in Commercial Preparations; Phytochem. (1991); 30: 3899-3902.

55) Moore, B.M., Kang, B. & Flurkey, W.H.; Histochemical and immunochemical localization of tyrosinase in whole tissue sections of mushrooms; Phytochem. (1988); 27: 3735-3737.

56) Schved, F. & Kahn, V.; Synergism exerted by 4-Methyl Catechol, Catechol, and their respective Quinones on the rate of DL-DOPA oxidation by mushroom tyrosinase; Pigm Cell Res. (1992); 5: 41-48.

57) Beelman, R.; Factors influencing post harvest quality and shelflife of fresh mushrooms; Mushroom J. (1988); 182: 455-463.

58) Czapski, J. & Bakowski, J.; Effect of storage conditions on the quality of cultivated mushrooms (*Agaricus bisporus* (Lange)Sing.); Acta Agrobot. (1986); 39: 221-234.

59) Frost, C.E., Burton, K.S. & Atkey, P.T.; A fresh look at cooling mushrooms; Mushroom J. (1989); 193: 23-29.

60) Murr, D.P. & Morris, L.L.; Effect of storage temperature on post-harvest changes in mushrooms; J. Amer. Soc. Hort. Sci. (1975); 100: 16-19.

61) Murr, D.P. & Morris, L.L.; Effect of storage atmosphere on post-harvest growth of mushrooms; J. Amer. Soc. Hort. Sci. (1975); 100: 298-301.

62) Dua, L.S. & Jandaik, C.L.; Cytokinins in two cultivated edible mushrooms; Sci. Hort. (1979); 10: 301-304.

63) Fermor, T.R., Henry, M.B., Fenlon, J.S., Glenister, M.J., Lincoln, S.P. & Lynch, J.M.; Development and Application of a Biocontrol System for Bacterial Blotch of the Cultivated Mushroom; Crop Protection (1991); 10: 271-278.

64) Gandy, D.G.; "Watery stipe" - a preliminary investigation; Mushroom Sci. (1959); IV: 411-415.

65) Harmsen, M.C., Tolner, B., Kram, A., Go, S.J., Dehaan, A. & Wessels, J.G.H.; Sequences of Three dsRNAs Associated with La France Disease of the Cultivated Mushroom (*Agaricus bisporus*); Current Gen. (1991); 20: 137-144.

66) Rainey, P.B.; Effect of *Pseudomonas putida* on Hyphal Growth of *Agaricus bisporus* ; Mycol. Res. (1991); 95: 699-704.

67) Rainey, P.B.; Phenotypic Variation of *Pseudomonas putida* and *Pseudomonas Tolaasii* Affects Attachment to *Agaricus bisporus* Mycelium; J. Gen. Microbiol. (1991); 137: 2769-2779.

68) Garcia Mendoza, C., Avellan, M.A., Sanchez, E. & Novaes-Ledieu, M.; Differentiation and wall chemistry of *Agaricus bisporus* vegetative and aggregated micelia; Arch. Microbiol. (1987); 148: 68-71.

69) Mol, P.C., Vermeulen, C.A. & Wessels, J.G.H.; Diffuse extension of hyphae in stipes of *Agaricus bisporus* may be based on a unique wall structure; Mycol. Res. (1990); 94: 480-488.

70) Mol, P.C. & Wessels, J.G.H.; Difference in wall structure between substrate hyphae and hyphae of fruit -body stipes in *Agaricus bisporus* ; Mycol. Res. (1990); 94: 472-479.

71) Braaksma, A., Schaap, D.J., Vrije, T. de, Jongen, W.M.F. & Woltering, E.J.; Ageing of the mushroom (*Agaricus bisporus*) under post-harvest conditions; Postharvest Biol. Techn. (1994); 4: 99-110.

72) Braaksma, A., Meer, P. van der & Schaap, D.J.; Polyphosphate accumulation in the senescing mushroom *Agaricus bisporus*; Postharvest Biol. Techn. (1996); 8: 121-127.

73) Hammond, J.B.W. & Nichols, R.; Changes in Respiration and Soluble Carbohydrates during the Post-Harvest Storage of Mushrooms (*Agaricus bisporus*); J. Sci. Food Agric. (1975); 26: 835-842.

74) Hammond, J.B.W.; Changes in composition of harvested mushrooms (*Agaricus bisporus*); Phytochem. (1979); 18: 415-18.

75) McArdle, F.J., Beelman, R.B. & Parrish, G.K.; Influence of post-harvest storage on the protein content of the cultivated mushroom, *Agaricus bisporus* ; Mushroom Sci. (1976); 1974: 9, Pt. 1, 341-346.

76) Oka, Y., Ogawa, T. & Sasaoka, K.; First evidence for the occurrence of N-acetyl-L-ornithine and quantification of the free amino acids in the cultivated mushroom, *Pleurotus ostreatus* ; J. Nutr. Sci. Vitaminol. (1984); 30: 27-35.

77) Burton, K.S., Partis, M.D., Wood, D.A. & Thurston, C.F.; Accumulation of serine proteinase in senescent sporophores of the cultivated mushroom *Agaricus bisporus*; Mycol. Res. (1997); 101: 146-152.

78) Ogawa, T., Oka, Y. & Sasaoka, K.; Amino acid profiles of common mushrooms including the identification of N-(N-γ-L-Glutamyl-3-Sulfo-L-Alanyl)Glycine in *Flammulina Velutipes* ; J. Food Sci. (1987); 52: 135-137.

79) Oka, Y., Tsuji, H., Ogawa, T. & Sasaoka, K.; Quantitative determination of the free amino acids and their derivatives in the common edible mushroom, *Agaricus bisporus* ; J. Nutr. Sci. Vitaminol. (1981); 27: 253-262.

80) Stijve, T. & Diserens, H.; Harnstoff in speisepilzen; Deutsche Lebensmittel-Rundschau (1988); 84: 248-252.

81) Berezenko, S. & Sturgeon, R.J.; The Enzymatic determination of D-mannitol with mannitol dehydrogenase from *Agaricus bisporus* ; Carbohydrate Res. (1991); 216: 505-509.

82) Duetsch, G.A. & Rast, D.; Biochemical relation between mannitol formation and the hexose monophosphate cycle in *Agaricus bisporus* ;. Phytochem. (1972); 11: 2677-2681.

83) Hammond, J.B.W. & Nichols, R.; Carbohydrate metabolism in *Agaricus bisporus* (Lange) Imbach.: metabolism of carbon-14-labeled sugars by sporophores and mycelium; New Phytol. (1977); 79: 315-325.

84) Hammond, J.B.W.; Carbohydrate metabolism in *Agaricus bisporus* : oxidative pathways in mycelium and sporophores; J. Gen. Microbiol. (1977); 102: 245-248.

85) Rast, D. & Bachofen, R.; Carboxylation reactions in *Agaricus bisporus* I. The endogenous carbon dioxide-acceptor; Arch. Mikrobiol. (1967); 57: 392-405.

86) Wehrli, M. & Rast, D.; Stoffwechsel von $^{14}CO_2$ in Plectenchymschnitten von *Agaricus bisporus*; Z. Pflantzenphysiol. (1967); 56: 325-339.

87) Atkey, P. T.; The scanning Electron Microscope in Mushroom Research; Mushroom J. (1983); 127: 241-243.

88) Atkey, P. T. & Nichols, R.; Surface structure of *Agaricus bisporus* by scanning electron microscopy; Mushroom J. (1983); 129: 334-335.

89) Hesen, L.P.W. & Van Griensven, L.J.L.D.; Verkleuring van champignons bezien met de electronen microscoop; De Champignoncultuur (1990); 34: 381-385.

90) Jasinski, E.M., Stemberger, B. & Kilara, A.; Ultrastructural studies of raw and processed tissue of the major cultivated mushroom, *Agaricus bisporus*.; Food Microstruc. (1984); 3: 191-196.

91) Wood, D.A., Craig, G.D., Atkey, P.T., Newsam, R.J. & Gull,K.; Ultrastructural studies on the cultivation process and growth and development of the cultivated mushroom *Agaricus bisporus* ; Food Microstruc. (1985); 4: 143-164.

92) Braaksma, A., Doorn, A.A. van, Kieft, H. & Aelst, A.C. van; Morphometric analysis of ageing mushrooms (*Agaricus bisporus*) during postharvest development; Postharvest Biol. Techn. (1998); 13: 71-79.

93) San Antonio, J.P. & Flegg, PB.; Transpiration from the sporophores of *Agaricus bisporus* 'white'; Amer. J. Bot. (1964); 51: 1129-1132.

94) Umar, M.H. & Van Griensven, L.J.L.D.; Hyphal regenaration and histogenesis in *Agaricus bisporus*; Mycol. Res. (1997); 101: 1025-1032.

95) Craig, G.D.; Morphogenesis in *Agaricus bisporus*; Thesis submitted to the University of Kent at Canterbury (1979).

96) Craig, G.D., Gull, K. & Wood, D.A.; Stipe Elongation in *Agaricus bisporus* ; J. Gen. Microbiol. (1977); 102: 337-347.

97) Laub, E. & Woller, R.; Über den Mannit- und Trehalosegehalt von Kulturchampignons (The Mannitol and Trehalose Content of Cultivated Champignons (Agaricus bisporus)); Mitt. Gebiete Lebensm. Hyg. (1984); 75: 110-116.

98) Hammond, J.B.W.; Sugar, sugar phosphate and NADP(H) levels in *Agaricus bisporus* fruit bodies; J. Gen. Microbiol. (1985); 131: 329-333.

99) Loescher, W. H., Tyson, R. H., Everard, J. D., Redgwell, R. J. & Bieleski, R. L.; Mannitol Synthesis in Higher Plants - Evidence for the Role and Characterization of a NADPH-Dependent Mannose 6-Phosphate Reductase; Plant Physiol. (1992); 98: 1396-1402.

100) Derikx, P.J.L., Op den Camp, H.J.M., Wagner, A.M., Straatsma, G., Van Griensven, L.J.L.D. & Vogels, G.D.; Respiratory pathways in *Agaricus bisporus* and *Scytalidium thermophilum* ; FEMS Microbiol. Lett. (1990); 66: 307-312.

101) Hammond, J.B.W.; Carbohydrate catabolism in harvested Mushrooms; Phytochem. (1978); 17: 1717-1719.

102) Morton, N., Dickerson, A.G. & Hammond, J.B.W.; Mannitol metabolism in *Agaricus bisporus* purification and properties of mannitol-dehydrogenase; J. Gen. Microbiol. (1985); 131: 2885-2890.

103) Gadian, D.G.; Nuclear magnetic resonance and its applications to living systems; Clarendon Press, Oxford, (1982).

104) Callaghan, P.T.; Principles of Nuclear Magnetic Resonance Microscopy; Clarendon Press, Oxford, (1991).

105) Lauterbur, P.C.; Image formation by induced local interactions: examples employing NMR; Nature (1973) 242: 190.

106) Pope, J.M.; Applications of chemical shift microscopy to non-invasive histochemistry of plant materials; In: Blümich B. & Kuhn, W. (eds.); Magnetic Resonance Microscopy methods and applications in materials science, agriculture and biomedicine; VCH Verlagsgesellschaft mbH, Weinheim (1992); 441-457.

107) Sarafis, V., Pope, J. & Sarig, Y.; Some aspects of NMR microscopy applications in plant science and agriculture; In: Blümich B. & Kuhn, W. (eds.); Magnetic Resonance Microscopy methods and applications in materials science, agriculture and biomedicine; VCH Verlagsgesellschaft mbH, Weinheim (1992); 459-476.

108) Chudek, J.A. & Hunter, G.; Magnetic resonance imaging of plants; Progress in Nuclear Magn. Reson. Spectroscopy (1997); 31: 43-62.

109) Clark, C.J., Hockings, P.D., Joyce, D.C. & Mazucco, R.A.; Applications of magnetic resonance imaging to pre- and post-harvest studies of fruits and vegetables; Postharvest Biol. Techn. (1997); 11: 1-21.

110) Wehrli, F.W., Shaw, D. & Kneeland, J.B. (eds.); Biomedical Magnetic Resonance Imaging. Principles, Methodology and Applications; VCH Verlagsgesellschaft mbH, Weinheim (1988).

111) Ratcliffe, R.G.; In vivo NMR studies of higher plants and algae; Adv. Bot. Res. (1994); 20: 44-123.

112) Martin, F.; Monitoring plant metabolism by ^{13}C, ^{15}N and ^{14}N nuclear magnetic resonance spectroscopy. A review of the applications to algea, fungi and higher plant; Physiol. Veg. (1985); 23: 463-490.

113) Morris, P.G.; Nuclear Magnetic Resonance Spectroscopy of Living Systems; Nucl. Magn. Reson. (1991); 20: 384-427.

114) Ratcliffe, R.G.; Application of Nuclear Magnetic Resonance methods to plant tissue; Meth. In Enzym. (1987); 148: 683-700.

115) MacFall, J.S. & Johnson, G.A.; The architecture of plant vasculature and transport as seen with magnetic resonance microscopy; Can. J. Bot. (1994); 72: 1561-1573.

116) MacFall, J.S. & Van As, H.; Nuclear Magnetic Resonance in Plant Biology; Current Topics in Plant Physiology; Volume 16; American Society of Plant Physiologists; Rockville, Maryland U.S.A. (1996); 33-76.

117) Kuchenbrod, E., Kahler, E., Thürmer, F., Deichmann, R., Zimmermann, U. & Haase, A.; Functional magnetic resonance imaging of intact plants-quantitative observation of flow in plant vessels; Magn. Reson. Imaging (1998); 16: 331-338.

118) Callaghan, P.T., Clark, C.J. & Forde, L.C.; Use of static and dynamic NMR microscopy to investigate the origins of contrast in images of biological tissues; Biophys. Chem. (1994); 50: 225-235.

119) Barreiro, P., Ruiz-Cabello, J., Fernandez-Valle, M.E., Ortiz, C. & Ruiz-Altisent, M.; Mealiness assessment in apples using MRI techniques; Magn. Reson. Imag. (1999); 17: 275-281.

120) Ratcliffe, R.G.; In vivo NMR spectroscopy: Biochemical and physiological applications to plants; Current Topics in Plant Physiology; Volume 16; American Society of Plant Physiologists; Rockville, Maryland U.S.A. (1996); 1-32.

121) Hinshaw, W.S., Bottomley, P.A. & Holland, G.N.; Radiographic thin-section image of the human wrist by nuclear magnetic resonance; Nature (1977); 270: 722-723.

122) Harris, R.K.; Nuclear Magnetic Resonance Spectroscopy, a physicochemical view; 5th edition, Longman Scientific & Technical, Harlow, (1991).

123) Whittall, K.P. & MacKay, A.L.; Quantitative Interpretation of NMR Relaxation Data; J. Magn. Reson. (1989); 84: 134-152.

124) Whittall, K.P.; Recovering Compartment Sizes from NMR Relaxation Data; J. Magn. Reson. (1991); 94: 486-492.

125) Brown, R.J.S.; Information Available and Unavailable from Multiexponential Relaxation Data; J. Magn. Reson. (1989); 82: 539-561.

126) Clayden, N.J. & Hesler, B.D.; Multiexponential Analysis of relaxation decays; J. Magn. Reson. (1992); 98: 271-282.

127) Snaar, J.E.M. & Van As, H.; Probing water compartments and membrane permeability in plant cells by ^{1}H-NMR relaxation measurements; Biophys. J. (1992); 63: 1654-1658.

128) Connelly, A., Lohman, J.A.B., Loughman, B.C., QuiQuampoix, H. & Ratcliffe, R.G.; High resolution imaging of plant tissues by NMR; J. Exp. Bot. (1987); 38: 1713-1723.

129) Lewa, C.J. & Lewa, M.; Temperature Dependence of 1H-NMR Relaxation Time, T_2, for Intact and Neoplastic Plant Tissues; J. Magn. Reson. (1990); 89: 219-226.

130) Hallenga, K. & Koenig, S.; Protein relaxation as studied by solvend ^{1}H and ^{2}H magnetic relaxation; Biochem. (1976); 15: 4255-4264.

131) Koenig, S.H. & Brown, R.D.; The importance of motion of water for magnetic resonance imaging; Invest. Radiol. (1985); 20: 297:305.

132) Diegel, J.G. & Pintar, M.M.; A possible improvement in the resolution of proton spin relaxation for the study of cancer at low frequency; J. Nat. Canc. Inst. (1975) 35: 725-726.

133) Bihan, D. Le, Turner, R. & MacFall, J.R.; Effect of intrafoxel incoherent motions (IVIM) insteady-state free precession (SSFP) imaging: application to molecular diffusion imaging; Magn. Reson. Med. (1989); 10: 324-337.

134) Meyer, R. A., & Brown, T.R.; Diffusion measurements by microscopic imaging; J. Magn. Reson. (1988); 76: 393-399.

135) Majumdar, S. & Gore, J.C.; Studies of diffusion in random fields produced by variations in susceptibility; J. Magn. Reson. (1988); 78:41-55.

136) Brownstein, K.R. & Tarr, C.E.; Spin-Lattice Relaxation in a system governed by diffusion; J. Magn. Reson. (1977); 26: 17-24.

137) Brownstein, K.R. & Tarr, C.E.; Importance of classical diffusion in NMR studies of water in biological cells; Phys. Rev. A. (1979); 19: 2446-2453.

138) Brownstein, K.R.; Diffusion as an Explanation of Observed NMR Behavior of water absorbed on wood; J. Magn. Reson. (1980); 40: 505-510.

139) Edzes, H.T., van Dusschoten, D. & Van As, H.; Quantitative T_2 imaging of plant tissues by means of multi-echo MRI microscopy; Magn. Reson. Imaging (1998); 16: 185-196.

140) von Kienlin, M. & Pohmann, R.; Spatially resolved spectroscopic imaging; in: Blümler, P., Blümich, B., Botto, R. & Fukushima, E. (eds.); Spatially Resolved Magnetic Resonance methods, Materials, Medicine, Biology, Rheology, Geology, Ecology, Hardware; Wiley-VCH, Weinheim (1998); 3-20.

141) Veres, J.S., Johnson, G.A. & Kramer, P.J.; In Vivo Magnetic Resonance Imaging of Blechnum Ferns: Changes in T_1 and N(H) during Dehydration and Rehydration; Amer. J. Bot. (1991); 78: 80-88.

142) Menon, R.S., Mackay, A.L., Flibotte, S. & Hailey, J.R.T.; Quantitative seperation of NMR images of water in wood on the basis of T_2; J. Magn. Reson. (1989); 82: 205-210.

143) Kuchenbrod, E., Haase, A., Benkert, R., Schneider, H. & Zimmermann, U.; Quantitative NMR microscopy on intact plants; Magn. Reson. Imag. (1995); 13: 447-455.

144) Clark, C.J., Lynley, N., Drummond, I.N. & MacFall, J.S.; Quantitative NMR imaging of kiwifruit (Actinidia deliciosa) during growth and ripening; J. Sci. Food Agric. (1998); 78: 349-358.

145) Clark, C.J. & MacFall, J.S.; Magnetic resonance imaging of persimmon fruit (*Diospyros kaki*) during storage at low temperature and under modified atmosphere; Postharvest Biol. Techn. (1997); 9: 97-108.

146) Hills, B.P. & Duce, S.L.; The influence of chemical and diffusive exchange on water proton transverse relaxation in plant tissues; Magn. Reson. Imag. (1990); 8: 321-331.

147) Ishida, N., Ogawa, H. & Kano, H.; Diffusion of cell-associated water in ripening barley seeds; Magn. Reson. Imag. (1995); 13: 745-751.

148) Belton, P.S. & Ratcliffe, R.G.; NMR and compartiment in biological tissues; Prog. NMR Spec. (1985); 17: 241-279.

149) Bihan, D. Le.; Molecular Diffusion Nuclear Magnetic Resonance Imaging; Magn. Reson. Quart. (1991); 7: 1-30.

150) Veres, J.S., Cofer, G.P. & Johnson, G.A.; Distinguishing Plant Tissues with Magnetic Resonance Microscopy; Amer. J. Bot. (1991); 78: 1704-1711.

151) Flibotte, S., Menon, R.S., MacKay, A.L. & Hailey, J.R.T.; Proton Magnetic Resonance of Western Red Cedar; Wood and Fiber Sci. (1990); 22: 362-376.

152) Snaar, J.E.M. & Van As, H.; NMR self-diffusion measurements in a bounded system with loss of magnitization at the walls; J. Magn. Reson. A (1993); 102: 318-326.

153) Hills, B. & Snaar, J.E.M.; Dynamic q-space microscopy of cellular tissue; Mol. Phys. (1992); 76: 979-994.

154) Rollins, A., Barber, J., Elliott, R. & Wood, B.; Xenobiotic monitoring in plants by ^{19}F and ^{1}H Nuclear magnetic resonance imaging and spectroscopy; Plant Physiol. (1989); 91: 1243-1246.

155) Schripsema, J. & Verpoorte, R.; Investigation of Extracts of Plant Cell Cultures by Proton Nuclear Magnetic Resonance Spectroscopy; Phytochem. Anal. (1991); 2: 155-162.

156) Ratcliffe, R.G.; NMR and the inorganic composition of plants; J. Inorg. Biochem. (1986); 28: 347-354.

157) Yazaki, Y., Asukawaga, N., Ishikawa, Y., Ohta, E. & Sakata, M.; Estimation of cytoplasmic free Mg^{2+} levels and phophorylation potentials in Mung Bean root tips by in vivo ^{31}P-NMR spectroscopy; Plant Cell Physiol. (1988); 29: 919-924.

158) Yazaki, Y., Maki, K., Sato, T., Ohta, E. & Sakata, M.; Application of ^{39}K-NMR spectroscopy to Potassium transport in Mung Bean root tips; Plant Cell Physiol. (1988); 29: 1417-1422.

159) Bock, K. & Pedersen, C.; Carbon-13 nuclear magnetic resonace spectroscopy of monosaccharides; Adv. in Carbohydrate Chem. and Biochem. (1983); 41: 27-65.

160) Kalinowski, H. O., Berger, S. & Braun, S.; Carbon-13 NMR spectroscopy; John Wiley & Sons, Chichester (1988).

161) Fan, T.W.M.; Recent advances in profiling plant metabolites by multi-nuclear & multi-dimensional NMR; Current Topics in Plant Physiology; Volume 16; American Society of Plant Physiologists; Rockville, Maryland U.S.A. (1996); 181-254.

162) Braaksma, A. & Schaap, D.J.; Protein analysis of the common mushroom *Agaricus bisporus*; Postharvest Biol. Techn. (1996); 7: 119-127.

163) Shachar-Hill, Y, Pfeffer, P.E. & Ratcliffe, R.G.; Measuring nitrate in plant cells by in vivo NMR using Gd^{3+} as a shift reagent; J. Magn. Reson B (1996); 111: 9-14.

164) Fox, G.G., McCallan, N.R. & R.G. Ratcliffe; Manipulating cytoplasmic pH under anoxia: a critical test of the pH switch from aerobic to anaerobic metabolism; Planta (1995); 195: 324-330.

165) Schneider, B.; In-vivo nuclear magnetic spectroscopy of low-molecular-weight compounds in plant cells; Planta (1997); 203: 1-8.

166) Tse, T.Y., Spanswick, R.M. & Jelinski, L.W.; Quantitative evaluation of NMR and MRI methods to measure sucrose concentrations in plants; Protoplasma (1996); 194: 54-62.

167) Heidenreich, M., Spyros, A., Köckenberger, W., Chandrakumar, N., Bowtell, R. & Kimmich, R.; CYCLOCROP Mapping of ^{13}C labelled compounds: Perspective in polymer science and plant physiology; in: Blümler, P., Blümich, B., Botto, R. & Fukushima, E. (eds.); Spatially Resolved Magnetic Resonance methods, Materials, Medicine, Biology, Rheology, Geology, Ecology, Hardware; Wiley-VCH, Weinheim (1998); 21-52.

168) Pope, J.M. & Walker, R.R.; Applications of NMR micro-imaging to the study of water, lipid and carbohydrate distribution in grape berries; Protoplasma (1997); 173: 177-186.

169) Goodman, B.A., Williamson, B. & Chudek, J.A.; Identification of the distribution of sugars in grapes using chemical shift selective NMR microscopy; Magn. Reson. Imag (1993); 11: 1039-1041.

170) Gussoni, M., Greco, F., Pegna, M., Bianchi, G. & Zetta, L.; Solid state and microscopy NMR study of the chemical constituentsof *Afzelia cuanzensis* seeds; Magn. Reson. Imag. (1994); 12: 477-486.

171) Metzler, A., Izquierdo, M., Ziegler, A., Köckenberger, W., Komor, E., von Kienlin, M., Haase, A. & Decorps, M.; Plant histochemistry by correlation peak imaging; Proc. Natl. Acad. Sci. USA (1995); 92: 11912-11915.

172) Meininger, M., Stowasser R., Jakob, P.M., Schneider, H., Koppler, D., Bringmann, G., Zimmermann, U. & Haase, A.; Nuclear magnetic resonance microscopy of Ancistrocladus heyneanus; Protoplasma. (1997); 198: 210-217.

173) Metzler, A., Köckenberger, W., von Kienlin, M., Komor, E. & Haase, A.; Quantitative measurement of sucrose distribution in ricinus communis seedlings by chemical-shift microscopy; J. Magn. Reson. B (1994); 105: 249-252.

174) Jagannathan, N.R., Govindaraju, V. & Raghunathan, P.; In vivo magnetic resonance study of the histochemistry of coconut (Cocos nucifera); Magn. Reson. Imag. (1995); 13: 885-892.

175) McCarthy, M.J. & Kauten, R.J.; Magnetic resonance imaging applications in food research; Tr. Food Sci. Techn. (1990); december: 134-139.

176) McCarthy, M.J. & McCarthy, K.L.; Applications of magnetic resonance imaging to food research; Magn. Reson. Imag. (1996); 14: 799-802.

177) Yan, Z.Y., McCarthy, M.J., Klemann, L., Otterburn, M.S. & Finley, J.; NMR applications in complex food systems; Magn. Reson. Imag. (1996); 14: 979-981.

178) Johnson, G.A., Brown, J. & Kramer, P.J.; Magnetic Resonance Microscopy of changes in water content in stems of transpiring plants; Proc. Natl. Acad. Sci. USA. (1987); 84: 2752-2755.

179) Chen, P., McCarthy, M.J. & Kauten, R.; NMR for Internal Quality Evaluation of Fruits and Vegetables; Amer. Soc. Agric. Eng. (1989); 32: 1747-1753.

180) Ishida, N., Kobayashi, T., Koizumi, M. & Kano, H.; ^{1}H-NMR imaging of tomato fruits; Agric. Biol. Chem. (1989); 53: 2363-2367.

181) Wang, P.C. & Chang, S.J.; Nuclear Magnetic Resonance Imaging of Wood; Wood and Fiber Sci. (1986); 18: 308-314.

182) Wang, C.Y. & Wang, P.C.; Nondestructive detection of core breakdown in "Bartlett" Pears with nuclear magnetic resonance imaging; Hort. Sci. (1989); 24: 106-109.

183) Wang, S.Y., Wang, P.C. & Faust, M.; Non-destructive detection of watercore in apple with nuclear magnetic resonace imaging; Sci. Hort. (1988); 35: 227-234.

184) Ahn, C.B. & Chu, W.C.; Optimal Imaging Strategied for Three-Dimensional Nuclear Resonance Microscopy; J. Magn. Reson. (1991); 94: 455-470.

185) Sezginer, A., Kleinberg, R.L., Fukuhara, M. & Latour, L.L.; Very rapid simultaneous measurement of nuclear magnetic resonance spin-lattice relaxation time and spin-spin relaxation time; J. Magn. Reson. (1991); 92: 504-527.

186) Gersonde, K., Tolxdorff, T. & Felsberg, L.; Identification and characterization of tissues by T_2-selective whole-body proton NMR imaging; Magn. Reson. Med. (1985); 2: 390-401.

187) Colire, C., Rumeur, E. Le, Gallier, J., Certaines, J. de & Larher, F.; An assessment of the proton nuclear magnetic resonance as an alternative method to describe water status of leaf tissues in wilted plants; Plant Physiol. Biochem. (1988); 26: 767-776.

188) Hahn, E. L.; Spin Echoes; Phys. Rev. (1950); 80: 580-594.

189) Carr, H.Y. & Purcell, E.M.; Effect of diffusion on free precession in Nuclear Magnetic Resonance Experiments; Phys. Rev. (1954); 94: 630-638.

190) Meiboom, S. & Gill, D.; Modified Spin-echo Method for Measuring Nuclear Relaxation Times; Rev Sc. Instr. (1958); 29: 688-691.

191) Duce, S.L., Carpenter, T.A., Hall, L.D. & Hills, B.P.; An investigation of the origins of contrast in NMR spin echo images of plant tissue; Magn. Reson. Imaging (1992); 10: 289-297.

192) Schneiders, N.J., Post, H., Brunner, P., Ford, J., Bryan, R.N. & Willcott, M.R.; Accurate T_2 NMR images.; Med. Phys. (1983); 10: 642-645.

193) Snaar, J.E.M. & Van As, H.; A Method for Simultaneous Measurement of NMR Spin-Lattice and Spin-Spin Relaxation times in Compartmentalised Systems; J. Magn. Reson. (1992); 90: 139-148.

194) Rofe, C.J., Van Noort, J., Back, P.J. & Callaghan, P.T.; NMR Microscopy using large, pulsed Magnetic-Field gradients; J. Magn. Reson. B (1995); 108: 125-136.

195) Van Dusschoten, D., Moonen, C.T.W., de Jager, P.A. & Van As, H.; Unraveling diffusion constants in biological tissue by combining Carr-Purcell-Meiboom-Gill Imaging and pulsed field gradient NMR; Magn. Reson. Med. (1996); 36: 907-913.

196) Van Dusschoten, D., de Jager, P.A. & Van As, H.; Extracting diffusion constants from echo-time-dependent PFG NMR data using relaxation time information; J. Magn. Reson. A (1995); 116: 22-28.

197) Van Dusschoten, D., de Jager, P.A. & Van As, H.; Flexible PFG NMR desensitized for susceptibility artifacts, using the PFG multiple-spin-echo sequence; J. Magn. Reson. A (1995); 112: 237-240.

198) Araujo, C.D., Mackay, A.L., Hailey, J.R.T., Whittall, K.P. & Le, H.; Proton Magnetic Resonance Techniques for Characterization of Water in Wood - Application to White Spruce.; Wood Sci. Techn. (1992); 26: 101-113.

199) Kinchesh, P., Randall, E.W. & Zick, K.; The elimination of susceptibility distortions in the imaging of liquids in solids: The stray field imaging technique; J. Magn. Reson. (1992); 100: 411-415.

200) Köckenberger, W., Pope, J.M., Jeffrey, K.R., Komor, E. & Callaghan, P.T.; A non-invasive measurement of phloem and xylem water flow in castor bean seedling by nuclear magnetic resonance microimaging; Planta (1997); 201: 53-63.

201) Schaafsma, T.J., Van As, H., Palstra, W.D., Snaar, J.E.M. & De Jager, P.A.; Quantitative measurements and imaging of transport processes in plants and porous media by 1H NMR; Magn. Reson. Imag. (1992); 10: 827-836.

202) Van As, H., Reinders, J.E.A., de Jager, P.A., van den Sanden, P.A.C.M. & Schaafsma, T.J.; In situ plant water balance studies using a portable NMR spectrometer; J. Exp. Bot. (1994); 45: 61-67.

203) Millard, M.M., Veisz, O.B., Krizek, D.T. & Line, M.; Magnetic resonance imaging (MRI) of water during cold acclimation and freezing in winter wheat; Plant Cell Environ. (1995); 18:535-544.

204) Millard, M.M., Veisz, O.B., Krizek, D.T. & Line, M.; Thermodynamic analysis of the physical state of water during freezing in plant tissue, based on the temperature dependence of proton spin-spin relaxation; Plant Cell Environ. (1996); 19: 33-42.

205) McCain, D.C., Marsh, K.B. & Peterson, L.A.; Water is allocated differently to chloroplasts in sun and shade leaves; Plant Physiol. (1988); 86: 16-18.

206) McCain, D.C. & Markley, J.L.; A theory and a model for interpreting the proton nuclear magnetic resonance spectra of water in plant leaves; Biophys. J. (1985); 48: 687-694.

207) Zion, B., Chen, P. & McCarthy, M.; Nondestructive quality evaluation of fresh prunes by NMR spectroscopy; J. Sci. Food Agric. (1995); 67: 423-429.

208) Glidewell, S.M., Williamson, B., Goodman, B.A., Chudek, J.A. & Hunter, G.; An NMR microscopic study of grape (Vitis vinifera L.); Protoplasma (1997); 198: 27-35.

209) Williamson, B., Goodman, B.A., Chudek, J.A., Hunter, G. & Lohman, J.A.B.; The vascular architecture of the fruit receptacle of red raspberry determined by 3D NMR microscopy and surface rendering techniques; New Phytol. (1994); 128: 39-44.

2

CHANGES IN METABOLITE CONCENTRATIONS DETECTED BY ^{13}C-NMR IN THE SENESCING MUSHROOM (*AGARICUS BISPORUS*)

published as:

Donker, H.C.W. & Braaksma, A.; Changes in metabolite concentrations detected by ^{13}C-NMR in the senescing mushroom (*Agaricus bisporus*); Postharvest Biol. Techn. (1997); 10: 127-134.

ELSEVIER

Postharvest Biology and Technology 10 (1997) 127–134

Postharvest Biology and Technology

Changes in metabolite concentrations detected by ^{13}C-NMR in the senescing mushroom (*Agaricus bisporus*)

H.C.W. Donker[a], A. Braaksma[b,*]

[a]*Department of Molecular Physics, Wageningen Agricultural University, Dreijenlaan 3, 6703 HA Wageningen, The Netherlands*
[b]*Agrotechnological Research Institute (ATO-DLO), P.O. Box 17, 6700 AA Wageningen, Netherlands*

Received 1 February 1996; accepted 21 August 1996

Abstract

Extracts of the cap, gill and stipe of the fruiting body of the mushroom (*Agaricus biporus*) were studied by ^{13}C-NMR spectroscopy. This technique enables changes in the main metabolite pools to be studied simultaneously as a function of storage time, temperature and postharvest development. An earlier reported reduction in dry weight of the stipe could be explained by a decrease in mannitol content. At 1°C storage temperature, no postharvest development occurred, yet mannitol content decreased. It is concluded that mannitol is probably used as a respiratory substrate in gill tissue. Proteolytic breakdown was apparent, even during storage at 1°C, but occurred preferentially in the stipe. The products are most probably used by the gill and to a lesser extent by the cap to maintain metabolic activity as demonstrated by urea-cycle activity. Changes in the content of four amino acid pools (glutamate, glutamine, alanine and aspartate) proved to be tissue-specific, as were changes in the content of mannitol, fumarate and malate. © 1997 Elsevier Science B.V.

Keywords: *Agaricus bisporus*; ^{13}C-NMR; Mushroom; Senescence

1. Introduction

The life-cycle of the sporophore of the mushroom *Agaricus bisporus* culminates with spore formation (Flegg, 1985). The life-cycle is not terminated by harvest, but continues and is morphologically indistinguishable from senescence of a fruiting body still in contact with its mycelium. When the mushroom fruiting body is not harvested, metabolic resource can be provided by the mycelium.

After harvest, the mushroom exhausts parts of the fruiting body in favour of gill development. Rearrangement of dry weight from stipe and cap towards gill tissue has been described by Braaksma et al. (1994). Hammond and Nichols (1975) showed that mannitol, generally regarded as an osmoticum, decreases in extracts of entire

* Corresponding author. Tel.: +31 317 475112; fax: +31 317 412268; e-mail: a.braaksma@ato.dlo.nl

mushrooms during postharvest development. The composition of harvested mushrooms with regard to free amino acids, is known to depend on compost composition, flush number (Crissan and Sands, 1978; Czapski and Bakowski, 1986), harvest time (Crissan and Sands, 1978; Burton, 1988) and strain (Weaver et al., 1977). Published reports mostly focus on changes in one specific compound during senescence. Often the reported analyses are performed on entire mushrooms, thus neglecting the specific function of the separate tissues. We therefore applied ^{13}C-NMR spectroscopy to monitor all main changes in metabolite concentrations simultaneously, in the separate tissues during senescence. We optimized a generally accepted extraction method, checked its reliability and assigned resonances of all metabolites which appear to change in separate, senescing, tissues. These results are compared with ^{13}C-NMR experiments in vivo on pieces of cap, stipe and gill-tissue of senescent mushrooms at comparable stages of development.

2. Materials and methods

Button mushrooms *Agaricus bisporus*, strain U1, were purchased from a local grower and transported to the laboratory within 1 h of harvest and stored at either high relative humidity (RH > 90%) under five different storage regimes or processed immediately. The five storage regimes were: 1°C, 3 days; 5°C, 3 days; 10°C, 3 days; 20°C, 3 days; 20°C, 6 days. Either immediately or after the storage period the mushrooms were separated into caps, stipes and gills and rapidly frozen in liquid nitrogen, to arrest enzymatic breakdown activated by cutting. The samples were stored at −25°C for a maximum of one week, until extraction.

2.1. Extraction procedures

The standard extraction method was based on a method previously described by Laub and Woller (1984). The frozen separated cap, stipe or gill-tissue of mushrooms was weighed and placed in a microwave oven (750 W), defrosted and boiled within 1 min. In this way, proteins were rapidly denatured. The boiled pieces of mushroom tissue were homogenized in a Waring blender. Sufficient boiling demineralized water was added to obtain a slurry. After centrifugation at 12 000 × *g* the supernatant was decanted and freeze-dried. A known amount of lyophilized powder (typically 0.3 g) was dissolved in 2 ml 0.25 M sodium phosphate and 0.25 M sodium acetate buffer, final pH 7.1, using acetate as internal reference, and inserted in a 10 mm outer diameter NMR sample tube.

Extracts were also made either by grinding a known amount of lyophilized tissue in demineralized water on ice, followed by centrifugation at 4°C and 12 000 × *g* for 10 min, or by grinding frozen mushroom tissue at 4°C in a 5-fold excess of 12% $HClO_4$. This extract was also centrifuged at 4°C and 12 000 × *g* for 10 min, and the supernatant neutralized with 2 M KOH.

The supernatants were freeze-dried and stored at −25°C until the NMR measurements were taken. For the NMR measurements, a known amount of lyophilized powder of the supernatants, typically 0.3 g, was dissolved in 2 ml 0.25 M sodium phosphate and 0.25 M sodium acetate, final pH 7.1, using acetate as internal reference.

2.2. In vivo mushroom samples

Mushrooms were stored for up to 6 days at 20°C, RH > 90%. At each day of the storage period a fruiting body was taken and separated into cap, gill and stipe. The excised separate parts of the mushroom were inserted in an NMR-tube together with an external reference capillary. Attention was paid to minimise wounding and mechanical disruption of the tissue.

2.3. ^{13}C-NMR spectroscopy

The ^{13}C-NMR spectra were recorded on a Bruker AMX 400 WB, operating at 100.6 MHz. Typical acquisition parameters were: sweep width 20 833 Hz, pulse duration 15 μs, data size 16 K complex data points, relaxation delay 2.5 s, number of scans 5000. Proton decoupling was achieved by a power gated GARP pulse sequence.

The FIDs were exponentially multiplied with a line broadening of 3 Hz, prior to zero filling and fast Fourier transformation. The ^{13}C-chemical shifts were measured relative to C_2-acetate at 23.95 ppm, assigned using published reference spectra (Usui et al., 1973; Rabenstein and Sayer, 1976; Wüthrich, 1976; Bock and Pedersen, 1983; Bock et al., 1984), and spiked with pure compounds when necessary.

One non-overlapping resonance of each compound of interest was chosen for quantification purposes. Integrals of these Lorentzian line shaped resonances were quantified by using calibration curves relative to the integral of the C_2-acetate signal. Calibration was applied to compensate for relaxation effects. The calibration curves were recorded in the concentration range around the expected concentration in the extracts with the same pH as the extracts. The correlation coefficient of the calibration curves was in all cases better than 0.99.

The complete experiment was repeated three times (e.g. on extracts from three different batches of harvested mushrooms) and the result averaged ($n = 3$). The results were expressed as mass percentages fresh weight by the use of the mass distribution. The results of the analyses were tested statistically by using the Student's t-test, at the 95% confidence level.

2.4. In vivo ^{13}C-NMR spectroscopy

The in vivo ^{13}C-NMR spectra of excized, intact pieces of tissues were recorded using an external reference, consisting of 0.5 ml 2 M sodium acetate in D_2O. The external reference, in a 5 mm NMR tube, was centred in the tissue sample, in the 10 mm NMR tube. The spectrometer was locked on the ^2H signal and shimmed to optimize the field. The acquisition parameters were similar to the parameters mentioned above, with the number of scans being 2500. The FID was exponentially multiplied with a line broadening of 20 Hz, prior to fast Fourier transformation. The spectra were referenced to 1.0 mmol C_2-acetate at 23.95 ppm. The $C_{1,6}$-mannitol signal at 64.0 ppm was used to quantify the in vivo spectra. An estimation for the amount of mannitol was made from the ratio between the integrated resonances at 23.95 of C_2-acetate and 64 ppm of $C_{1,6}$-mannitol. From this estimate the corresponding mass percentage fresh weight of mannitol was calculated.

3. Results

3.1. Spectral assignment

The standard extraction resulted in well-resolved spectra, comparable with the spectra obtained by either extraction of lyophilized mushroom tissue in water or extraction of frozen mushroom tissue in 12% $HClO_4$. ^{13}C-NMR spectra of extracts of lyophilized tissue in water showed better resolved trehalose resonances and some minor unknown resonances, probably originating from sugars or sugar-phosphates. A malate resonance was often not observed by this extraction method, as was the C_2-fumarate resonance in the spectra from the $HClO_4$ extracts.

Various spectra of extracts of comparable mushroom tissue, with respect to postharvest treatment, were compared. Those signals which changed in intensity, were identified. The identified compounds are summarized in Table 1, together with their ^{13}C-NMR assignments.

Most resonances were identified by their chemical shift values and the constant ratio of their intensities over various spectra. Additionally, resonances were assigned by spiking spectra with the compound involved. A large excess of mannitol is present in the mushroom (Morton et al., 1985; Braaksma, unpublished observations). The dominating resonances at 63.9, 70.1 and 71.7 ppm were therefore assigned to $C_{1,6}$, $C_{2,5}$ and $C_{3,4}$ of mannitol, respectively. The amino acids could be assigned according to Wüthrich (1976). The carbon atoms C_1–C_5 of glutamate and glutamine were assigned to the resonances at $\pm$175, 55.4, 27.6, 34.1, $\pm$181 and at $\pm$175, 54.9, 26.9, 31.6 and $\pm$178 ppm, respectively. The C_1 atoms of these amino acids could not be assigned unambiguously due to overlap with resonances of other carboxylic C_1 carbon atoms.

The C_3 of alanine was assigned to the unique signal at 16.9 ppm and the other two resonances

Table 1
Compounds identified in mushroom tissue with their assignments of the ^{13}C-NMR

Metabolite	^{13}C-NMR chemical shift δ, ppm relative to external TMS					
	C_1	C_2	C_3	C_4	C_5	C_6
Mannitol	63.9	71.7	70.1	70.1	71.7	63.9
Alanine	176.3	51.2	16.9			
Fumarate	±174	135.8	135.8	±174		
Glutamate	±175	55.4	27.6	34.1	±181	
Glutamine	±175	54.9	26.9	31.6	±178	
Malate	±181	43.1	70.9	±181		
Urea	163.2					
Aspartate	±175	52.8	37.2	±178		
Ornithine	175.1	55.1	28.1	23.5	39.6	
Trehalose	93.1	71.7	73.3	72.8	70.1	61.3
Acetate	±181	23.95				

Resonances which changed upon different postharvest treatments, e.g. storage at 1, 5, 10 and 20°C and RH > 90% for 3 days and storage at 20°C for 6 days.

were found at 176.3 ppm for C_1 and 51.2 ppm for C_2 of alanine.

The C_3 of aspartate was characterised by the resonance at 37.2 ppm; the resonances of the other carbon atoms were found at around 175 ppm for C_1 and 178 ppm for C_4, and at 52.8 ppm for C_2. The signal at 43.1 ppm was assigned to C_2 of malate, together with the signal at 70.9 ppm for C_3 and the signals around 181 ppm for C_1 and C_4.

The signal at 135.8 ppm was assigned to C_2 of fumarate after addition of some fumarate to the sample and re-recording of a spectrum. C_1 and C_4 of fumarate were found in the region of 174 ppm. After spiking with trehalose, the signals at 93.1, 73.3, 72.8 and 61.3 ppm were assigned to $C_{1,1'}$, $C_{3,3'}$, $C_{4,4'}$ and $C_{6,6'}$ of trehalose, respectively. Since trehalose is a rota-symmetric disaccharide, both monosaccharide units have identical ^{13}C-NMR resonance assignments. The signals of $C_{2,2'}$ and $C_{5,5'}$ could not be assigned due to overlap with the $C_{2,5}$ and $C_{3,4}$ signals of mannitol.

The signals at 23.5, 28.1 and 39.6 ppm could be assigned to the signals of C_4, C_3 and C_5 of ornithine, respectively, after assignment of all resonances of mannitol, glutamate, glutamine, alanine, aspartate, malate and fumarate and after spiking with ornithine. The C_1 and C_2 resonances of ornithine were found at 175.1 and 55.1 ppm, respectively. They both overlapped with other C_1- and C_2-resonances. The resonance at 163.2 ppm was assigned to the C_1 of urea because of its typical chemical shift value.

Only five major resonances could be observed in the *in vivo* spectra because of the much lower concentrations compared with the concentrated extracts and broad overlapping character of the resonances due to lack of homogeneity in the sample. The carboxylic C_1 atoms of various compounds gave rise to broad resonances around 175 ppm. No further details could be identified in this spectral region. Between 80 and 50 ppm, three broad resonances were observed. The resonance around 55 ppm was caused by C_2 atoms of amino acids. The two other resonances at 71 ppm and at 64 ppm were assigned to $C_{2,3,4,5}$ and $C_{1,6}$ of mannitol, respectively, because of the large excess of mannitol present in mushrooms. The same excess of mannitol was also observed in the spectra of extracts and is known from literature. The resonances around 30 ppm were too broad to assign. Acetate was used as internal reference; no evidence for the presence of acetate in mushrooms was found in extracts without acetate.

$C_{1,6}$-mannitol, C_4-glutamate, C_4-glutamine, C_3-alanine, C_3-aspartate, $C_{2,3}$-fumarate and C_2-malate could be identified in the ^{13}C-NMR spectra of the extracts unambiguously and quantified, using the reference signal of C_2-ac-

etate. Total mass percentages dry weight and the total mass percentages water soluble dry weight were determined. The mass percentages fresh weight of each compound for each part of the mushroom could be calculated and are presented in Figs. 1–4. Due to low signal to noise ratio and/or overlap, trehalose, ornithine and urea could not be quantified reliably.

The $C_{1,6}$-mannitol resonance in the in vivo spectra was quantified as described above. The results were comparable with the mannitol content as measured in extracts for cap and stipe tissue, but not for gill tissue. Probably due to excessive wounding and mechanical disruption of the gill tissue because of sample preparation and lack of tissue homogeneity in the NMR-sample tube, the in vivo measured contents of mannitol were roughly four times lower than those measured in extracts (results not shown).

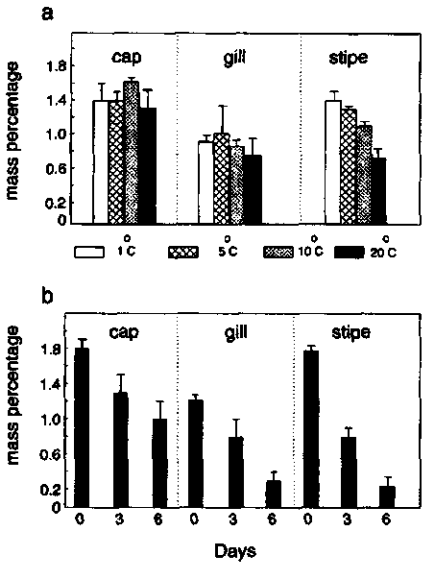

Fig. 1. Mass percentages of fresh weight of mannitol (a) as a function of the storage temperature during 3 days at high relative humidity (> 90%) and (b) as a function of the storage duration at 20°C and high relative humidity (> 90%). Day 0 is within 1 h of harvest. The values and their standard deviations are derived from three different batches of harvested mushrooms.

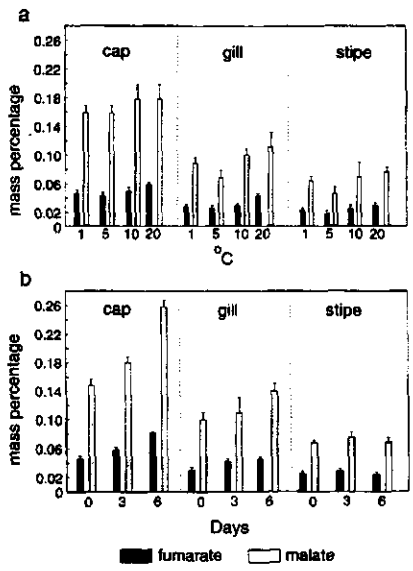

Fig. 2. Mass percentages of fresh weight of fumarate and malate (a) as a function of the storage temperature during 3 days at high relative humidity (> 90%) and (b) as a function of the storage duration at 20°C and high relative humidity (> 90%). Day 0 is within 1 h of harvest. The values and their standard deviations are derived from three different batches of harvested mushrooms.

4. Discussion

^{13}C-NMR spectra of different extracts from the same mushroom tissues proved to be completely comparable. This indicates that no artefacts are introduced by the extraction method. Those compounds which changed in content during postharvest development (e.g. opening of the cap, growth of gills and formation of spores) and which could be identified reliably, are listed in Table 1.

In all tissues there was a significant decrease in mannitol after harvest (Fig. 1(b), day 0), and also after 3 days at 1°C (Fig.1(a)), when there is no postharvest development (e.g. opening of the cap,

growth of gills and formation of spores). Since postharvest development was absent at 1°C, this suggests that mannitol is used as a respiratory substrate. In gill tissue, the mannitol content decreased only after 3 days at 20°C, when postharvest development was completed. In both the gill and cap tissue the mannitol content decreased further when the mushrooms were stored for 6 days at 20°C (Fig. 1(b)). Stipe tissue was the only tissue in which, at each applied storage condition, a significant decrease in mannitol content was found. The total decrease in mass percentage (at 20°C for 3 days) in stipe tissue equals the observed decrease in dry weight of the stipe as reported earlier (Braaksma et al., 1994). This could be interpreted as the loss in dry weight in the stipe during postharvest development (20°C storage) being mainly due to transport of mannitol (equivalents) from stipe to gill tissue. Since

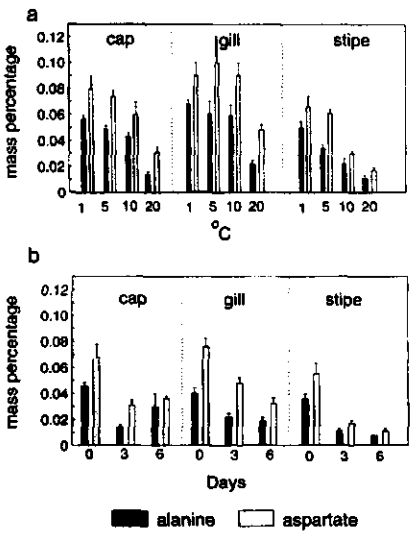

Fig. 3. Mass percentages of fresh weight of alanine and aspartate (a) as a function of the storage temperature during 3 days at high relative humidity (> 90%) and (b) as a function of the storage duration at 20°C and high relative humidity (> 90%). Day 0 is within 1 h of harvest. The values and their standard deviations are derived from three different batches of harvested mushrooms.

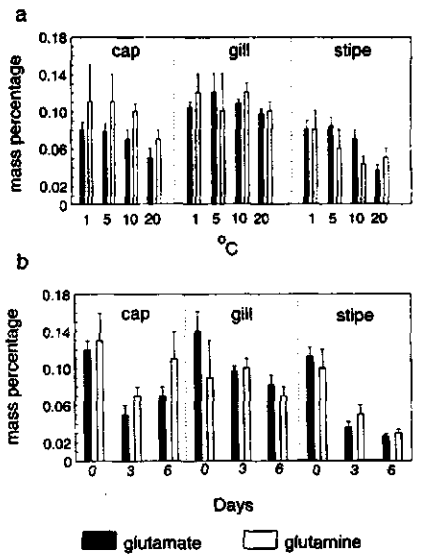

Fig. 4. Mass percentages of fresh weight of glutamine and glutamate (a) as a function of the storage temperature during 3 days at high relative humidity (> 90%) and (b) as a function of the storage duration at 20°C and high RH (> 90%). Day 0 is within 1 h of harvest. The values and their S.D. are derived from three different batches of harvested mushrooms.

about 70% of the respiratory capacity is located in gill tissue (Braaksma et al., 1996), mannitol is probably used as a respiratory substrate.

In all tissues the fumarate content was not significantly changed in storage at 1, 5 and 10°C, although the contents in the different tissues were not the same (Fig. 2(a)). In cap and gill tissue a small increase was found after 3 or 6 days of storage at 20°C (Fig. 2(b)). In stipe tissue the content of both malate and fumarate was constant during 3 days storage (Fig. 2(a)), but in the cap and gill tissue the malate content significantly increased when stored at 10°C during 3 days. After postharvest development was completed (20°C for 3 days) the increase continued up to 6 days (Fig. 2(b)). Going from 1 to 20°C, the respiration rate increased by a factor of 8 or more. In spite of the fact that the metabolic rates are quite different, the Krebs cycle is apparently able to

keep the malate content constant at a low level in tissue either stored at 1 or at 20°C. One striking feature is the fact that the content of malate in the cap tissue was two to three times higher than in the other tissues. Apparently the regulation of the balance of the Krebs cycle is different in this tissue.

Harvest (Fig. 3(b), day 0) induced a significant increase in aspartate and alanine in all tissues except for aspartate in the cap (Fig. 3(a)). Upon storage at 20°C for 3 days, the content of alanine and aspartate in all tissues decreased (Fig. 3(b)). This decrease continued in gill and stipe tissue when stored for up to 6 days (Fig. 3(b)). However, in the cap an increase was observed during this prolonged storage period. When stored at temperatures of 1, 5 and 10°C, the content of these two amino acids stayed constant in gill tissue and decreased in the other tissues.

Under different storage temperatures, the changes in content of glutamate and glutamine were about the same as observed for alanine and aspartate. In contrast with alanine and aspartate, harvest induced a decrease in content in all tissues.

Proline and lysine were expected to be present in the extracts (Oka et al., 1981) but could not be identified by our method. A resonance of C_5-proline was expected around 46.8 ppm and a resonance of C_4-lysine was expected around 22 ppm. Neither resonances were observed in all three extraction methods. We conclude that either these compounds are not present in concentrations high enough to be detected in the extracts by the described method or that they are absent due to different growing circumstances or differences between cultivars.

Since the mushroom is deprived of metabolic resources after harvest, proteolysis is initiated (Murr and Morris, 1975a,b; Hammond, 1979; Burton, 1988) to complete its postharvest development. Proteolysis is explained as an adaptation of the mushroom to the starving conditions brought about by harvesting (Murr and Morris, 1975a,b). The data, here presented, show that a change in content of four amino acid pools after harvest (glutamate, glutamine, aspartate and alanine) is tissue-specific. Since proteolytic activity is present, these amino acids should be supplied in excess to the free amino acid pool and a rise in concentrations was expected. However, apparently these free amino acids are processed rapidly in various metabolic pathways. Evidence for the breakdown of amino acids is the presence of an active urea-cycle, illustrated by the fact that rising amounts of urea were found in all tissues. Though the amount of urea could not be quantitated reliably, the increase during postharvest development was clear (results not shown). This is in accordance with the findings of Braaksma and Schaap (1996) also on the U1 cultivar. Indications for the reported presence of ornithine (Oka et al., 1981) were mainly found in the gill tissue. The applied method provides synchronized information about changing contents of metabolites in the different tissues of the senescing mushroom under postharvest conditions. Further investigations should be directed to measuring the fluxes of these compounds in order to complete the picture of carbon metabolism in senescing mushrooms.

Acknowledgements

The author H. Donker thanks the State Institute for Quality Control of Agricultural Products (RIKILT-DLO), for the financial support of his work. Also the financial support for A. Braaksma by the CNC, the Dutch Mushroom Growers Association, is highly appreciated. The authors thank D.J. Schaap of the Agro Technological Research Institute (ATO-DLO) for his assistance with the practical work.

References

Bock, K., Pedersen, C. and Pedersen, H., 1984. Carbon-13 nuclear magnetic resonance data for oligosaccharides. Adv. Carbohydr. Chem. Biochem., 42: 193–225.

Bock, K. and Pedersen, C., 1983. Carbon-13 nuclear magnetic resonace spectroscopy of monosaccharides. Adv. Carbohydr. Chem. Biochem., 41: 27–65.

Braaksma, A. and Schaap, D.J., 1996. Protein analysis of the common mushroom *Agaricus bisporus*. Postharvest Biol. Technol., 7: 119–127.

Braaksma, A., Schaap, D.J., Vrije, T., de Jongen, W.M.F. and Woltering, E.J., 1994. Ageing of the mushroom (*Agaricus bisporus*) under post-harvest conditions. Postharvest Biol. Technol., 4: 99–110.

Braaksma, A., van der Meer, P. and Schaap, D.J., 1996. Polyphosphate accumulation in the senescing mushroom *Agaricus bisporus*. Postharvest Biol. Technol., 8: 121–127.

Burton, K.S., 1988. The effects of pre- and post-harvest development on mushroom tyrosinase. J. Hortic. Sci., 63: 255–260.

Crissan, E.V. and Sands, A., 1978. Nutritional value. In: The Biology and Cultivation of Edible Mushrooms, Chang, S.T. and Hayes, W.A. (Eds). Academic Press, New York, pp. 137–167.

Czapski, J. and Bakowski, J., 1986. Effect of storage conditions on the quality of cultivated mushrooms (*Agaricus bisporus* (Lange) Sing.). Acta Agrobot., 39: 221–234.

Flegg, P.B., 1985. In: The Biology and Technology of the Cultivated Mushroom, Flegg, P.B., Spencer, D.M. and Wood D.A. (Eds). Wiley, Chichester, pp. 203–204.

Hammond, J.B.W., 1979. Changes in composition of harvested mushrooms (*Agaricus bisporus*). Phytochemistry, 18: 415–418.

Hammond, J.B.W. and Nichols, R., 1975. Changes in respiration and soluble carbohydrates during the post-harvest storage of mushrooms (*Agaricus bisporus*). J. Sci. Food Agric., 26: 835–842.

Laub, E. and Woller, R., 1984. Über den Mannit- und Trehalosegehalt von Kulturchampignons (the mannitol and trehalose content of cultivated champignons (*Agaricus bisporus*)). Mitt. Gebiete Lebensm. Hyg., 75: 110–116.

Morton, N, Dickerson, A.G. and Hammond, J.B.W., 1985. Mannitol metabolism in *Agaricus bisporus*: purification and properties of mannitol dehydrogenase. J. Gen. Microbiol., 131: 2885–2890.

Murr, D.P. and Morris, L.L., 1975a. Effect of storage temperature on post-harvest changes in mushrooms. J. Am. Soc. Hort. Sci., 100: 16–19.

Murr, D.P. and Morris, L.L., 1975b. Effect of storage atmosphere on post-harvest growth of mushrooms. J. Am. Soc. Hort. Sci., 100: 298–301.

Oka, Y., Tsuji, H., Ogawa, T. and Sasaoka, K., 1981. Quantitative determination of the free amino acids and their derivatives in the common edible mushroom, *Agaricus bisporus*. J. Nutr. Sci. Vitaminol., 27: 253–262.

Rabenstein, D.L. and Sayer, T.L., 1976. Carbon-13 chemical shift parameters for amines, carboxylic acids, and amino acids. J. Magn. Resn., 24: 27–39.

Usui, T., Yamaoka, N., Matsuda, K., Tuzimura, K., Sugiyama, H. and Seto, S., 1973. ^{13}C nuclear magnetic resonance spectra of glucobioses, glucotrioses and glucans. J. Chem. Soc.-I. Perkin, 20: 2425–2432.

Weaver, J.C., Kroger, M. and Kneebone, L.R., 1977. Comparative protein studies (Kjeldahl, dye binding, amino acid analysis) of nine strains of *Agaricus bisporus* (Lange) Imbach mushrooms. J. Food Sci., 42: 364–366.

Wüthrich, K., 1976. NMR in Biological Research: Peptides and Proteins. North-Holland, Amsterdam.

3

NMR IMAGING OF WHITE BUTTON MUSHROOM (*AGARICUS BISPORUS*) AT VARIOUS MAGNETIC FIELDS

published as:

Donker, H.C.W., Van As, H., Edzes, H.T. & Jans, A.W.H.; NMR Imaging of white button mushroom (*Agaricus bisporus*) at various magnetic fields; Magn. Reson. Imag. (1996); 14: 1205-1215.

ELSEVIER

Magnetic Resonance Imaging, Vol. 14, No. 10, pp. 1205–1215, 1996

● *Original Contribution*

NMR IMAGING OF WHITE BUTTON MUSHROOM (*AGARICUS BISPORIS*) AT VARIOUS MAGNETIC FIELDS

H.C.W. DONKER, H. VAN AS, H.T. EDZES AND A.W.H. JANS

Department of Molecular Physics, Agricultural University, 6703 HA Wageningen, The Netherlands

Nuclear magnetic resonance (NMR) and magnetic resonance imaging (MRI) have been applied to visualize physiological phenomena in plants and agricultural crops. Imaging sequences that result in contrast of a combination of parameters (e.g., proton density, T_1, T_2, T_2^*) cannot be used for a correct and unique interpretation of the results. In this study multiecho imaging together with monoexponential T_2 decay fitting was applied to determine reliable proton density and T_2 distributions over a mushroom. This was done at three magnetic field strengths (9.4, 4.7, and 0.47 T) because susceptibility inhomogeneities were suspected to influence the T_2 relaxation times negatively, and because the influences of susceptibility inhomogeneities increase with a rise in magnetic field strength. Electron microscopy was used to understand the different T_2's for the various tissue types in mushrooms. Large influences of the tissue ultrastructure on the observed T_2 relaxation times were found and explained. Based on the results, it is concluded that imaging mushrooms at low fields (around or below 0.47 T) and short echo times has strong advantages over its high-field counterpart, especially with respect to quantitative imaging of the water balance of mushrooms. These conclusions indicate general validity whenever NMR imaging contrast is influenced by susceptibility inhomogeneities.

Keywords: **Mushrooms; *Agaricus bisporus*; Field strength; Multiecho imaging; Image contrast; Plant tissue; Quantitative imaging**

INTRODUCTION

The white button mushroom (*Agaricus bisporus*) is an important crop in The Netherlands, with an estimated turnover volume of about $180 million annually (1988). It is, however, prone to fast senescence and therefore easily loses its economic value.

Mushrooms contain over 90% of water by weight[1] and have a spongy structure with large extracellular spaces.[2–6] These spaces can be filled with either air or water. The density of the mushroom is about 0.6 g/ml, but this density varies with the amount of extracellular water and the ultrastructure of the mushroom.[1] The tissue density may be as high as 0.9 g/ml in the gill or as low as 0.3 g/ml in the core of the stipe. Mushroom growers can influence the amount of extracellular water by watering their crop the day before harvest, although this extracellular water reduces the quality of the mushroom.

Nuclear magnetic resonance (NMR) imaging is attractive to study the relation between water distribution and the postharvest physiological changes in mushrooms, because this technique gives access to the noninvasive determination of the water distribution in an object. NMR imaging of plant material has already been applied successfully to ripening of tomatoes,[7] core detection of pears and apples,[8–11] stems of transpiring plants,[12] Blechnum ferns,[13] wood and roots of Douglas fir seedlings,[14] and a number of food products.[15] In these studies qualitative information on the internal structure of the objects under study has been obtained, since image contrast in these studies originates from the combined effects of the spin–spin relaxation (T_2), spin-lattice relaxation (T_1), spin density and the applied magnetic field strength (B_0). The selection of a particular type of image contrast depends on the question about the tissue structure and properties to be addressed.

H.C.W. Donker, H. Van As, and H.T. Edzes were deeply saddened by the death of A.W.H. Jans on December 12, 1994.

RECEIVED October 24, 1995; ACCEPTED April 24, 1996.

Address correspondence to H. Van As, Department of Molecular Physics, Agricultural University, Dreijenlaan 3, 6703 HA Wageningen, The Netherlands.

To relate NMR images to water balances and distributions quantitatively, however, theoretical knowledge of contrast in NMR images is required to separate individual NMR parameters and translate them to the physiology of the investigated object.[15-22,47,48] Several attempts to understand NMR contrast have already been made in, for instance, cactus with deuterium, NMR[23] squash with T_1 weighting,[24] courgette with T_2 weighting,[25] and wood[26-28] and plants[47] with quantitative T_2 and spin density imaging.

Usually the effects of B_0 and susceptibility inhomogeneity on the NMR images are not taken into consideration,[25,47] but because of the spongy structure of mushrooms, and plant material in general, these parameters are likely to be important.[48] In this article we present the results of mushroom imaging at various magnetic field strengths and echo times. The image contrast is discussed in relation to the ultrastructure and water distribution.

THEORY

The signal intensity in a multiecho pulse sequence containing Carr–Purcell–Meiboom–Gill (CPMG)-like signal decay is given by[16,29]:

$$S(t) = S(0)\left\{1 - \exp\left(\frac{-T_r}{T_1}\right)\right\}\left\{\exp\left(\frac{-t}{T_2}\right)\right\} \quad (1)$$

Here, t represents the time after excitation at $N \times T_e$, $S(t)$ the signal intensity at time t, and $S(0)$ the signal intensity at time t=0 (cf. Fig. 1b). T_r presents the repetition time, T_e the echo time between the 180 pulses, and N the counting number of the echo. $S(t)$ is characterized by the spin-lattice relaxation time T_1 and the spin–spin relaxation time T_2.

By choosing $T_r >> T_1$, T_1 relaxation does not contribute to the intensity $S(t)$ in the resulting image. The observed T_2 decay in an image is usually an apparent T_2 which is the summation of various T_2-reducing contributions. For our present purpose we will take three such contributions into consideration:

$$\frac{1}{T_2} = \frac{1}{T_{2,\text{tissue}}} + \frac{1}{T_{2,\text{read}}} + \frac{1}{T_{2,\text{susc}}} \quad (2)$$

where $T_{2,\text{tissue}}$ represents the spin–spin relaxation time of water in the tissue, related to the tissue ultrastructure; $T_{2,\text{read}}$ the apparent spin–spin relaxation time which results from the presence of read gradients during the imaging experiment; and $T_{2,\text{susc}}$ the apparent spin–spin relaxation time which arises from magnetic susceptibility inhomogeneities. The reduction by the last two terms in Eq. (2) is mainly caused by self-

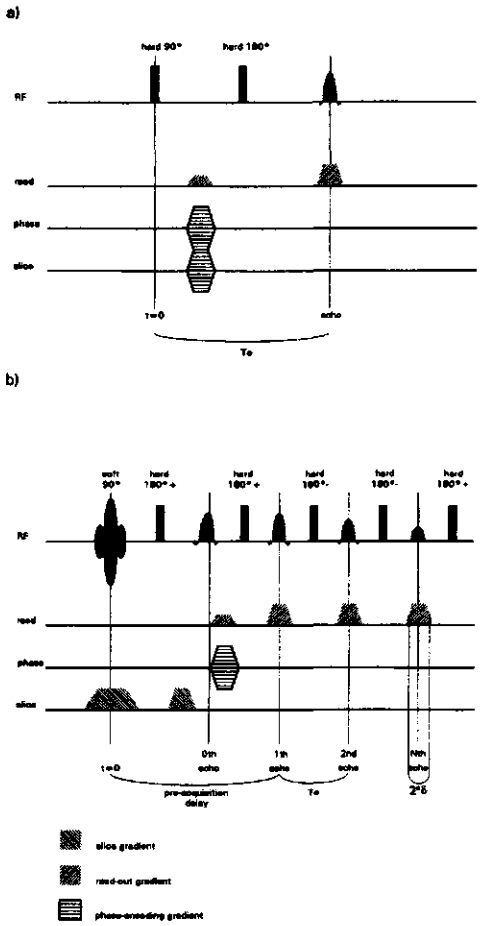

Fig. 1. Pulse sequences for 3D spin echo imaging at 9.4 T (a) and multiecho imaging at both 4.7 and 0.47 T (b).

diffusion through magnetic field gradients, in particular, the read gradient and local gradients due to susceptibility inhomogeneities.[30-36] For the sequence as presented in Fig. 1b, the read gradients contribute to T_2 signal decay according to the following equation:

$$\frac{1}{T_{2,\text{read}}} = \gamma^2 G_{\text{read}}{}^2 \delta^2 \left(1 - \frac{4\delta}{3T_e}\right) D \quad (3)$$

where γ is the nuclear gyromagnetic ratio, G_{read} the strength of the read gradient pulse, δ half the duration

of the read gradient pulse, and D the self-diffusion constant of the molecule containing the observed nucleus. It is assumed that there are no effects due to restricted diffusion.

The tissue structure in a biological sample may cause susceptibility inhomogeneities which induce local field gradients with an unpredictable strength and shape.[37] The contribution of inhomogeneities to T_2 signal attenuation is proportional to the square of the magnetic field B_0, the echo time, and the susceptibility inhomogeneity[38–42,46]:

$$\frac{1}{T_{2,\text{susc}}} \propto \gamma^2 <\chi^2> T_e^2 D \qquad (4)$$

Here, $<\chi^2>$ characterizes the mean square distribution of the local field gradients due to susceptibility inhomogeneities, which is proportional to the square of the externally applied magnetic field B_0. Because of these contributions to the apparent T_2, the final contrast will be influenced by T_e and B_0. This influence will not be homogeneous over an object, but strongly depends on the structure of the object and the region under observation.

To study the influence of the magnetic field strength and echo time, we imaged mushrooms at three values of B_0 and a range of echo times.

MATERIALS AND METHODS

Mushrooms

The mushrooms used for NMR imaging at 9.4 T and for electron microscopy were purchased from a local green grocer. The mushroom used for imaging at 4.7 and 0.47 T was of the cultivar Horst-U1 purchased directly from the mushroom grower and imaged at 4.7 T 1 day after harvest and at 0.47 T 2 days after harvest. Between the experiments the mushrooms were stored at 278 K and at maximum relative humidity.

After the experiment the mushroom used for imaging at 4.7 and 0.47 T was dissected. The cap, stipe, and gill of the mushroom were dried overnight at 353 K to measure the mass percentage water by weighting the mass loss (Table 1).

Table 1. Mass percentages of water in the stipe, cap, and gill of the mushroom applied for multiecho imaging at 0.47 and 4.7 T

Tissue type	Mass % water
Stipe	92.8%
Gill	90.4%
Cap	92.8%

NMR Measurements

One mushroom was imaged at 9.4 T on a Bruker AMX 400 WB (Bruker GmbH, Rheinstetten, Germany) using a three-dimensional (3D) imaging sequence, presented in Fig. 1a, with only hard radiofrequency pulses. Only by applying a very short echo time (T_e = 2.0 ms) could an image be acquired in which the complete mushroom could be recognized. The image was recorded as 64 data points in the read dimension and 64 steps in the phase-encoding dimension. T_r = 2 s, and a sampling rate of 100 kHz was used. The 3D voxel in the image had a volume of 0.47 × 0.47 × 0.47 mm^3. At longer T_e's the mushroom could no longer be recognized in the image.

A second mushroom was imaged at both 4.7 and 0.47 T. At 4.7 T, we used a Spectroscopy Imaging Systems imager (Varian Associates, Fremont, CA) with a 40-cm-diameter bore using a high-resolution insert; at 0.47 T an imager was used consisting of a Bruker electromagnet with a 10-cm air gap, an SMIS console (SMIS Ltd., Guildford, UK) and a DOTY probe head (DOTY Scientific, Columbia, OH) with actively shielded gradients and a 3-cm-diameter cylindrical sample space. At both fields T_e = 2.5, 3.5, or 6.0 ms, and T_r = 6 s was used. A multiecho slice-selective imaging sequence was applied to obtain 64 echo images (Fig. 1b). At 4.7 T the first echo was acquired 15.9 ms after excitation with a sampling rate of 60 kHz, whereas at 0.47 T the first echo was at 4.9 ms and the sampling rate was 100 kHz. The first echo time and the sampling rate were dictated by the spectrometer hardware and software.

All images were obtained by Fourier transformation and corrected for phase. The real intensity image was presented with negligible intensity in the imaginary image for all echo images. The pixel size was 0.78 × 0.78 mm^2 and the slice thickness 2 mm. For reference purposes five tubes with Gd-DTPA (Schering AG, Berlin, Germany) solutions of 0.3, 1.0, 3.0, 10.0, and 30.0 mM, respectively, were imaged at both field strengths according to the same protocol with T_e = 2.5 ms and T_r = 6 s.

Exponential Fitting of the Images at 4.7 and 0.47 T

The real part of the phase-corrected multiecho images was fitted on a pixel-by-pixel basis using a monoexponential decay function without baseline, using the Levenberg–Marquart criterion[43] for chi-square minimization. The algorithm was programmed in Interactive Data Language (IDL; RSI, Boulder, CO), operating on a Silicon Graphics Indigo 2 computer. The amplitude images were obtained from the extrapolation of the decay curve to t=0, which was the center of the soft 90° pulse at the start of the applied imaging sequence.

Electron Microscopy

Tissue pieces from a fresh mushroom were rapidly frozen in liquid nitrogen and glued to a brass sample holder with Tissue Tek, OCT compound no. 4583 (Miles Laboratories, Elkhart, IN). The frozen samples were milled in a cryo-ultramiller of the type "poly cut e" (Reichert & Jung GmbH, Nußloch, Germany).

Subsequently, the samples were cryoetched for approximately 30 min in a cryotech CT 1000 (Oxford Instruments Ltd., Oxford, UK) at a temperature of 183 K of the sample holder and the anticontaminator at 83 K. The samples were sputter-coated with gold for 2 min before recording the electron microscopy photographs using an SEM 535 electron microscope (Philips Export B.V., Eindhoven, The Netherlands), operating at 15.2 kV accelerating voltage, with a temperature of 113 K of the sample holder and the anticontaminator at 88 K.

RESULTS

NMR Images at Various Magnetic Field Strengths

In Fig. 2 16 slices of a 3D image set of a mushroom obtained at a field strength of 9.4 T are presented. The images show signal intensity at various locations in the mushroom. However, the intensity is not homogeneously distributed over the image. The stipe and the gill have comparable intensities, whereas the cap has an intensity ranging from 20% to 50% of the intensity in the stipe.

A void of 10 × 8 pixels is visible in the cap, in slices 10–13. Only one pixel in the center of the void has twice the signal intensity of the noise level. This pixel is surrounded by two regions: first, a region with a constant low intensity about two pixels wide; and second, a ring of about three pixels with a higher intensity and a sharp edge. On inspection of the entire 3D image this two band structure appears to enclose the void in all three dimensions. However, no void was observed on visual inspection of the mushroom after the experiment. Accordingly, no irregularities were observed in the stipe of the imaged mushroom, although the images suggest otherwise.

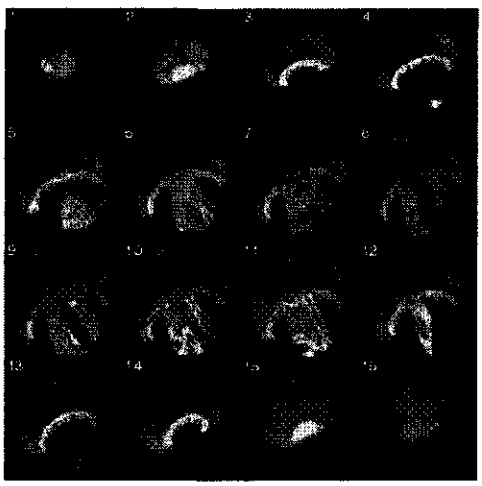

Fig. 2. Sixteen 2D slices of a 3D magnitude image of a mushroom at 9.4 T. T_e = 2.0 ms; T_r = 2 s; 64 data points; 64 phase-encoding steps in both phase-encoding directions, averaged twice; sampling rate 100 kHz.

The multiecho images of the mushroom obtained at 4.7 T show remarkable differences in signal intensity between the cap, core of the stipe, outer stipe, and gill; the first two have almost no intensity and the latter two have about maximum signal intensity (Fig. 3a). A distinct effect is observed due to an increase in the echo time. The fastest signal decay is found at T_e = 6 ms, which is the longest echo time applied. Nowhere in this multiecho image is there much signal intensity left in the last echo, whereas the images with T_e = 2.5 and 3.5 ms still have some signal intensity left, especially in the outer stipe. The cap is hardly visible at all three echo times, not even in the first echo.

The Gd-DTPA reference tubes display corresponding behavior of differing T_2's. The tube with the highest Gd-DTPA concentration is already barely visible in the first echo, where the other tubes lose their signal intensity less quickly corresponding to their decreasing Gd-DTPA concentrations, as was expected for reference tubes with an increasing concentration of paramagnetic ions.

The same mushroom imaged at 0.47 T 1 day after the 4.7-T measurement shows a more or less homogeneously distributed signal intensity in the first echo (Fig. 3b). Only the inner stipe does not have much signal intensity. Again, the signal decays fastest at T_e = 6 ms, but even in that case, the cap still has signal intensity in the 64th echo.

Three of five Gd-DTPA reference tubes have equal maximum signal intensity in the first echo. The decay of the signal intensity corresponds to the Gd-DTPA concentrations in the various tubes.

The calculated T_2 and amplitude images, obtained by a monoexponential fit of each pixel in the multiecho images of the mushroom and the five reference tubes as obtained at 4.7 and 0.47 T, are presented in Figure 4.

Figure 5 shows typical decay curves of one pixel, arbitrarily picked from the center of the five Gd-DTPA reference tubes at both 4.7 T (Fig. 3a) and 0.47 T (Fig. 3b). The calculated averaged T_2 and amplitude values of 12 pixels, randomly picked from the images of each reference tube, are presented in Table 2.

The T_2 values of identical reference tubes do not differ significantly at 4.7 and 0.47 T. The amplitude

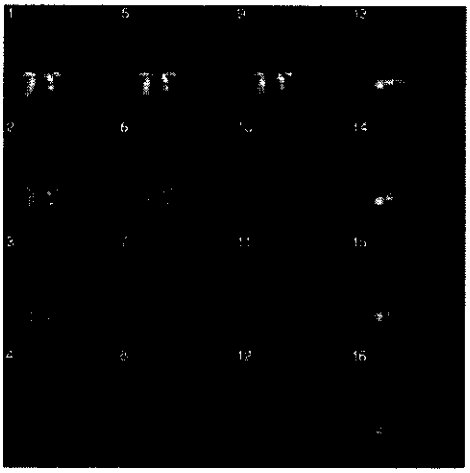

(a)

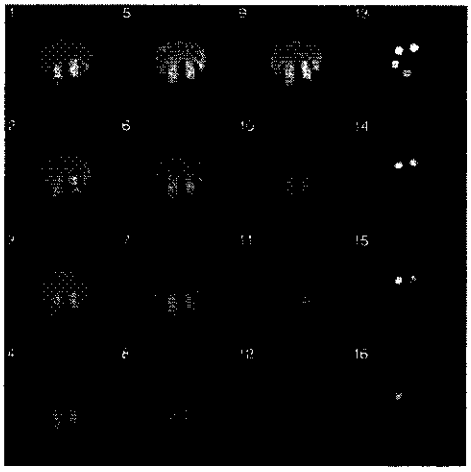

(b)

Fig. 3. Slice-selective, phase-sensitive real images of one mushroom, obtained at 4.7 T (a) and 0.47 T (b). The first (images 1, 5, 9, and 13), 16th (images 2, 6, 10, and 14), 32nd (images 3, 7, 11, and 15) and 64th echo images (images 4, 8, 12, and 16) of the mushroom and the Gd-DTPA reference tubes are presented. T_e = 2.5 (images 1–4), 3.5 (images 5–8), or 6.0 ms (images 9–12) for the mushroom and 2.5 ms for the Gd-DTPA reference tubes (images 13–16); T_r = 6 s; 64 data points; 64 phase-encoding steps; 64 echo s; sampling rate 60 kHz at 4.7 T and 100 KHz at 0.47 T. The images were not filtered or zero-filled.

of the tubes with 0.3, 1.0, 10.0, and 30.0 mM Gd-DTPA imaged at 0.47 T corresponds well with the maximum intensity of 250 arbitrary units (a.u.), where the amplitudes of the tubes imaged at 4.7 T differ significantly from 250 arbitrary units (a.u.). The amplitude of a pixel full of water ought to be around 250 a.u. In the images at 0.47 T, this amplitude value is within the standard deviation for all five tubes, whereas in the images at 4.7 T amplitude is lost, especially in the central tube with the 3.0-mM Gd-DTPA solution.

The amplitude and T_2 values of the different parts of the mushroom observed in Fig. 4 are summarized in Table 3. The amplitude images obtained at 0.47 T show the individual parts of the mushroom, each with a constant amplitude, except for the core of the stipe, which has a very low amplitude. The amplitude images of the same mushroom imaged at 4.7 T are inhomogeneous. The amplitude in the cap is too low in view of the results obtained at 0.47 T and of the mass percentages water presented in Table 1.

The T_2 images obtained at 4.7 T show T_2 values for the cap from around 50 ms in the image with T_e = 2.5 ms, going down to < 10 ms in the image with T_e = 6.0 ms. Here, T_2 approaches the echo time and is therefore not accurately determined, but the decrease is still significant. The outer stipe, however, has a stable T_2 over the various echo times of about 110 ms. The outer stipe in the T_2 images extends more into the core of the stipe than it does in the amplitude images. The gill has an average T_2 of 70 ms. The T_2 in the images obtained at 0.47 T decrease gradually at increasing echo times. In the outer stipe, the T_2 is initially around

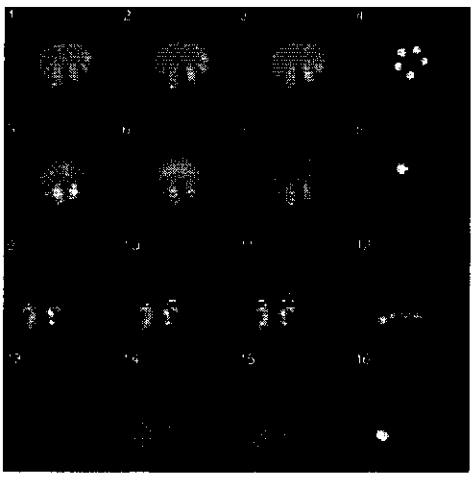

Fig. 4. Calculated amplitude and T_2 images of the multiecho images partly presented in Fig. 3, at 0.47 T (images 1–8) and 4.7 (images 9–16). The amplitude images (images 1–4 and 9–12) are linear scaled from 0 to 250 a.u. and the T_2 images (images 5–8 and 13–16) linear from 0 to 400 ms.

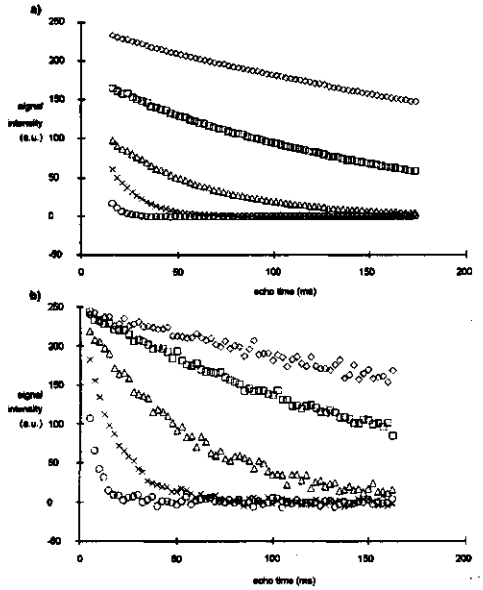

Fig. 5. Typical decay curves of one pixel out of the center of each reference tube Gd-DTPA with: ◇ 0.3 mM; □ 1.0 mM; △ 3.0 mM; × 10.0 mM; and ○ 30.0 mM at 4.7 T (a) and 0.47 T (b); signal intensity (a.u.) versus echo time, $N \times T_e$ (ms).

300 ms, at which it decreases to 260 ms; and in the cap the T_2 at $T_e = 2.5$ ms is 220 ms, at which it reduces to 160 ms at $T_e = 6.0$ ms. The gill has a constant T_2 of around 100 ms.

Table 2. Amplitude and T_2 values of the five Gd-DTPA reference tubes at 4.7 and 0.47 T

Field (T)	Gd-DTPA (mM)	Amplitude (a.u.)	SD	T_2 (s)	SD
4.7	0.3	227	20	0.346	0.008
	1.0	200	40	0.152	0.002
	3.0	161	38	0.053	0.001
	10.0	185	39	0.016	0.001
	30.0			±0.005	
0.47	0.3	243	4.0	0.36	0.02
	1.0	247	7.8	0.159	0.004
	3.0	247	5.3	0.055	0.002
	10.0	242	3.3	0.0171	0.0003
	30.0	248	11	0.0055	0.0003

The values are averaged over 12 pixels originating from one reference tube in the amplitude and T_2 images. The presented errors are standard deviations of the distribution of amplitude and T_2 values. The 30-mM reference tube in the images at 4.7 T could not be fitted because of a too-low signal intensity. In Fig. 5, a typical decay curve of each reference tube is presented.

Table 3. Typical T_2 and amplitude values of the distinct tissue types of a mushroom imaged at 4.7 and 0.47 T at various echo times (T_e)

Field (T)	T_e (ms)	T_2 (ms) stipe	T_2 (ms) gill	T_2 (ms) cap
4.7	2.5	120	80	50
	3.5	110	70	30
	6.0	100	60	10
0.47	2.5	300	100	260
	3.5	280	100	240
	6.0	260	100	160
Field (T)	T_e (ms)	Amplitude stipe (a.u.)	Amplitude gill (a.u.)	Amplitude cap (a.u.)
4.7	2.5	220	220	15
	3.5	225	220	15
	6.0	230	220	20
0.47	2.5	160	160	108
	3.5	165	160	108
	6.0	170	165	100

The approximate values were obtained from Fig. 4.

Fitting of a monoexponential function to the decay is demonstrated by a residue plot of an arbitrarily picked pixel from the cap of a mushroom image at 0.47 T in Fig. 6.

Electron Microscopy (EM) Photographs

Scanning EM photographs are presented in Fig. 7. Figure 7a shows the transition zone between the cap (left) and the gill (right). The tissue structure differs remarkably. The cap has an open structure with air spaces of an average estimated size of 80 μm (Fig. 7b). The fraction of air space in the cap is as much as 50% of the total volume of the cap. The gill, however, does not have air spaces of the same dimensions and volumes. The tissue structure in the gill is more dense than it is in the cap (Fig. 7c). The fraction of air spaces in the gill is about 25%, which is significantly different from the cap.

In Fig. 7d the structure of outer stipe tissue is pre-

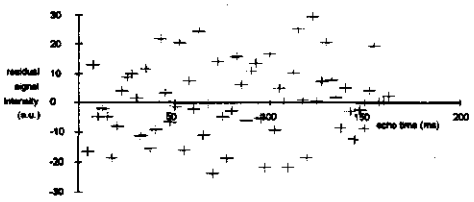

Fig. 6. Residue plot of one arbitrarily picked pixel from the cap of a mushroom image at 0.47 T; signal intensity (a.u.) versus echo time, $N \times T_e$ (ms).

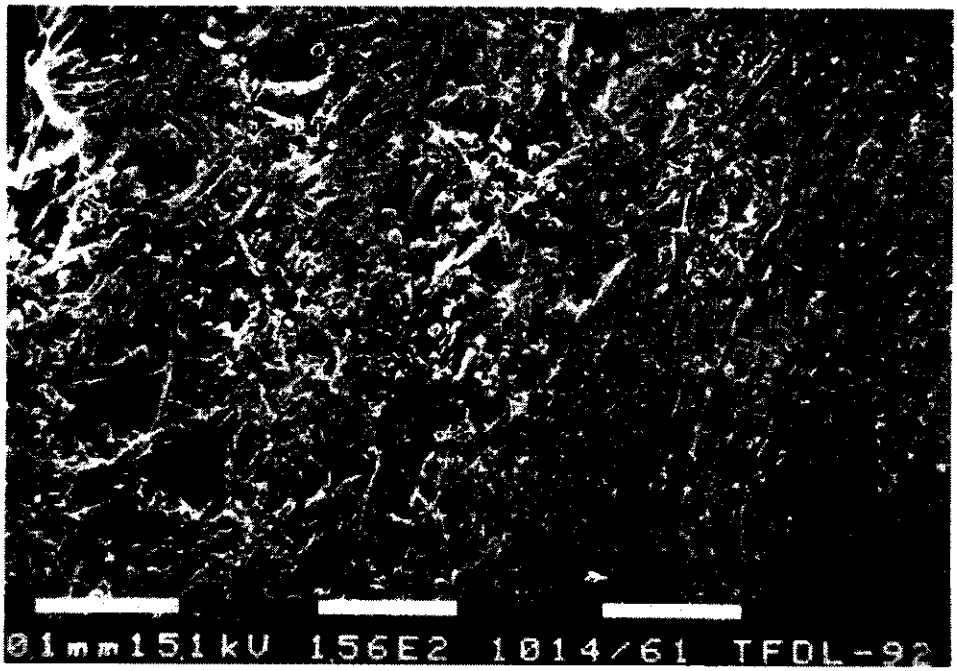
0.1mm15.1kV 156E2 1014/61 TFDL-92

(a)

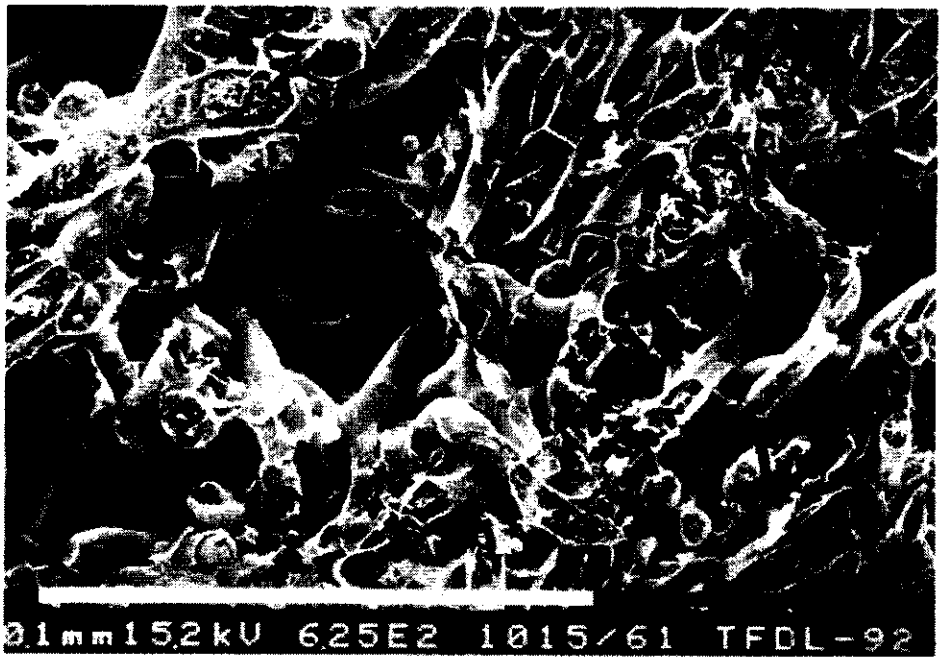
0.1mm15.2kV 625E2 1015/61 TFDL-92

(b)

(c)

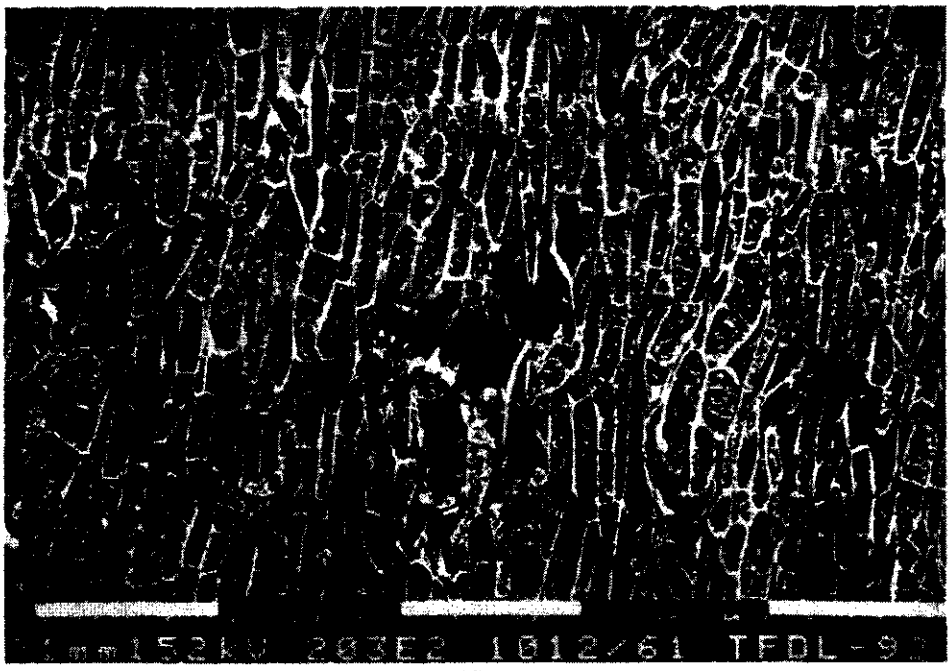

(d)

sented. The cells have an orientation in the direction of the stipe. There are air spaces present in the stipe, although their size is smaller than the spaces present in the cap and their occurrence is rarer. These spaces also make < 25% of the total volume of the stipe. The inner stipe has a structure more like cap tissue.[4]

DISCUSSION AND CONCLUSIONS

In this study, we tried to understand NMR images of the mushroom *A. bisporus*, to quantify the water distribution. Images at 9.4 T were very sensitive to the applied echo time. Only by applying a very short echo time of 2 ms were images obtained in which the cap could be recognized. This short echo time could be obtained by using a 3D image sequence. The signal intensity in the cap of these images was much too low with respect to the almost similar amounts of water in the stipe and the cap of the mushroom (Table 1). Voids in the tissue structure caused artefacts in the images which had larger sizes than the void itself.

At lower field strengths, multiecho images were acquired. This type of images gives access to quantitative water information via T_2 decay of the NMR signal.[26~28,47] A suitable pulse sequence was implemented on two different imagers operating at 4.7 and 0.47 T.

The signal intensity in the first echo image of the Gd-DTPA reference tubes at 4.7 T did not present a signal intensity which could be related to the equal amount of water per tube, and at 0.47 T only the intensity of the three tubes with the lowest Gd-DTPA concentration could be more or less related to the amount of water per tube. It was therefore essential to recover the amplitude and T_2 values per pixel from the decay in the multiecho images. These analyses showed well-recovered T_2 and amplitude values for the Gd-DTPA tubes imaged at 0.47 T. The T_2 of the tubes imaged at 4.7 T were well recovered, whereas the amplitudes recovered less well. The reference tube with the highest Gd-DTPA concentration could not be recovered at 4.7 T.

The four Gd-DTPA reference tubes with the lowest Gd-DTPA concentrations have identical T_2's at both fields, which convinced us that the T_2's were properly determined and appeared to be equal at both fields. The amplitude images at 0.47 T represent well the amount of water per tube. At 4.7 T, the amplitudes are more difficult to interpret because these images still have artefacts and show loss of signal intensity in the central regions of the image. This loss of amplitude is probably caused by B_1 inhomogeneity.

Comparing the T_2's of the mushroom at both field strengths and at different echo times, we find that the T_2 in the cap decreases much faster with increasing field strength or echo time than in the stipe and gill. The fact that the Gd-DTPA reference tubes at both fields have comparable T_2's indicates other T_2-reducing mechanisms to influence the T_2 of water in the cap. Theoretically, two causes for T_2 reduction were mentioned: diffusion of spins through the read gradient, and diffusion of spins through gradients caused by susceptibility inhomogeneities [Eqs. (3) and (4), respectively]. Estimated contributions of the read gradient to T_2 are presented in Table 4 as relaxation rates. All of these $\frac{1}{T_2}$'s are much shorter than 1.0 s^{-1} and therefore cannot reduce the observed T_2's significantly. The observed changes in T_2's are larger and therefore need to have another origin.

The influence that local gradients caused by susceptibility inhomogeneities have on images has already been studied in theory[44] and in phantoms.[37,45] In biological samples susceptibility inhomogeneities induce regions with strongly reduced signal intensity, which can be helpful in morphological studies, but make it difficult correctly to quantify the amount of water present in such an object on the basis of only a single echo image.[24,25]

It is evident that in the present experiments, the strongest T_2 reduction is observed in tissue with the largest amount of extracellular air spaces in the cap and inner stipe. From the EM photographs, it becomes clear that the cap has a high amount of large air spaces, in contrast to the (outer) stipe and gill. These air spaces result in susceptibility inhomogeneities, causing local gradients with an unknown orientation and strength, and increasing at higher field strength. Since the susceptibility inhomogeneities are reflected by $<\chi^2>$ in Eq. (4), the cap is likely to have a more reduced T_2 than the gill and outer stipe at increasing field strength or echo time.

In the mushroom, extended regions with susceptibility inhomogeneities, mainly in the cap, cause major problems in relating the signal intensity of single echo images to the water distribution. However, the amount of water can be determined properly after fitting the decay in multiecho images. Even water with short T_2's could be determined quantitatively in this way. The multiecho images of the mushroom were fitted with a monoexponential function, which is reasonable because the residue plots did not indicate more exponents to be present in the decay at the actual number of data points and the signal-to-noise ratio (Fig. 6).

The observed T_2 values can be well explained by the susceptibility inhomogeneities in the various types of tissue. The T_2 in the cap, imaged at 0.47 T, is more

Fig. 7. Electron microscope photographs of mushroom tissue. (a) Overview of the cap and inner gill; (b) detail of cap tissue taken from the centre of the cap; (c) detail of gill tissue; (d) outer stipe located close to the cap. The bar represents 100 μm.

Table 4. Estimation of the apparent $1/T_2$ contribution by the read gradient to the observed T_2 in the images acquired at both 4.7 and 0.47 T, according to Eq. (3)

T_r (ms)	$1/T_2$ (s^{-1}) at 0.47 T	$1/T_2$ (s^{-1}) at 4.7 T
2.5	0.12	0.034
3.5	0.15	0.041
6.0	0.17	0.047

The differences between the two fields is found in the different values for δ, caused by differing data sampling methods at both imagers.

reduced than the T_2 in the gill and outer stipe. The large influence of the B_0 field is well demonstrated by the large reduction of T_2's at 4.7 T and the almost inaccessibly short T_2 values at 9.4 T. At 4.7 T the T_2 of the cap is so reduced that it becomes shorter than the applied echo time, resulting in unreliable extrapolation to zero time in the fitting procedure.

The best way to obtain quantitative NMR images related to water distributions is to image at low field (<2 T?) and apply echo times which are as short as possible (around 3 ms; this value depends on the field strength). Only then can the influence of susceptibility inhomogeneities be reduced to a minimum, allowing the interpretation of the calculated amplitude images as water distribution images. This is emphasized by the fact that the first echo images of the mushroom obtained at 0.47 T and the corresponding calculated amplitude approximately have the same contrast. The calculated amplitude images have less spreading of the pixel intensity and therefore better present the amount of water per pixel.

This conclusion is supported by the fact that the mass percentages water in the cap and stipe are equal within 0.1% (Table 1, determined at the end of the experiment). The difference between the amplitude in the cap and the outer stipe (Table 3b) is therefore fully accounted for by the difference in tissue density, which is around 0.75 g/ml for the outer stipe and around 0.5 g/ml for the cap. The actual tissue density of mushroom tissue is hard to determine because of its variation in the amount of absorbed water in the extracellular spaces. These values are therefore only indicative. The ratio between the cap and outer stipe in the amplitude images at 0.47 T is 0.66; likewise for the ratio in tissue density, in contradiction to the ratio in the images acquired at 4.7 T. Here, the amplitudes in the mushroom may be artificially increased owing to normalization problems on the signal amplitudes of the reference tubes (Fig. 5). Normalization at 4.7 T is based on only the tube with the lowest Gd-DTPA concentration, and all other tubes have much lower intensity. It is not clear from the results presented in Fig. 5a that the first tube has the correct signal intensity.

This study demonstrates that strong susceptibility inhomogeneities are present in mushrooms. Their influence can be reduced by applying low field strengths and short echo times. Only then can the amplitude images give a faithful representation of the water distribution. Multiecho images at low field seem to offer great advantage in these kind of studies despite the lower sensitivity at lower field strength. Further investigations will be needed to make a quantitative estimation of the influence susceptibility inhomogeneities have on the T_2 of water in mushrooms.

Acknowledgements—The authors thank T.J. Schaafsma and L.J.L.D. van Griensven for carefully reading and discussing the manuscript. The project was financially supported by the State Institute for Quality Control of Agricultural Products (RIKILT-DLO) at Wageningen, The Netherlands. Part of this work was carried out at The Netherlands in vivo NMR facility at the Bijvoet Center for Biomolecular Research, which is supported by The Netherlands Organization for Scientific Research (NWO).

REFERENCES

1. Flegg, P.B.; Spencer, D.M.; Wood, D.A. (Eds.) The Biology and Technology of the Cultivated Mushroom. Chichester: Wiley; 1985.
2. Boekestein, A.; Hulsteyn, K.; Hesen, L.P.W.; van Griensven, L.J.L.D. Cryo-scanning electron microscopy of mushroom tissue. Scanning 15:171–173; 1993.
3. Jasinski, E.M.; Stemberger, B.; Kilara, A. Ultrastructural studies of raw and processed tissue of the major cultivated mushroom, *Agaricus bisporus*. Food Microstruc. 3:191–196; 1984.
4. Wood, D.A.; Craig, G.D.; Atkey, P.T.; Newsam, R.J.; Gull, K. Ultrastructural studies on the cultivation process and growth and development of the cultivated mushroom *Agaricus bisporus*. Food Microstruc. 4:143–164; 1985.
5. Atkey, P.T. The scanning electron microscope in mushroom research. Mushroom J. 129:241–244; 1983.
6. Atkey, P.T.; Nichols, R. Surface structure of *Agaricus bisporus* by scanning electron microscopy. Mushroom J. 129:334–335; 1983.
7. Ishida, N.; Kobayashi, T.; Koizumi, M.; Kano, H. 1H-NMR imaging of tomato fruits. Agric. Biol. Chem. 53:2363–2367; 1989.
8. Chen, P.; McCarthy, M.J.; Kauten R. NMR for internal quality evaluation of fruits and vegetables. Am. Soc. Agric. Eng. 32:1747–1753; 1989.
9. Wang, C.Y.; Wang, P.C. Nondestructive detection of core breakdown in "Bartlett" pears with nuclear magnetic resonance imaging. Hort. Sci. 24:106–109; 1989.
10. Wang, S.Y.; Wang, P.C.; Faust, M. Nondestructive detection of watercore in apple with nuclear magnetic resonace imaging. Sci. Hort. 35:227–234; 1988.
11. McCarthy, M.J.; Perez, E.; Ozilgen, M. Model for transient moisture profiles of a drying apple slab using the data obtained with magnetic resonance imaging. Biotech. Prog. 7:540–543; 1991.
12. Johnson, G.A.; Brown, J.; Kramer, P.J. Magnetic reso-

nance microscopy of changes in water content in stems of transpiring plants. Proc. Natl. Acad. Sci. USA 84:2752–2755; 1987.
13. Veres, J.S.; Johnson, G.A.; Kramer, P.J. In vivo magnetic resonance imaging of Blechnum ferns: Changes in T_1 and N(H) during dehydration and rehydration. Am. J. Bot. 78:80–88; 1991.
14. Brown, D.P.; Pratum, T.K.; Bledsoe, C.; Ford, E.D.; Cothern, J.S.; Perry, D. Noninvasive studies of conifer roots—nuclear magnetic resonance (NMR) imaging of Douglas-fir seedlings. Can. J. Forest Res. 21:1559–1566; 1991.
15. McCarthy, M.J.; Kauten, R.J. Magnetic resonance imaging applications in food research. Trends Food Sci. Technol. 134:139; 1990.
16. Callaghan, P.T. Principles of Nuclear Magnetic Resonance Microscopy. Oxford: Clarendon Press; 1991.
17. Belton, P.S.; Ratcliffe, R.G. NMR and compartiment in biological tissues. Prog. NMR Spectrosc. 17:241–279; 1985.
18. Ahn, C.B.; Chu, W.C. Optimal imaging strategied for three-dimensional nuclear resonance microscopy. J. Magn. Reson. Imaging 94:455–470; 1991.
19. Schneiders, N.J.; Ford, J.; Bryan, R.N.; Willcott, M.R. Accurate T_2 NMR images. Med. Phys. 10:642–645; 1983.
20. Colire, C.; Rumeur, E.L.; Gallier, J.; de Certaines, J.; Larher, F. An assessment of the proton nuclear magnetic resonance as an alternative method to describe water status of leaf tissues in wilted plants. Plant Physiol. Biochem. 26:767–776; 1988.
21. Snaar, J.E.M.; Van As, H. Probing water compartments and membrane permeability in plant cells by 1H NMR relaxation measurements. Biophys. J. 63:1654–1658; 1992.
22. Monteiro Marques, J.P.; Rutledge, D.N.; Ducauze C.J. Low resolution pulse nuclear magnetic resonance study of carrots equilibrated at various water activities and temperatures. Sci. Aliments 11:513–525; 1991.
23. Link, J.; Seelig, J. Comparison of deuterium NMR imaging methods and applications to plants. J. Magn. Reson. Imaging 89:310–330; 1990.
24. Veres, J.S.; Cofer, G.P.; Johnson, G.A. Distinguishing plant tissues with magnetic resonance microscopy. Am. J. Bot. 78:1704–1711; 1991.
25. Duce, S.L.; Carpenter, T.A.; Hall, L.D.; Hills, B.P. An investigation of the origins of contrast in NMR spin echo images of plant tissue. Magn. Reson. Imaging 10:289–297; 1992.
26. Araujo, C.D.; Mackay, A.L.; Hailey, J.R.T.; Whittall, K.P.; Le, H. Proton magnetic resonance techniques for characterization of water in wood—Application to white spruce. Wood Sci. Technol. 26:101–113; 1992.
27. Menon, R.S.; Mackay, A.L.; Flibotte, S.; Hailey, J.R.T. Quantitative seperation of NMR images of water in wood on the basis of T_2. J. Magn. Reson. Imaging 82:205–210; 1989.
28. Flibotte, S.; Menon, R.S.; MacKay, A.L.; Hailey, J.R.T. Proton magnetic resonance of western red cedar. Wood Fiber Sci. 22:362–376; 1990.
29. Mulkern, R.V.; Patz, S.; Brooks, M.; Metcalf, D.C.; Jolesz, F.A. Spin-lock techniques and CPMG imaging sequences: A critical appraisal of $T_{1\rho}$ contrast at 0.15 T. Magn. Reson. Imaging 7:437–444; 1989.
30. Hahn, E.L. Spin echoes. Phys. Rev. 80:580–594; 1950.
31. Carr, H.Y.; Purcell, E.M. Effect of diffusion on free precession in nuclear magnetic resonance experiments. Phys. Rev. 94:630–638; 1954.
32. Bihan, D.L. Molecular diffusion nuclear magnetic resonance imaging. Magn. Reson. Q. 7:1–30; 1991.
33. Stilbs, P. Fourier transform pulsed-gradient spin-echo studies of molecular diffusion. Prog. NMR Spectrosc. 19:1–45; 1987.
34. Bihan, D.L.; Turner, R.; Moonen, C.T.W.; Pekar, J.P. Imaging of diffusion and microcirculation with gradient sensitization: Design, strategy, and significance. J. Magn. Reson. Imaging 1:7–28; 1991.
35. Gibbs, S.J.; Carpenter, T.A.; Hall, L.D. Diffusion imaging with unshielded gradients. J. Magn. Reson. Imaging 98:183–191; 1992.
36. Hyslop, W.B.; Lauterbur, P.C. Effects of restricted diffusion on microscopic NMR imaging. J. Magn. Reson. Imaging 94:501–510; 1991.
37. Posse, S.; Aue, W.P. Susceptibility artifacts in spin-echo and gradient-echo imaging. J. Mag. Reson. Imaging 88:473–492; 1990.
38. Bihan, D.L.; Turner, R.; Macfall, J.R. Effect of intrafoxel incoherent motions (IVIM) insteady-state free precession (SSFP) imaging: Application to molecular diffusion imaging. Magn. Reson. Med. 10:324–337; 1989.
39. Meyer, R.A.; Brown, T.R. Diffusion measurements by microscopic imaging. J. Magn. Reson. Imaging 76:393–399; 1988.
40. Brownstein, K.R.; Tarr, C.E. Importance of classical diffusion in NMR studies of water in biological cells. Phys. Rev. A. 19:2446–2453; 1979.
41. Brownstein, K.R.; Tarr, C.E. Spin-lattice relaxation in a system governed by diffusion. J. Magn. Reson. Imaging 26:17–24; 1977.
42. Brownstein. K.R. Diffusion as an explanation of observed NMR behavior of water absorbed on wood. J. Magn. Reson. Imaging 40:505–510; 1980.
43. Press, W.H.; Teukolsky, S.A.; Vetterling, W.T.; Flannery, B.P. (Eds.) Numerical Recipes., 2nd ed. Cambridge: Cambridge University Press; 1992.
44. Zhong, J.H.; Kennan, R.P.; Gore, J.C. Effects of susceptibility variations on NMR measurements of diffusion. J. Magn. Reson. Imaging 95:267–280; 1991.
45. Zhong, J.; Gore, J.C. Studies of restricted diffusion in heterogeneous media containing variations in susceptibility. Magn. Reson. Med. 19:276–284; 1991.
46. Majumdar, S.; Gore, J.C. Studies of diffusion in random fields produced by variations in susceptibility. J. Magn. Reson. Imaging 78:41–55; 1988.
47. Kuchenbrod, E.; Haase, A.; Benkert, R.; Schneider, H.; Zimmerman, U. Quantitative NMR microscopy on intact plants. Magn. Reson. Imaging 13:447–455; 1995.
48. Connely, A.; Lohman, J.A.B.; Loughman, B.C.; QuiQuampoix, H.; Ratcliffe, R.G. High resolution imaging of plant tissues by NMR. J. Exp. Bot. 38:1713–1723; 1987.

4

QUANTITATIVE ^{1}H-NMR IMAGING OF WATER IN WHITE BUTTON MUSHROOMS (*AGARICUS BISPORUS*)

published as:

Donker, H.C.W., Van As, H., Snijder, H.J. & Edzes, H.T.; Quantitative ^{1}H-NMR imaging of water in white button mushrooms (*Agaricus bisporus*); Magn. Reson. Imag. (1997); 15: 113-121.

ELSEVIER

Magnetic Resonance Imaging, Vol. 15, No. 1, pp. 113–121, 1997

● *Original Contribution*

QUANTITATIVE ^{1}H-NMR IMAGING OF WATER IN WHITE BUTTON MUSHROOMS (*AGARICUS BISPORUS*)

H.C.W. DONKER, H. VAN AS, H.J. SNIJDER AND H.T. EDZES

Department of Molecular Physics, Agricultural University, Dreijenlaan 3, 6703 HA Wageningen, The Netherlands

MRI represents a valuable tool for studying the amount and physical status of water in plants and agricultural products, for example, mushrooms (*Agaricus bisporus*). Contrast in NMR images originates from the mixed influence of the fundamental NMR parameters, amongst others, spin-density, T_2- and T_1 relaxation processes. Maps of these parameters contain valuable anatomical and physiological information. They can, however, be severely distorted, depending on the combination of parameter settings and anatomy of the object under study. The influence of the tissue structure of mushrooms, for example, tissue density (susceptibility inhomogeneity) and cell shape on the amplitude, T_2, and T_1 images is analyzed. This is achieved by vacuum infiltration of the cavities in the mushroom's spongy structure with Gd-DTPA solutions and acquiring Saturation Recovery-Multispin Echo images. It is demonstrated that the intrinsic long T_2 values in the cap and outer stipe tissue strongly relate to the size and geometry of the highly vacuolated cells in these spongy tissues. All observed T_2 values are strongly affected by susceptibility effects. The T_2 of gill tissue is shorter than T_2 of the cap and outer stipe, probably because these cells are less vacuolized and smaller in size. The calculated amplitude images are not directly influenced by susceptibility inhomogeneities as long as the observed relaxation times remained sufficient long. They reflect the water distribution in mushrooms best if short echo times are applied in a multispin echo imaging sequence at low magnetic field strength.

Keywords: **Saturation-recovery multiecho imaging; Vacuum infiltration; Gd-DTPA contrast enhancement; Susceptibility inhomogeneity; Relaxation; Image contrast; Quantitative water density imaging; Plant tissue; Mushrooms; *Agaricus bisporus*.**

INTRODUCTION

Knowledge of the water distribution in the mushroom (*Agaricus bisporus*) is of major interest for studying the postharvest senescence of this economically important crop. NMR imaging gives noninvasively access to this information.

The mushroom is made of cylindrical mycelial cells with a diameter of 20 μm. Mushrooms have a spongy structure with a tissue density of 0.3 to 0.9 g/ml and contain approximately 92% (mass/mass) of water.[1–4] The core of the stipe has a very low tissue density with a broad range of cells in the various developmental stages.[3] The gill has a high tissue density and is usually less vacuolized (<50% volume/volume).[3]

Contrast observed in NMR images depends upon, e.g., the spin-density distribution and the spin-spin (T_2) and spin-lattice (T_1) relaxation times of the protons present in the object under study.[5–8] To study the water distribution of the mushroom, pure amplitude images of the proton spin-density distribution are required.[5,9] Even multiecho images at short echo times (~3 ms) do not garantee to represent pure amplitudes.[10]

Susceptibility inhomogeneities were already found to have a major influence on the observed T_2 from Multispin Echo (MSE) images of mushrooms.[10] The effects of these inhomogeneities increase at higher magnetic fields.[10] Even at relatively low field strength (0.5 T) the T_2 images in our work turned out to be influenced by the applied echo time, indicating that susceptibility contributions cannot be neglected. The corresponding amplitude images were hardly affected. It was not clear, however, whether these images presented the amount of water per pixel quantitatively.

In this article T_2 and T_1 relaxation of protons of

RECEIVED 3/1/96; ACCEPTED 9/3/96.
Address correspondence to H. Van As, Department of Molecular Physics, Agricultural University, Dreijenlaan 3, 6703 HA Wageningen, The Netherlands.

tissue water in the mushroom is analyzed, based on the results obtained from combined Saturation Recovery Multispin Echo (SR-MSE) images and short echo time MSE images. Susceptibility effects, originating from the spongy structure of the mushroom, on the amplitude, T_2 and T_1 images have been studied by using vacuum infiltration of the mushroom with various Gd-DTPA solutions. The relaxation time images were related to tissue structure details (size/geometry of cells/vacuoles). It is demonstrated that in this way quantitative water distribution maps can be obtained.

MATERIAL AND METHODS

Experimental

Three fruit bodies from one batch, being just one typical example of a Horst-U1® mushroom, were purchased from a local green grocer less than 48 h after harvest. The mushrooms were stored at 7°C in a sealed package. First, the original mushrooms were imaged. Each mushroom was consecutively submerged in one of the solutions of 0.6, 2.5, and 10.0 mM Gd-DTPA, prepared from a 0.5 M Gd-DTPA stock solution with a twofold excess of DTPA (Schering AG, Berlin, Germany), and vacuum infiltrated at 20 mm Hg pressure for 10 min in a vacuum exsiccator. Before releasing the vacuum, remaining air bubbles were removed from the solution and from the surface of the fruit body by gently shaking and tapping of the exsiccator. After vacuum infiltration each mushroom was imaged twice to check reproducibility and long timescale effects.

Three SR-MSE images were recorded of each mushroom: before infiltration, 10–30 min after infiltration, and 2 h after infiltration. Two MSE images were acquired of the mushroom infiltrated with 2.5 mM Gd-DTPA solution; one before infiltration and one directly after infiltration. The SR-MSE images were acquired with T_e = 7.5 ms and the MSE images with T_e = 2.5 ms.

From the SR-MSE images, amplitude, T_2, and T_1 images were calculated on a pixel-by-pixel base, assuming mono-exponential decay for both T_2 and T_1 dimension. Decay in both the T_2 and T_1 dimension was fitted simultaneously in the SR-MSE data sets. The MSE images of the mushroom before and after infiltration with 2.5 mM Gd-DTPA solution were also fitted mono-exponentially. Relaxation rate difference images were calculated from $1/T_2$ or $1/T_1$ images by subtracting the relaxation rate before vacuum infiltration from the relaxation rate after vacuum infiltration.

To separate the contribution of the infiltration solution and of the mushroom, the MSE image of the mushroom vacuum infiltrated with 2.5 mM Gd-DTPA solution was also fitted with a biexponential fitting function.

Mass fractions tissue were determined of the vacuum infiltrated cap, outer stipe, and core of the stipe by weighting excised tissue before and after vacuum infiltration with demineralized water. Because mushrooms exist of more than 90% water the mass fraction tissue is a reasonable approximation for the tissue density, at least within the errors of the here presented methods. The mass fractions will be used to compare to the amplitude images.

Data Acquisition and Processing

The mushrooms were imaged on a 0.47 T (20.35 MHz) imager consisting of a Bruker (Bruker Spectrospin GmbH, Rheinstetten, Germany) electromagnet, a SMIS (SMIS Ltd., Guildford, UK) console, and a DOTY (DOTY Scientific Inc., Columbia, USA) customised probe-head with actively shielded gradients. The applied SR-MSE and MSE pulse sequences are presented in Fig. 1.

Typical applied acquisition parameters were: spectral width 100 kHz, no phase cycle, 64 complex data points per transient, 64 phase-encoding gradient steps, and no averaging. For the SR-MSE measurements we used eight increments of 200 ms in the SR time domain and 64 echos with T_e = 7.5 ms, T_r = 3000 ms, a slice thickness of 2.0 mm, and a field of view of 30 mm. MSE images of 512 echos were acquired without the optional initial hard 90°; saturation recovery pulse of the SR-MSE sequence and with T_e = 2.5 ms and T_r = 3000 ms.

The obtained data were first filtered with a Gaussian filter of 0.75 pixel (or 330 Hz per point) and afterwards

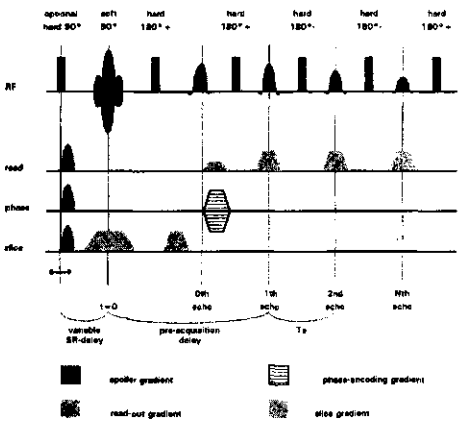

Fig. 1. Applied pulse sequence for the acquisition of the SR-MSE and the MSE images. The initial hard 90° pulse determines the difference between the SR-MSE and MSE imaging pulse sequence.

zero filled once, before fast Fourier transformation and phasing. A mono-exponential fitting function was applied to fit the decay of each pixel (x,y) in the real intensity (SR-) MSE images. This was achieved by calculating an initial guess of the decay constant(s) and amplitude based on linear regression of the initial part of the logarithmic decay curves. With this initial guess, a Levenberg-Marquard nonlinear least square algorithm was applied to obtain the final fit. Iteration of the fit was halted after the chi-square difference became less than 0.1% or after 100 iterations. All data points were weighted equally.

The applied fitting function for the decay of the signal intensity in pixel x,y is given by:[9]

$$S_{x,y}(T_{sr},t) = S_{x,y}(T_{sr} = \infty, t = 0)^{*} \times (1 - \exp[-T_{sr}/T_{1,x,y}])^{*}\exp(-t/T_{2,x,y}) \quad (1)$$

Here, $S_{x,y}(T_{sr},t)$ is the signal intensity at time t in

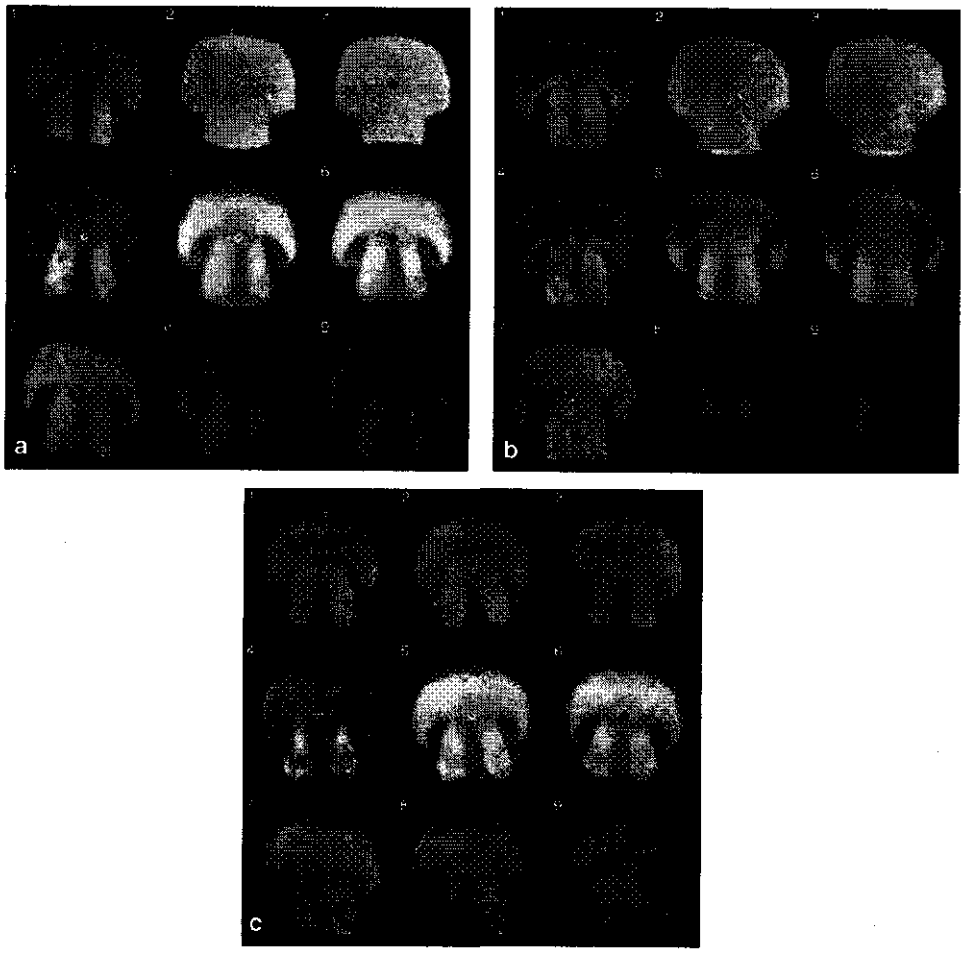

Fig. 2. Calculated amplitude (1–3), T_2 (4–6), and T_1 (7–9) image of a mushroom before [1,4,7], directly after [2,5,8], and 2 h after [3,6,9] vacuum infiltration with 0.6 mM Gd-DTPA solution (a), 2.5 mM Gd-DTPA solution (b), and 10.0 mM Gd-DTPA solution (c). The amplitude images are scaled from 0 to 30,000 arbitrary units (a.u.), the T_2 images from 0 to 400 ms and the T_1 images from 0 to 2500 ms.

the saturation recovery step T_{sr}; $S_{x,y}(t = 0, T_{sr} = \infty)$ the extrapolated amplitude at $t = 0$, representing the spin density; T_2 the transversal relaxation time; T_1 the longitudinal relaxation time; T_{sr} the saturation recovery incrementing delay, and t the time after the soft 90° pulse. Using Equation 1 quantitative amplitude, T_2 and T_1 images are obtained. The accuracy of the parameter values in the fitted images is better than 5% for more than 95% of all fitted pixels.

Estimated amplitude, T_2, and T_1 values for the cap, gill, and stipe before and after vacuum infiltration are presented in the tables, as well as these parameters for the infiltration solutions. These values, obtained by visual parameter estimation, are used to summarise the data of the parameter images and to facilitate the discussion. Presented amplitude values have an estimated error of 10%, T_2 values have an estimated error of 10%, and T_1 values have an estimated error of 20%.

To understand the differences between the images, resulting from various treatments of the mushroom, we calculated difference images of the amplitude images and of the reciprocal relaxation time images:

$$\text{Amplitude: } \Delta S \equiv S_{after} - S_{before} \qquad (2a)$$

$$\text{Relaxation rate: } \Delta R \equiv R_a - R_b \qquad (2b)$$

where $R_a \equiv 1/T$ after treatment, $R_b \equiv 1/T$ before treatment, and T is either a T_2 or T_1 image. S is an amplitude image.

RESULTS

SR-MSE Imaging

Calculated amplitude, T_2, and T_1 images of the mushrooms before, directly after, and 2 h after vacuum infiltration with the three Gd-DTPA solutions, obtained with the SR-MSE imaging pulse-sequence applying T_e = 7.5 ms, are presented in Fig. 2. Their parameter estimations are presented in Tables 1 and 5.

All three mushrooms before vacuum infiltration have comparable T_1 values for the cap and the stipe and a little differing T_1 values for the gill. After vacuum infiltration with Gd-DTPA solution, T_1s of the mushrooms infiltrated with 0.6 mM and 10.0 mM Gd-DTPA change the same way, especially the cap and stipe. T_1 of the gill remained more or less constant. T_1 of the mushroom infiltrated with 2.5 mM decreased most in the cap, gill, and core of the stipe, more than the other two mushrooms did (Table 2a).

The T_2 of a fresh mushroom was different for the cap, stipe, and gill, with the T_2 for the outer stipe being about double the T_2 for the cap and gill. After vacuum infiltration, T_2s of the cap became almost equal to the T_2 of the outer stipe, except for the mushroom infiltrated with 2.5 mM Gd-DTPA. Here, the T_2 of the cap increased less and did not become equal to the T_2 of the outer stipe. The T_2 of the gill increased on infiltration with 0.6 mM Gd-DTPA. This increase gradually changed in a decrease at an increasing Gd-DTPA concentration (Table 1b).

$\Delta S \Delta R2$, and $\Delta R1$ images were calculated from the reciprocal relaxation time images before and directly after vacuum infiltration of Fig. 2, according to Equation 2, and are presented in Fig. 3. The estimated relaxation rates of these images for the various parts of the mushrooms are presented in Table 2.

The amplitude images of the three mushrooms before infiltration did not differ significantly, representing three mushrooms with a comparable signal intensity and signal distribution.

After infiltration, the mushrooms infiltrated with 0.6

Table 1. Estimated $T_1 \pm 20\%$ and $T_2 \pm 10\%$ values of a mushroom before and after vacuum infiltration, imaged with a SR-MSE imaging sequence, applying T_e = 7.5 ms and T_r = 3000 ms, originating from the images presented in Fig. 2

T_1 (s), before infiltration				T_1 (s), after infiltration			T_1 (s)
Cap	Gill	Stipe	Gd-DTPA solution	Cap	Gill	Stipe	infiltrate
1.4	0.3	1.3	0.6 mM	0.8	0.3	1.1	0.30
1.4	0.6	1.4	2.5 mM	0.5	0.4	0.7	0.08
1.2	0.3	1.1	10.0 mM	1.0	0.2	0.8	0.02
T_2 (ms), before infiltration				T_2 (ms), after infiltration			T_2 (ms)
Cap	Gill	Stipe	Gd-DTPA solution	Cap	Gill	Stipe	infiltrate
150	100	300	0.6 mM	300	180	300	220
140	180	230	2.5 mM	180	100	270	60
150	100	280	10.0 mM	300	80	300	16

Table 2. Estimated $\Delta R_1 \pm 30\%$ and $\Delta R_2 \pm 20\%$ on vacuum infiltration with 0.6 mM, 2.5 mM, and 10.0 mM

	ΔR_1 (s^{-1})			
	Cap	Gill	Stipe core	Stipe outer
0.6 mM	−0.5	−1	−1.2	<−0.3
2.5 mM	−2	−3	−3	−0.8
10.0 mM	<−0.3	−2	−0.7	−0.5
	ΔR_2 (s^{-1})			
	Cap	Gill	Stipe core	Stipe outer
0.6 mM	4	1.4	6.6	1
2.5 mM	2	—	—	0.7
10.0 mM	4	<0.7	1.4	0.7

The T_2s reflect increasing T_2s on vacuum infiltration where the T_1s reflect decreasing T_1s on vacuum infiltration, originating from the images presented in Fig. 3.

mM and 2.5 mM solution both presented an increased, constant amplitude per pixel. The amplitude image of the mushroom infiltrated with 0.6 mM Gd-DTPA solution corresponded with the amplitude of the maximum amount of water per pixel of 100% volume/volume.

Fig. 3. ΔS (1–3), ΔR_2 (4–6), and ΔR_1 (7–9) images of three mushrooms infiltrated with 0.6 mM [1,4,7], 2.5 mM [2,5,8] and 10.0 mM [3,6,9] Gd-DTPA solution (Fig. 2). The amplitude images are scaled from 0 to 20,000 a.u., representing the amplitude increase, the R_2 images are scaled from 0 to 10 s^{-1} representing the R_2 increase, and the R_1 images are scaled from 0 to −4.0 s^{-1} representing the R_1 decrease.

It was comparable to the amplitude of the remaining infiltration solution below the cutting surface of this mushroom. The spread of the amplitude per pixel over this entire amplitude image was around 5%. The amplitude image of the mushroom infiltrated with 2.5 mM Gd-DTPA solution was less than the maximum amount of water per pixel. The remaining infiltration solution below the cutting surface of this mushroom had a higher amplitude than the mushroom itself.

The amplitude of the mushroom infiltrated with 10.0 mM Gd-DTPA solution increased around 5% compared to the amplitude of the fresh mushroom. Amplitude, resulting from the infiltration solution, could not be observed below the stipe of this mushroom, in contrast to the results presented in Fig. 2a and b. Amplitude difference images are presented in Fig. 3. Various estimated amplitude values, together with the weighted mass fractions tissue of the excised mushroom parts are presented in Table 5.

The 2 h storage period of the infiltrated mushroom did not have noticeable effects on the amplitude, T_2, and T_1 images.

MSE Imaging

The calculated amplitude and T_2 images of the mono-exponential fit of the original MSE images with

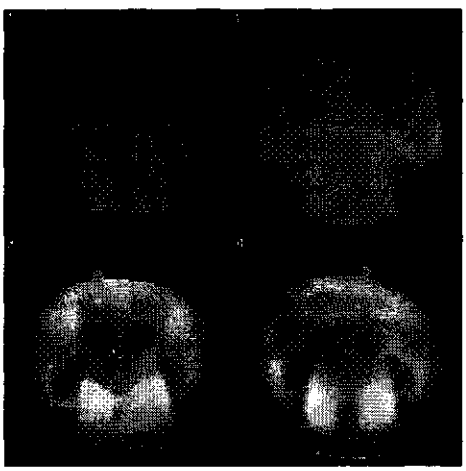

Fig. 4. Calculated amplitude and T_2 images from a MSE pulse sequence, applying T_e = 2.5 ms and T_r = 3000 ms. The images 1 and 2 represent the amplitude image before and after vacuum infiltration with 2.5 mM Gd-DTPA solution and the images 3 and 4 represent the corresponding T_2 images. Because the amplitude images are in arbitrary units, they cannot be compared to the amplitude images presented in Fig. 2. The amplitude images are scaled from 0 to 40,000 a.u. and the T_2 images are scaled from 0 to 400 ms.

Table 3. Estimated T_2 values ± 10% of a mushroom before and after vacuum infiltration, imaged with a MSE imaging sequence, applying T_e = 2.5 ms and T_r = 3000 ms, originating from the images presented in Fig. 4

T_2 (ms), before infiltration				T_2 (ms), after infiltration			T_2 (ms)
Cap	Gill	Stipe	Gd-DTPA Solution	Cap	Gill	Stipe	infiltrate
270	130	320	2.5 mM	250	120	330	60

T_e = 2.5 ms of a mushroom before and after vacuum infiltration with 2.5 mM Gd-DTPA solution are presented in Fig. 4. The corresponding estimated T_2 values are summarized in Table 3.

The amplitude image before infiltration was low for the cap and high for the outer stipe and gill. After vacuum infiltration, the amplitude images became more homogeneous, but the amplitude in the cap was still low compared to that of other parts of the mushroom.

This dataset was also fitted biexponentially, in an attempt to separate the signal from the mushroom and the infiltration solution. The amplitude and T_2 images of both fractions obtained from this biexponential fit are presented in Fig. 5; the corresponding numerical values are summarized in Table 4. The amplitude values are compared to other amplitude values in Table 5.

As can be seen in Fig. 5 and Table 4, two fractions could be separated, but not completely over the entire mushroom. Especially in the core of the mushroom two identical T_2s with extremely variable amplitudes are found, indicating single exponential behavior. In the region close to the cutting surface, the two exponentials could not be discriminated easily either, probably because of the absence of tissue in this part of the image.

DISCUSSION

Fresh fruit bodies of the mushroom *Agaricus bisporus* were vacuum infiltrated with different Gd-DTPA solutions and imaged. The solution filled the extracellular spaces, thereby eliminating susceptibility inhomogeneities.[7,9,11,12] Hence, the resulting relaxation decay after vacuum infiltration originates from both the tissue water and the Gd-DTPA infiltration solution. At fast spin-exchange rates this results in mono-exponential decay, but at lower spin-exchange rates the analytical relation is complex, being nonmono-exponential.[9,14–16]

The discrimination between mono- and nonmono-exponential (multiexponential) behavior in a fit depends strongly on the number of acquired data points and their spacing, the ratio of the decay-constants and -amplitudes and the signal-to-noise ratio. Fast exchange is more likely to occur for T_1 than it is for T_2, because T_2 processes are faster, compared to exchange rates, than T_1 processes.[9,13]

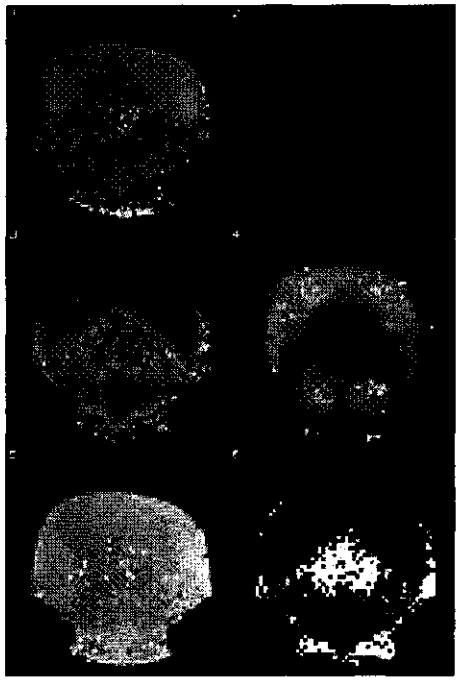

Fig. 5. Amplitude and T_2 images obtained from one and the same mushroom, vacuum infiltrated with 2.5 mM Gd-DTPA solution, applying biexponential fitting of the MSE (T_e = 2.5 ms, T_r = 3 s) dataset. The images 1 and 3 represent the amplitude images of both fractions, image 5 the summation of the amplitude images 1 and 3, all three scaled from 0 to 40,000 a.u. The images 2 and 4 represent the T_2 images of both fractions, image 2 the fraction with a short T_2, and image 4 the fraction with a long T_2, scaled from 0 to 800 ms. Image 6 represents a quotient image of the T_2s of both fractions (image 2/image 4), scaled from 0.05 to 1.0. The fraction with the short T_2 was assigned to the 2.5 mM Gd-DTPA solution, where the fraction with the long T_2 could be assigned to water in the mushroom.

Table 4. Amplitude ± 10% and T_2 ± 10% of two fractions of the bi-exponential fitted MSE image of the mushroom vacuum infiltrated with 2.5 mM Gd-DTPA solution

				Stipe			
		Cap	Gill	Core	Outer	Cutting surface	Center
signal (a.u.)	frac. 1	0.6	±	0.6	±0.5	±	±
	frac. 2	0.3	±	0.3	±0.4	±	±
T_2 (ms)	frac. 1	60	40	40	160	60	80
	frac. 2	500	150	300	450	±	80

± is presented when spreading of the values per pixel in a part of a parameter image does not allow a proper parameter estimation, originating from the images presented in Fig. 5. The amplitude values are scaled to compare to the values presented in Table 5.

The presence of Gd-DTPA decreased T_1 at all Gd-DTPA concentrations but the decrease can not easily be related to the concentration of the Gd-DTPA solution. After vacuum infiltration with the 10 mM infiltrate, the T_1 of the cap and stipe were less reduced as could be expected from the results obtained with the other two Gd-DTPA concentrations. If both fractions would have mixed, the T_1 of the cap and stipe of this mushroom would certainly have been reduced more on vacuum infiltration than was observed now. We, therefore, conclude that the two water pools in the cap and stipe only exchanged on a very slow rate, even at the long T_1 time scale.

The suggestion that the extracellular Gd-DTPA solution and the intracellular water hardly exchange is further supported by the biexponentially fitted MSE images (at T_e = 2.5 ms) of the mushroom infiltrated with 2.5 mM Gd-DTPA solution. Two fractions could be discriminated in parts of that mushroom. The T_2 of fraction 1 of 40–60 ms (for the cap, gill, and core of the stipe) was close to the T_2 expected for the 2.5 mM infiltrate solution (T_2 = 60 ms), as observed below the cutting surface of the stipe (see Tables 1 and 3). This fraction was, therefore, assigned to the Gd-DTPA solution. The T_2 values of fraction 2 observed in the cap, outer stipe, and gill compared rather well to the T_2s observed in the SR-MSE images in the presence of the 10 mM infiltrate. This fraction was therefore assigned to water in mushroom tissue.

In the SR-MSE T_2 images (at T_e = 7.5 ms), two effects counteract; T_2 decreases due to the infiltration with an agent with a short relaxation time and T_2 increases due to loss of susceptibility inhomogeneity. In the applied Gd-DTPA concentration range, T_2 of the infiltrate becomes increasingly difficult to observe at increasing concentrations. For the 10 mM solution, the T_2 of the infiltrate became too short for the applied echo time (T_e) and did not influence the overall decay of the infiltrated tissue anymore. The T_2 images of the mushroom infiltrated with 10 mM Gd-DTPA solution, therefore, reflected the T_2 of water in mushroom tissue without losses due to susceptibility artefacts and without decreases due to infiltration solutions. The resulting T_2 appeared to be equal for the cap and outer stipe, around 300 ms. T_2 of the gill was remarkable shorter, around 100 ms.

Proton-exchange between water in tissue and the protons in the Gd-DTPA solution was for the above mentioned reasons slow at the T_1 and T_2 time scale. Cellular compartmental structures were probably still

Table 5. Mass fractions tissue in vacuum infiltrated mushroom parts (g/g) and amplitude estimations (a.u.) of the various amplitude images

	Tissue fraction (g/g)	0.6 mM (a.u.)		2.5 mM (a.u.)		10.0 mM (a.u.)		Bi-exponential (a.u.)	
		Before	After	Before	After	Before	After	Frac. 1	Frac. 2
Cap	0.6 ± 0.05	0.6	1.0	0.6	0.9	0.6	0.6	0.6	0.3
Gill	—	0.9	1.0	1.0	1.0	0.9	0.9	*	*
Stipe, core	0.4 ± 0.05	0.4	1.0	0.4	0.9	0.5	0.6	0.6	0.3
Stipe, outer	0.8 ± 0.05	0.8	1.0	0.8	1.0	0.8	0.9	±0.5	±0.4

The mass fractions tissue were obtained by weighting excised cap, outer stipe, and core of stipe before and after vacuum infiltration with demineralized water. The presented error is the standard deviation over five individual measurements (n = 5). The amplitude estimations originate from Table 2 and are scaled to 1.0 for the 0.6 mM vacuum infiltrated mushroom for presentational sake. * is presented when spreading of the values per pixel in a part of a amplitude image does not allow a proper parameter estimation.

intact, even after vacuum infiltration.[7,9,11,12,18] This conclusion is supported by the fact that the parameter images of all three infiltrated mushrooms did not change significantly over a period of 2 h. Probably the cellular structures are, therefore, not disturbed and the infiltrate has only entered the extracellular spaces. The cellular membranes only allow relatively slow exchange even at a 2-h time scale.

Let us now try to clearify the origin of the T_2 of the cap and outer stipe (= 300 ms). The vacuole is known to be well developed in the cap and outer stipe[1-3] and can make up 90% of the cellular content in these regions. It are cylindrically shaped compartments with a radius of 10 μm. Using the model of Brownstein and Tarr,[14-16] the observed T_2 ($T_{2,obs}$) depends on the bulk T_2 ($T_{2,bulk}$), the radius of the compartment (A), the diffusion coefficient (D), and the rate of wall relaxation or surface sink strength density[14-19] (H). If $AH<<D$, $T_{2,obs}$ is given by:

$$1/T_{2,obs} = 2H/A + 1/T_{2,bulk} \qquad (3)$$

For vacuolar protons, $T_{2,bulk}$ is in the order of 2 s.[15,18] Under the above-mentioned assumptions of cellular shape, size, and magnetization loss at the wall, an average wall relaxation rate of 1.4×10^{-5} m/s was found. This value is in good agreement with that found by Snaar and Van As[18,19] for apple tissue.

The T_2 of the gill was shorter, probably because gill tissue was not as highly vacuolized as the cap and stipe were, the cells were usually smaller in size[1-3] and the gill was made up from at least three different tissue types; i.e., trama, basidia, and spores.[1] The relaxation mechanisms in the gill are, therefore, much harder to understand compared to those for the other parts of the mushroom and need further investigation.

Now we focus on the interpretation of the amplitude images and to what extent these images present the actual water distribution in mushrooms.

The amplitude images before vacuum infiltration are comparable within the error of 5% to each other. Also the ratio of the mass fractions of the cap, outer stipe, and core of the stipe and the estimated amplitude values before vacuum infiltration correspond remarkably well (Table 5). In earlier work,[10] we demonstrated that amplitude images of mushrooms are hardly affected by susceptibility inhomogeneities, based on the observation that the variation of the echo-time did not affect the reconstructed amplitude images. Therefore, does the amplitude image of these three mushrooms before vacuum infiltration yield an accurate estimation of the water content per pixel of these mushrooms.

The amplitude image of the mushroom infiltrated with 0.6 mM Gd-DTPA represents the maximum amount of water possible per pixel. There was no difference in amplitude of the infiltrating solution below the cutting surface of this mushroom and the amplitude of the mushroom itself. Both T_1 and T_2 were well observable for the 0.6 mM Gd-DTPA solution. The T_2 of the Gd-DTPA solution was close to the T_2 of tissue water. The amplitude difference image of this mushroom, therefore, presents the contribution of the Gd-DTPA solution to the amplitude after vacuum infiltration.

At 10 mM the contribution of the Gd-DTPA solution to the amplitude image was reduced to a minimum, which was expected for the short T_2 of this solution. The amplitude difference image is, indeed, about 5% of the amplitude of the fresh mushroom and originates from the small contribution of the Gd-DTPA solution.

These conclusions for the amplitude images are supported by the biexponential fit of the mushroom infiltrated with 2.5 mM Gd-DTPA. The amplitude image of fraction 2 is an indication for the amount of tissue water in the infiltrated mushroom. This biexponential fit has, however, to be treated carefully because of the poor signal to noise ratio of the decay and the spread in the fitting results in the core and outer regions of the mushroom.

Taking all previous considerations together, we may conclude that the amplitude images reflect the amount of water per pixel best if the T_2 of the tissue water to be observed is sufficiently longer than the applied echo time ($T_2 > 3 * T_e$). The amplitude images are not directly influenced by susceptibility inhomogeneities. The intrinsic T_2 of tissue water is best approached by applying short echo times and long repetition times in a MSE imaging sequence at low field strength.[10] The amplitude images then become the product of the mass percentage water and the tissue density. Together, these two parameters provide the amount of water per pixel with better than 10% accuracy.

CONCLUSIONS

The observed T_2s in the cap and outer stipe of the mushroom originate from tissue water with long relaxation times in relatively large vacuoles. The T_2s of these parts of the mushroom are mainly reduced by susceptibility inhomogeneities and in addition by wall relaxation due to the small radius of the cylindrical-shaped compartment. The rate of wall relaxation in these parts of the mushroom was in good agreement with that found for plant tissues of, for example, apples. The T_2 of gill tissue was shorter because these cells were less vacuolized and smaller in size. Effects

of susceptibility inhomogeneities on the T_2 of gill tissue could hardly be determined.

Proton exchange between the intra- and extra-cellular protons hardly occurred in the vacuum infiltrated mushrooms and cellular structures were, therefore, probably still intact in these mushrooms. The calculated amplitude images were not affected by susceptibility inhomogeneities. These images reflect the water distribution in mushrooms best by applying short echo times in a multiple spin-echo imaging sequence at low magnetic field strength.

The present study demonstrates that NMR imaging is a valuable tool in studying tissue changes upon storage of mushrooms.

Acknowledgments—The authors thank T.J. Schaafsma and L.J.L.D. van Griensven for carefully reading and discussing the manuscript. The project was financially supported by the State Institute for Quality Control of Agricultural Products (RIKILT-DLO) at Wageningen, the Netherlands.

REFERENCES

1. Flegg, P.B.; Spencer, D.M.; Wood, D.A. (Eds.) The biology and technology of the cultivated mushroom. Chichester: John Wiley & Sons; 1985.
2. Craig, G.D. Morphogenesis in Agaricus bisporus. Canterbury: thesis accepted at the Universtity of Kent; 1979.
3. Wood, D.A.; Craig, G.D.; Atkey, P.T.; Newsam, R.J.; Gull, K. Ultrastructural studies on the cultivation process and growth and development of the cultivated mushroom *Agaricus bisporus*. Food Microstruct. 4:143–164; 1985.
4. Jasinski, E.M.; Stemberger, B.; Kilara, A. Ultrastructural studies of raw and processed tissue of the major cultivated mushroom, *Agaricus bisporus*. Food Microstruct. 3:191–196; 1984.
5. Kuchenbrod, E.; Haase, A.; Benkert, R.; Schneider, H.; Zimmermann, U. Quantitative NMR Microscopy on intact plants. Magn. Reson. Imaging 13:447–455; 1995.
6. Duce, S.L.; Carpenter, T.A.; Hall, L.D.; Hills, B.P. An investigation of the origins of contrast in NMR spin echo images of plant tissue. Magn. Reson. Imaging 10:289–297; 1992.
7. Veres, J.S.; Cofer, G.P.; Johnson, G.A. Distinguishing plant tissues with magnetic resonance microscopy. Am. J. Bot. 78:1704–1711; 1991.
8. Belton, P.S.; Ratcliffe, R.G. NMR and compartiment in biological tissues. Prog. NMR Spec. 17:241–279; 1985.
9. Callaghan, P.T. Principles of nuclear magnetic resonance microscopy. Oxford: Clarendon Press; 1991; pp. 414, 416, 38–39, 240–242.
10. Donker, H.C.W.; Van As, H.; Edzes, H.T.; Jans, A.W.H. NMR Imaging of white button mushroom (*Agaricus bisporus*) at various magnetic fields. Magn. Reson. Imaging 14:1205–1215; 1996.
11. Bowtell, R.; Mansfield, P.; Sharp, J.C.; Brown, G.D.; McJury, M.; Glover, P.M. NMR microscopy at 500 MHz: Cellular resolution in biosystems. In: B. Blümich, W. Kuhn (Eds). Magnetic Resonance Microscopy. Weinheim: VCH, 1992: p. 436.
12. Connelly, A.; Lohman, J.A.B.; Loughman, B.C.; Qui-Quampoix, H.; Ratcliffe, R.G. High resolution imaging of plant tissues by NMR. J. Exp. Bot. 38:1713–1723; 1987.
13. Snaar, J.E.M.; Van As, H. A method for simultaneous measurement of NMR spin-lattice and spin-spin relaxation times in compartmentalized systems. J. Magn. Reson. 90:139–148; 1992.
14. Brownstein, K.R.; Tarr, C.E. Spin-lattice relaxation in a system governed by diffusion. J. Magn. Reson. 26:17–24; 1977.
15. Brownstein, K.R.; Tarr, C.E. Importance of classical diffusion in NMR studies of water in biological cells. Phys. Rev. A. 19:2446–2453; 1979.
16. Brownstein, K.R. Diffusion as an explanation of observed NMR behavior of water absorbed on wood. J. Magn. Reson. 40:505–510; 1980.
17. Snaar, J.E.M.; Van As, H. NMR self-diffusion measurements in a bounded system with loss of magnetization at the walls. J. Magn. Reson. A 102:318–326; 1993.
18. Snaar, J.E.M.; Van As, H. Probing water compartments and membrane permeability in plant cells by 1H NMR relaxation measurements. Biophys. J. 63:1654–1658; 1992.
19. Snaar, J.E.M.; Van As, H.; Hills, B.P. Nuclear spin relaxation and diffusive exchange in multi-compartment systems. J. Magn. Reson. A. (submitted).

5

CELL WATER BALANCE OF WHITE BUTTON MUSHROOMS (*AGARICUS BISPORUS*) DURING ITS POST-HARVEST LIFETIME STUDIED BY QUANTITATIVE MAGNETIC RESONANCE IMAGING.

published as:

Donker, H.C.W. & Van As, H.; Cell water balance of white button mushrooms (*Agaricus bisporus*) during its post-harvest lifetime studied by quantitative magnetic resonance imaging; Biochim. Biophys. Acta gen. sub. (1999); 1427: 287-297.

ELSEVIER

Biochimica et Biophysica Acta 1427 (1999) 287–297

BBA

Cell water balance of white button mushrooms (*Agaricus bisporus*) during its post-harvest lifetime studied by quantitative magnetic resonance imaging

H.C.W. Donker, H. Van As *

Department of Biomolecular Sciences, Laboratory of Molecular Physics, Wageningen University, Dreijenlaan 3, 6703 HA Wageningen, The Netherlands

Received 20 July 1998; received in revised form 3 February 1999; accepted 11 February 1999

Abstract

A combination of quantitative water density and T_2 MRI and changes therein observed after infiltration with 'invisible' Gd-DTPA solution was used to study cell water balances, cell water potentials and cell integrity. This method was applied to reveal the evolution and mechanism of redistribution of water in harvested mushrooms. Even when mushrooms did not lose water during the storage period, a redistribution of water was observed from stipe to cap and gills. When the storage condition resulted in a net loss of water, the stipe lost more water than the cap. The water density in the gill increased, probably due to development of spores. Deterioration effects (i.e. leakage of cells, decrease in osmotic water potential) were found in the outer stipe. They were not found in the cap, even at prolonged storage at 293 K and R.H. = 70%. The changes in osmotic potential were partly accounted for by changes in the mannitol concentration. Changes in membrane permeability were also indicated. Cells in the cap had a constant low membrane (water) permeability. They developed a decreasing osmotic potential (more negative), whereas the osmotic potential in the outer stipe increased, together with the permeability of cells.

Keywords: *Agaricus bisporus*; Nuclear magnetic resonance imaging; Cell-water balance; Cell-water potential; Post-harvest lifetime; Senescence

1. Introduction

The mushroom (*Agaricus bisporus*) is known for its fast degradation after harvest and its coinciding reduction of economical value. To reduce economic loss, control of pre-sale storage is important. Especially the water balance of the mushroom is known to be severely affected by internal and external influences [1].

Mushrooms consist for about 92% (mass/mass) of water (90% for the gill and 92–95% for the cap and stipe) and are built up from aggregated mycelium threads. The aggregated mycelium is loosely packed and has a spongy structure with a varying density around 0.6 g/ml [1–4]. The high surface to volume ratio creates a large surface for water evaporation [1–5]. Due to the mushroom morphology

* Corresponding author. Fax: +31 (317) 482725; E-mail: henk.vanas@water.mf.wau.nl

and post-harvest storage conditions, changes in the water distribution over the mushroom occur after harvest. On harvest, the mushroom continues its natural development [1]: further development of gill and concomitant maturation of basidiospores, stipe elongation, opening of the cap, release of basidiospores.

These processes result from the combined effects of genetically programmed cell growth and cell death [6–8] especially in the cap and gill. The resources for these post-harvest processes have to be provided by the harvested mushroom itself. Water, as the major cell constituent, is redistributed internally, from the stipe to the cap and gill. The evolution and mechanism of redistribution of water in senescing mushrooms are still subject of scientific discussion. Numerous mechanisms have been proposed, such as diffusion, cytoplasmic streaming, osmotically driven flow, transpiration and bulk flow [1]. Obviously, the redistribution of water is influenced by the external climatic conditions [9–16].

On the other hand, however, harvested mushrooms break down proteolytically [12,13,16,17] and dry weight is relocated from the stipe to the cap and gill [18]. Since dry weight relocates, cellular structures are likely to be affected and water redistributed. Different deteriorating processes were found to be active in harvested mushrooms compared to not harvested, naturally senescing mushrooms [8]. These authors observed enlarged interhyphal spaces, loss of extracellular matrix and empty, exhausted and abnormally swollen cells in harvested mushrooms.

Proven earlier [19], nuclear magnetic resonance imaging (MRI) can be used to measure quantitatively the water distribution in individual mushrooms. The origin of the observed MRI contrast was elucidated by Gd-DTPA infiltration experiment [20]. Especially T_2 appeared to be heavily influenced by susceptibility inhomogeneities caused by the spongy structure of the mushroom. The water content per pixel could be measured quantitatively under strict imaging conditions.

Here experiments on harvested mushrooms are presented, demonstrating how quantitative MRI can provide information to trace changing water distributions throughout the post-harvest lifetime and its underlying mechanism(s).

2. Materials and methods

2.1. Mushrooms

Fresh mushrooms were obtained from either a local greengrocer or a mushroom grower. One lot of mushrooms (0.5 kg) from a greengrocer (likely to be Horst-U1) was divided into batches A, B and C, around 24 to 48 h after harvest. The experiments on batches A, B and C started the same day.

Another lot of mushrooms Horst-U1 (first flush, 1 kg), directly obtained from a mushroom grower, was separated into three batches, D, E and F, less than 4 h after harvest. The experiments on batches D, E and F started 24–36 h after harvest of these mushrooms. Day 1 for all six batches therefore refers to a period of around 24–36 h after harvest.

2.2. Storage

Each batch was stored differently in plastic packages as indicated in Table 1. Batches A, B and C were stored over 7 days. The three other batches were stored over 4 days. The closed plastic packages did not allow any gaseous exchange with the environment. From each batch one randomly selected mushroom was followed in time by imaging it each day while the experiment lasted, to trace changes in the water distribution throughout an entire storage period. Simultaneously the fresh weight of each mushroom was recorded and compared to the fresh weight at the start of the experiment. This experiment will be referred to as the 'storage experiment'.

Furthermore, one mushroom was randomly selected from batches D, E and F each day and imaged before and after vacuum infiltration with a 25.0 mM Gd-DTPA solution (T_2 is about 6 ms [19]). This solution was prepared from a 0.5 M Gd-DTPA stock solution with a twofold excess of DTPA (Schering, Berlin, Germany). Vacuum infiltration took place at 20 mmHg pressure for 10 min in a vacuum exsiccator. Before releasing the vacuum, remaining air bubbles were removed from the solution and from the surface of the fruit body by gently shaking and tapping of the exsiccator. This experiment will be referred to as the 'vacuum infiltration experiment'.

The fresh weight of the mushrooms in the storage experiment was determined each day before image

Table 1
Mass changes in mushrooms A, B, C, D, E and F

Batch	Storage regime			Mass fraction days after harvest						
	T (K)	R.H. (%)	Package	1	2	3	4	5	6	7
A	278	>95%	closed	1.00	1.00	1.00	1.00	0.99	0.99	0.99
B	278	<95%	open	1.00	0.99	0.98	0.96	0.95	0.94	0.93
C	293	60%	open	1.00	0.98	0.92	0.81	0.70	0.65	0.53
D	278	>95%	closed	1.00	1.00	1.00	1.00			
E	293	>95%	closed	1.00	1.00	1.00	1.00			
F	293	70%	open	1.00	0.99	0.98	0.97			

The mass changes are expressed as fractional fresh weight at the various days of the storage experiments compared to the fresh weight at day 1 (fresh weight (day n)/fresh weight (day 1)).

acquisition. The fresh weights of the mushrooms in the vacuum infiltration experiment were determined before acquisition of the 'before infiltration' image. The weights after vacuum infiltration were also determined.

First, mushrooms of the storage experiment were imaged and, second, one mushroom from batches D, E and F was imaged before and after infiltration. The vacuum infiltrated mushrooms were imaged as fast as possible after vacuum infiltration, typically 10 min.

Separately, three mushrooms from batches D, E and F were divided into cap stipe and gill, weighed and dried to determine dry weight changes, each day while the storage period lasted.

2.3. *Magnetic resonance imaging*

The mushrooms were imaged on a 0.47 T (20.35 MHz) imager [19,20]. The pulse sequence was described earlier and applied with a pre-acquisition delay of 4.9 ms for batches A, B and C and 1 ms for batches D, E and F (Fig. 1) [19,20].

The images of batches A, B and C were acquired with a spectral width 100 kHz, 64 complex data points per transient, 64 phase-encoding gradient steps, 512 echoes, no phase cycling and no averaging. The data were filtered with a gaussian filter of 0.75 pixel (or 330 Hz per point) and zero filled once before fast Fourier transformation and phasing.

Typical applied acquisition parameters for batches D, E and F were: spectral width 100 kHz, 128 complex data points per transient, 128 phase-encoding gradient steps, two acquisitions with alternating phases per transient, 128 echoes, no zero-filling and direct fast Fourier transformation.

Batches A, B and C were imaged with $T_e = 2.5$ ms; batches D, E and F with $T_e = 7.0$ ms. All six batches had $T_r = 3$ s ($T_r \gg T_1$), field of view 3 cm and a slice thickness of 2 mm.

The real intensity images of batches A, B and C and the absolute intensity images of batches D, E and F (with subtraction of the baseline level) were fitted on a pixel by pixel basis with a mono-exponential decay function without baseline resulting in an amplitude and T_2 image [19,20]. The imaginary images of batches A, B and C comprised a negligible signal. The Levenberg-Marquart algorithm [21] was used for chi-square minimisation. Pixels with signal intensity less than 5% of the maximum signal intensity in the first echo were rejected for fitting.

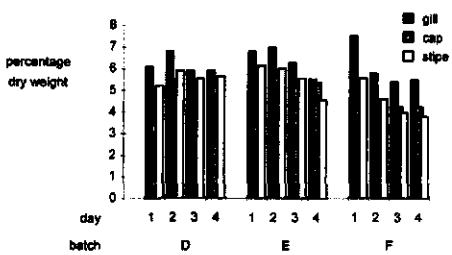

Fig. 1. Percentages dry weight (±5%) of the various tissues of mushrooms from batches D, E and F at the various days of the experiments. The percentages dry weight are determined by weighing separated fresh tissues from three mushrooms before and after overnight drying at 353 K.

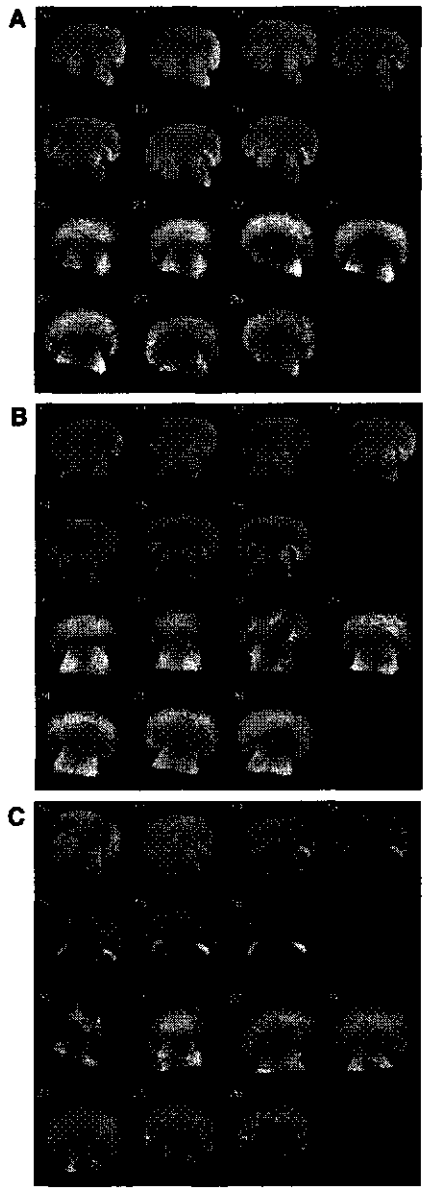

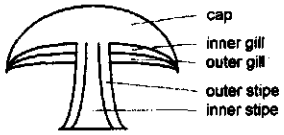

Fig. 3. Various tissue types in mushrooms that could be discriminated on the basis of the MRI results.

2.4. Data analyses

The resulting parameter images were further analysed by calculating 95% confidentiality intervals, representing the mean ± 1.96 times the standard error, out of pixel ensembles of around half of all pixels representing one tissue type in a mushroom, assuming a normal distribution of the pixel's T_2 and amplitude values. The pixel ensembles, representing particular tissues, were automatically selected from the image with a correlation calculation on the amplitude, T_2, reciprocal T_2 and distance between one randomly selected pixel and all other pixels in an image. A pixel was said to belong to a pixel ensemble of a particular tissue type if the correlation coefficient for the aforementioned parameters exceeded 0.95. The amplitude images were scaled to 100% water content per pixel by use of a reference capillary with $T_2 = 47$ ms, measured in combination with all measurements of batches D, E and F.

3. Results

3.1. Weight

The developments of the fresh weights of the mushrooms, subjected to the storage experiment, are presented in Table 1. The loss of fresh weight strongly depended on the applied storage regime. Mushroom C lost more fresh weight than all other mushrooms. The mushrooms from batches D, E and

←

Fig. 2. Typical example of images of T_2 (0–400 ms) and percentages of water (0–100% water) of mushrooms from batches A (panel A), B (panel B) and C (panel C). Images 10–16 represent the water percentage images from day 1 to day 7 and images 20–26 present the corresponding T_2 images.

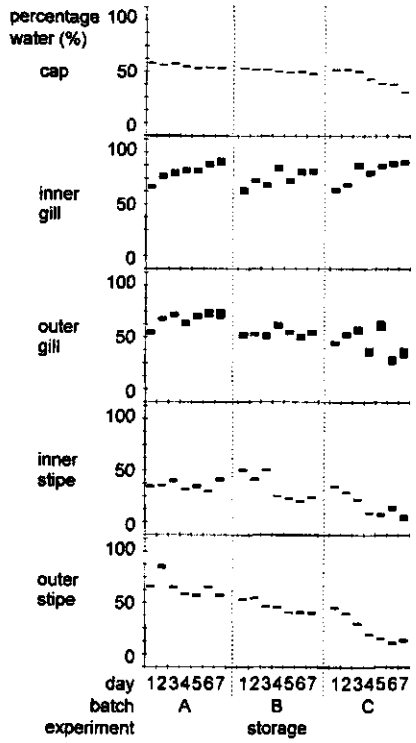

Fig. 4. 95% confidence intervals of the percentages of water per pixel in the various parts of the mushrooms of batches A, B and C, in a storage experiment.

F did hardly lose any fresh weight over the 4 day period.

The distribution of the dry weight after harvest was determined from a representative sample of batches D, E and F, while the experiment lasted (Fig. 1). Raising storage temperature and reducing R.H. induced a reduction of dry weight of the stipe and the cap, where the decrease in the stipe was faster. The dry weight of the gill was in all cases higher than those of the cap or stipe.

3.2. Single parameter images

Fig. 2 presents amplitude and T_2 images of three typical examples of storage experiments A, B and C over 7 consecutive days during storage. Pixel selection and averaging resulted in the discrimination of five different tissue types, as presented in Fig. 3. The averages are based on 1000–2500 pixels for the cap, 100–850 for the inner stipe, 500–1600 for the outer stipe, 20–300 for the inner and outer gills and 18 for the reference tubes. The 95% confidence intervals of the amplitude (percentage of water) of these different tissue types in all mushrooms for both storage experiments and T_2 values of the first storage experiment ($T_e = 2.5$ ms) are presented in Figs. 4–6. When two of these intervals do not overlap, their mean values are said to differ significantly. The T_2 values

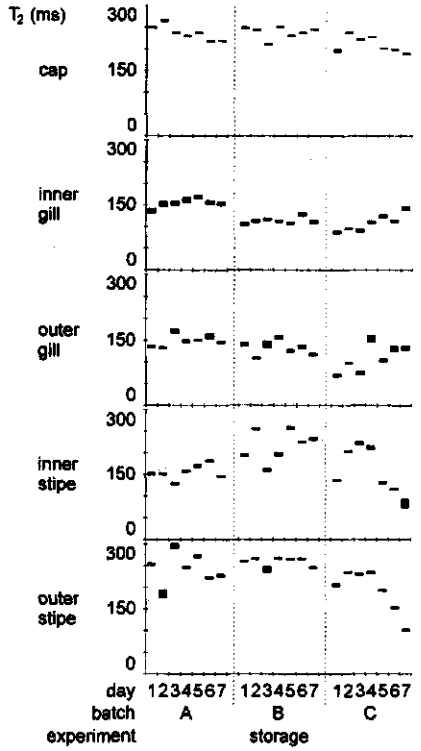

Fig. 5. 95% confidence intervals of T_2 (ms) in the various parts of the mushrooms of batches A, B and C, in a storage experiment ($T_e = 2.5$ ms).

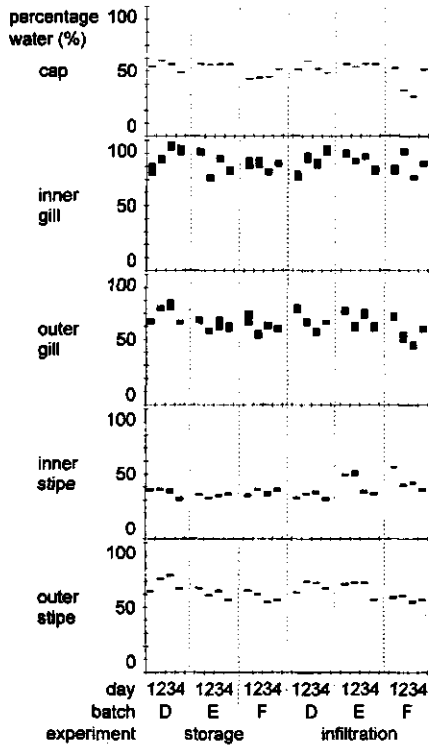

Fig. 6. 95% confidence intervals of the percentages of water per pixel in the various parts of the mushrooms of batches D, E and F, in a storage experiment and before vacuum infiltration.

at $T_e = 7$ ms (data not shown) were lower than these observed at $T_e = 2.5$ ms, in agreement with previous results [19,20]. T_2 ($T_e = 7$ ms) values were about constant in time except for the outer stipe (decrease from about 150 ms to 100 ms for batches E and F) and the inner gill (increase from about 150 ms to over 200 ms for batches E and F). From Fig. 6 (and the corresponding T_2 values, data not shown) it is clear that the results of a single mushroom followed in time (D, E, F, storage) and that of different individual mushrooms picked out of a batch as a function of storage time (D, E, F, before infiltration) are identical.

Figs. 4 and 6 reveal a redistribution of water in the harvested mushrooms from stipe and cap to gill, even when no net loss of water was detected (batch A, cf. Table 1). The decrease in the stipe was more pronounced than in the cap.

3.3. *Vacuum infiltration*

The changes on vacuum infiltration in the different tissue types were easiest observed in graphs presenting the difference values, Δ% water (Fig. 7A) and ΔT_2 (Fig. 7B). These figures present the difference values compared to the width of the summed 95% confidence intervals (both positively and negatively) of the values after minus before vacuum infiltration. When the Δ-values are larger than the summed 95% confidence intervals, the changes are said to be significant.

3.3.1. *Water percentage differences*

Water percentages in the cap of batch F increased on vacuum infiltration despite its dry storage condition at 293 K and R.H. = 70%. Batches D and E did not show storage related changes of the water percentages in the cap on vacuum infiltration (with the exception of E at day 4).

The water percentage of the inner and outer stipe did, however, present storage-dependent behaviour. The initial increase in the inner stipe of batch D disappeared in batch F. The outer stipe developed a clear reduction going from batch D to F.

3.3.2. *T_2 differences*

T_2 of the cap increased significantly on vacuum

Fig. 7. (A) Δ% water in the various tissues of the mushrooms of batches D, E and F (after vacuum infiltration minus before vacuum infiltration). The black bars represent the difference between the mean values of the pixel ensembles and the grey bars represent the summed 95% confidence intervals of the mean values, presented both positive and negative. (B) ΔT_2 (ms) in the various tissues of the mushrooms of batches D, E and F (after vacuum infiltration minus before vacuum infiltration). The black bars represent the difference between the mean values of the pixel ensembles and the grey bars represent the summed 95% confidence intervals of the mean values, presented both positive and negative.

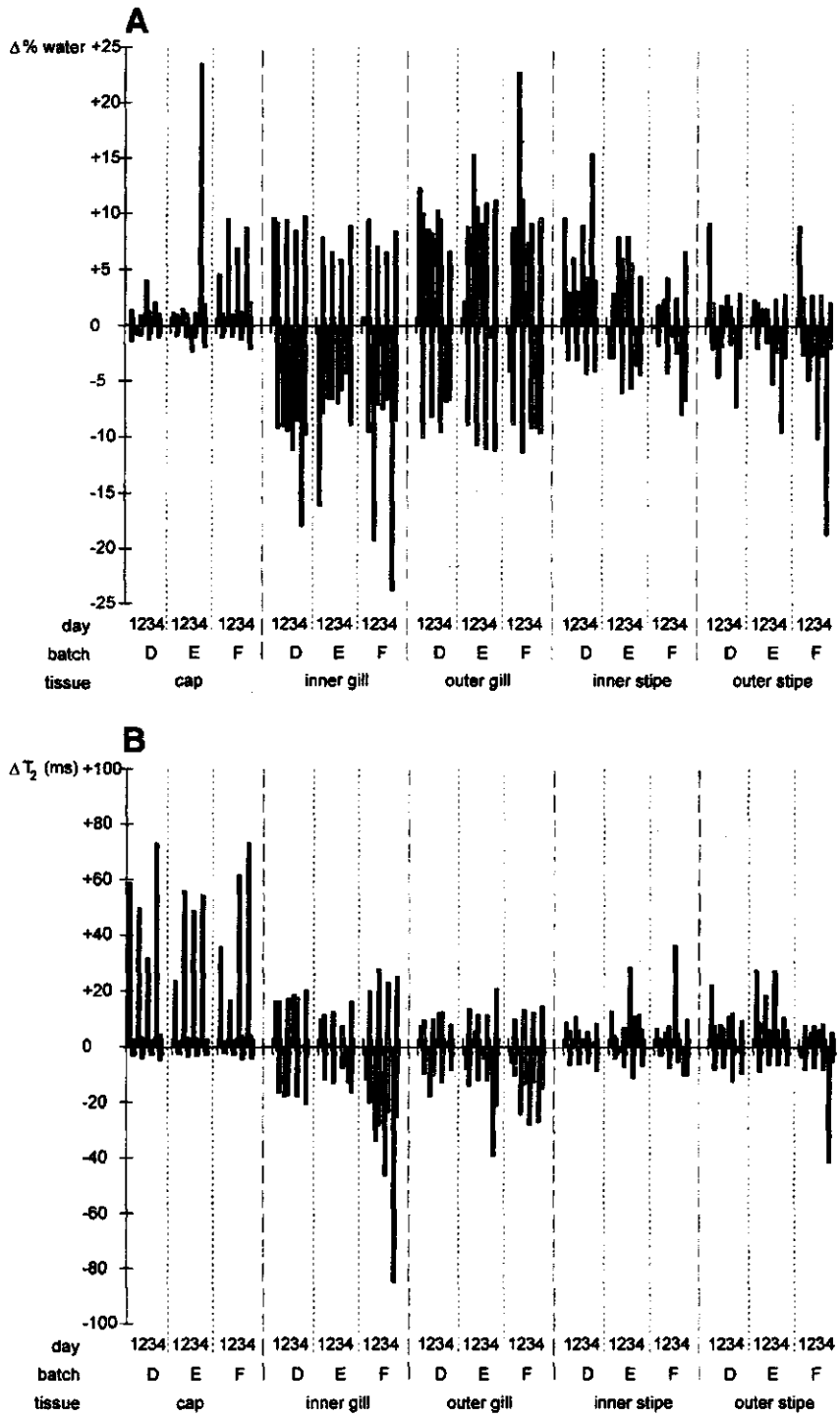
A
Δ% water +25
+20
+15
+10
+5
0
-5
-10
-15
-20
-25
day 1234 1234 1234 1234 1234 1234 1234 1234 1234 1234 1234 1234 1234 1234 1234
batch D E F D E F D E F D E F D E F
tissue cap inner gill outer gill inner stipe outer stipe
B
Δ T2 (ms) +100
+80
+60
+40
+20
0
-20
-40
-60
-80
-100
day 1234 1234 1234 1234 1234 1234 1234 1234 1234 1234 1234 1234 1234 1234 1234
batch D E F D E F D E F D E F D E F
tissue cap inner gill outer gill inner stipe outer stipe

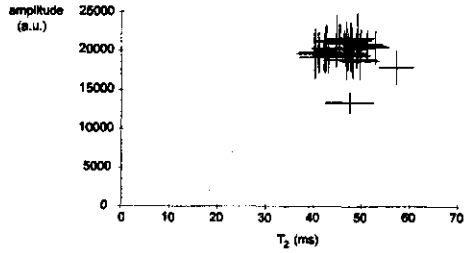

Fig. 8. Mean T_2 values versus mean amplitudes of the external reference capillaries in the storage and vacuum infiltration experiments of batches D, E and F. The lengths of the bars indicate twice the length of the standard deviation of the mean values. Overall, the means are based on 18 pixels ($n = 18$) for 33 measurements.

infiltration, although a trend was not clear. The inner gill developed a significant reduction of T_2 on vacuum infiltration towards batch F. A reduction of T_2 was also observed in the outer gill, though not as manifest as in the inner gill. The inner stipe showed two cases of increased T_2 on vacuum infiltration (batch E, day 3 and batch F, day 3) which could not be related to a storage regime. The outer stipe had an increased T_2 for batch E. T_2 of the outer stipe at day 4 of batch F decreased by 40 ms.

3.4. Data significance

The variability within the homogeneous reference capillary (filled with a doped aqueous solution and containing about 18 pixels) and the between-experiment variability for this capillary for all measurements of batches D, E and F (Fig. 8, $n = 33$) were comparable and resulted in a standard deviation of about 10% and a standard error of 2.5% for both parameters. Since we have normalised the amplitude images of the mushrooms on the reference tube, these images have an even better accuracy. For the T_2 images this normalisation procedure cannot be applied. However, the amplitude and T_2 values presented in Figs. 4–8 are based on the described selection procedure. They are the average of a structurally larger number of pixels than for the reference tube values. This makes the standard error for the tissue values smaller than the standard error for the reference tube values ($< 2.5\%$).

4. Discussion

NMR imaging has often been used to study internal anatomy in crops, fruits and other agricultural products [22]. Here we applied quantitative single parameter (amplitude and T_2) NMR imaging [19,20] to study post-harvest deterioration in stored mushrooms. The images were obtained at two different T_e values. The resulting T_2 images of mushrooms are strongly T_e dependent due to susceptibility inhomogeneities [19]. At $T_e = 2.5$ ms these artefacts are minimal. The T_2 values at $T_e = 2.5$ ms at day 1 (Fig. 5) compare well to those reported earlier [20]. It has been demonstrated that amplitude images are independent of T_e at the T_e values used [19]. They represent directly the tissue density times water content. Tissue densities of freshly harvested mushrooms were reported earlier [20]: cap 0.6 ± 0.05, inner stipe 0.4 ± 0.05, outer stipe 0.8 ± 0.05. When the amplitudes in this study at day 1 are combined with the percentages dry weight (Fig. 1) they show these tissue densities within the error boundaries.

All T_2 and amplitude values are expressed as 95% confidence intervals. If two intervals do not overlap, their difference is significant. The between-mushroom variations on day 1 reflect the variation in tissue density times water content for the amplitude values and variation in cell size and geometry for the T_2 images, as was found earlier [20].

The amplitude images clearly revealed a redistribution of water in harvested mushrooms, even in mushrooms that did not lose water at all (cf. Table 1 and Fig. 2). This redistribution occurred from the stipe and the cap to the gills and its velocity was storage condition dependent. However, the amplitude images comprise no information about the underlying mechanisms.

Harvested mushrooms break down proteins [12,13,16–18] especially in the stipe but also in the cap. On top of that, they relocate and/or respire e.g. mannitol, the most abundant metabolite in freshly harvested mushrooms [23]. Consequently, the water-binding capacity might decrease, followed by loss of cellular integrity. In general, we therefore expect changes in the cell water potentials in the different tissue types followed by water redistribution. T_2 relaxation times contain information related to these processes [20,22]. However, a number of different,

partly counteracting, mechanisms contribute to the observed changes in the T_2 values of the different tissues. T_2 alone does not allow to discriminate between them uniquely. Below we argue that they can be discriminated by a combination of T_2, Δamplitude and ΔT_2 information. The Gd-DTPA infiltration experiments provide this information.

In freshly harvested mushrooms, vacuum infiltration with a concentrated Gd-DTPA solution (> 10 mM) measured at relatively long T_e (7.5 ms) resulted in about identical amplitude values, but in longer T_2 values for the cap and (inner) stipe [20]. These results were explained in the way that the extracellular Gd-DTPA solution removed susceptibility artefacts and that (intra)cellular water did hardly exchange with the extracellular Gd-DTPA solution [20]. Thus, elimination of susceptibility inhomogeneities by vacuum infiltration leads to increased T_2 values and constant amplitudes in fresh tissue (cf. day 1 in Fig. 7).

In contrast, increasing (less negative) cell water potentials will result in decreasing amplitudes on infiltration due to loss of water from the intracellular to the extracellular space. Decreasing water potentials will result in the opposite effect: water uptake by the cell. Loss of cell integrity in deteriorating tissue will result in reduced T_2 values, eventually accompanied by a decrease in amplitude due to an increased exchange between intracellular water and the extracellular infiltrate. In the extreme of fast exchange, the high Gd-DTPA concentration of the extracellular infiltrate will reduce T_2 of the intracellular water. At the same time, amplitudes (from the remaining intracellular water) will decrease. Since tissue densities of the cap and stipe are around 0.5, half of the pixel volume is filled with (intra)cellular water and the other half is filled with (extracellular) 25 mM Gd-DTPA solution. The overall Gd-DTPA concentration can therefore not drop below 10 mM. Such a solution has a T_2 of about 15 ms, which is still hardly observable in the experiments with $T_e = 7$ ms, as they are presented here [19].

In the outer stipe of the mushrooms from batches E and F a decrease was observed on prolonged storage in the amplitude and T_2 and a change from an increase to a decrease in Δamplitude and ΔT_2 (cf. Figs. 6 and 7A,B). The initial increase in ΔT_2 results from the elimination of susceptibility effects. The decrease in T_2 and amplitude coincides with the redistribution of dry weight from the stipe to the cap and gill (Fig. 1). Whereas the stipe initially has a higher percentage dry weight compared to the cap, the dry weight level is reduced to levels below the dry weight of the cap. Although the differences are not large, they are important with respect to the cell water potential/osmotic potential. Tissue with a decreasing dry weight has an increasing (less negative) osmotic potential. This tissue starts losing water in an environment with a lower osmotic potential. Mannitol concentrations in the stipe drop from around 100 mM (1.8% fresh weight) to concentrations below 10 mM (0.2% fresh weight [23]) and Gd-DTPA is infiltrated at concentrations of 25 mM in around 40–60% of the tissue volume. For these reasons, water is likely to be extracted out of the (deteriorating) stipe cells. The decrease in Δamplitude on prolonged storage demonstrates this effect for the stipe. The decrease in ΔT_2 indicates an increase in cell permeability/loss of cell integrity.

In the cap, ΔT_2 increments on vacuum infiltration are observed, even at prolonged storage. They are caused by the eliminated susceptibility influences [20]. At the same time, a Δamplitude increase is observed in mushrooms of batch F and on the last day of batch E. Amplitudes can only increase on vacuum infiltration when the osmotic potential becomes much lower compared to the infiltration solution and the cell integrity is not affected.

Taking these observations together, it can be stated that on storage the cell permeability/cell integrity in the stipe is affected. This results in a higher exchange between residual cellular water and infiltrate. These parameters are definitively less affected in the cap. Therefore, the cell water potential decreased in the cap and increased in the stipe. This coincides with the redistribution of dry weight from the stipe to the cap and the conclusions found earlier that the gill and cap are preferentially provided with proteolytic breakdown products, in favour of the stipe [12,13,16,17,23].

Conclusions about the inner and outer gills and the inner stipe are harder to draw because the 95% confidence intervals for these tissues are much larger than for the outer stipe and cap. Gill tissue consists of vital cells, which are assumed to divide during development and post-harvest lifetime [24]. The observed decrease in ΔT_2 and Δamplitude in the inner

gill, especially in batch F, therefore cannot indicate a decrease in cell integrity, but might indicate increased cell permeability. This behaviour also prevents to draw conclusions about the development of the cell water potential in the gill tissue. On top of that mannitol concentrations and Gd-DTPA concentrations in the gill cannot be discussed as in the cap and stipe since the tissue density in the gill is much higher (90–100%) and the amount of infiltrated Gd-DTPA much lower.

It is interesting to compare our (T_2) findings with the morphometric results described by Braaksma et al. [24]. These authors found tissue specific processes during post-harvest development, such as cell growth by vacuolar expansion in cap tissue while most of the cells (about 80%) in this tissue disappear. This growth was not observed in the T_2 values of the cap (Fig. 5), probably due to a counteracting effect of susceptibility artefacts and membrane water permeability on T_2. In the gill tissue, radial expansion of both vacuole and cytoplasm was observed [24], which can explain the tendency of an increasing T_2 value in the gills, especially in the inner gill where susceptibility effects are minimal (cf. Fig. 5). The initial increase in T_2 values observed in the stipe also indicates cell growth. The decrease at longer storage times, again, indicates increased susceptibility effects, in accordance with the reported increase in intercellular space and cell death in the stipe [24].

Further work will be required to elucidate microscopic cellular deterioration and the function of other osmotic compounds like (poly)phosphate [25] in relation to macroscopic changes of deteriorating harvested *mushrooms*.

Extending our method, it might be possible to measure non-invasively and non-destructively the water potential by use of infiltrates containing both Gd-DTPA and an osmoticum that does not enter the cells (e.g. PEG-6000 or mannitol). For intact systems like fruits or plants (leaves) the changes in water potential may be quantified with respect to the water potential of the infiltrate. For e.g. seeds, pollen and tissue cultures the water potential of these systems can be monitored by observing de- or rehydration effects and changes in T_2 of these systems as a function of external osmotic potential of the medium. By use of imaging this can be performed with a range of different osmotic potentials in one stroke.

5. Conclusions

This study demonstrates how MRI can be used to trace changes in cell water balance, cell water potential and cell water permeability/cell integrity by the use of single parameter MSE-MRI and vacuum infiltration with a Gd-DTPA solution.

Storage experiments on mushrooms revealed the quantitative water redistribution by amplitude images. Infiltration experiments appended the underlying mechanisms by combined amplitude and T_2 information. T_2 information alone could not be correlated to morphometric results one on one. In addition to cell size and geometry, effects of changes in susceptibility and membrane permeability also contribute to the observed T_2 values.

The method is expected to be applicable to other biological systems, in which intracellular water does not exhibit fast mass transfer with the extracellular space.

Acknowledgements

The authors thank D. van Dusschoten for the tedious MR hard- and software optimisation and T.J. Schaafsma and L.J.L.D. Van Griensven for carefully reading and discussing the manuscript. The project was financially supported by the State Institute for Quality Control of Agricultural Products (RIKILT-DLO) at Wageningen, The Netherlands.

References

[1] P.B. Flegg, in: P.B. Flegg, D.M. Spencer, D.A. Wood (Eds.), The Biology and Technology of the Cultivated Mushroom, John Wiley and Sons, Chichester, 1985.

[2] D.A. Wood, G.D. Craig, P.T. Atkey, R.J. Newsam, K. Gull, Food Microstruct. 4 (1985) 143–164.

[3] P.T. Atkey, Mushroom J. 129 (1983) 241–244.

[4] P.T. Atkey, R. Nichols, Mushroom J. 129 (1983) 334–335.

[5] E.M. Jasinski, B. Stemberger, A. Kilara, Food Microstruct. 3 (1984) 191–196.

[6] M.H. Umar, L.J.L.D. Van Griensven, Mycologia 89 (1997) 274–277.

[7] M.H. Umar, L.J.L.D. Van Griensven, Mycol. Res. 101 (1997) 1025–1032.

[8] M.H. Umar, L.J.L.D. Van Griensven, Mycol. Res. 101 (1997) 1409–1422.

[9] J. Czapski, J. Bakowski, Acta Agrobot. 39 (1986) 221–234.
[10] R.B. Beelman, A. Okereke, B. Guthrie, in: Proc. Int. Symp. Scientific and Technical Aspects of Cultivating Edible Fungi, Pensylvenia State Univ., University Park, PA, 1986, pp. 251–258.
[11] R. Beelman, Mushroom J. 182 (1988) 455–463.
[12] D.P. Murr, L.L. Morris, J. Am. Soc. Hortic. Sci. 100 (1975) 16–19.
[13] D.P. Murr, L.L. Morris, J. Am. Soc. Hortic. Sci. 100 (1975) 298–301.
[14] C. MacCanna, T.R. Gormley, Mushroom Sci. 1968 (1968) 485–492.
[15] J.B.W. Hammond, R. Nichols, J. Sci. Food Agric. 26 (1975) 835–842.
[16] J.B.W. Hammond, Phytochemistry 18 (1979) 415–418.
[17] K.S. Burton, M.D. Partis, D.A. Wood, C.F. Thurston, Mycol. Res. 101 (1997) 146–152.
[18] A. Braaksma, D.J. Schaap, T. de Vrije, W.M.F. Jongen, E.J. Woltering, Postharvest Biol. Technol. 4 (1994) 99–110.
[19] H.C.W. Donker, H. Van As, H.T. Edzes, A.W.H. Jans, Magn. Reson. Imaging 14 (1996) 1205–1215.
[20] H.C.W. Donker, H. Van As, H.J. Snijder, H.T. Edzes, Magn. Reson. Imaging 15 (1997) 113–121.
[21] W.H. Press, in: W.H. Press, S.A. Teukolsky, W.T.Vetterling, B.P.Flannery (Eds.), Numerical Recipes in C, 2nd edn., University Press Cambridge, Cambridge, 1992.
[22] J.S. MacFall, H. Van As, in: Y. Shachar-Hill, P.E. Pfeffer (Eds.), Nuclear Magnetic Resonance in Plant Biology, American Society of Plant Physiologists, Rockville, MD, 1996.
[23] H.C.W. Donker, A. Braaksma, Postharvest Biol. Technol. 10 (1997) 127–134.
[24] A. Braaksma, A.A. van Doorn, H. Kieft, A.C. van Aelst, Postharvest Biol. Technol. 13 (1998) 71–79.
[25] A. Braaksma, P. van der Meer, D.J. Schaap, Postharvest Biol. Technol. 8 (1996) 121–127.

6

CONCLUSIONS AND SUGGESTIONS FOR FUTURE RESEARCH

6.1 Conclusions

After harvest the mushroom opens its cap, stretches its stipe and sheds spores. This is natural behaviour of the mushroom, even in the absence of an exogenous substrate (1). The opening of the cap and stretching of the stipe are accompanied by a redistribution of water and osmotica, because the mushroom stretches cells at specific locations. On the other hand, metabolic resources are required to keep the respirative rate high, especially in the gill.

In Chapter 2 (2), changes in the metabolic levels of mannitol, glutamate, glutamine, alanine, aspartate, fumarate and malate were found to be tissue-specific. Mannitol was relocated from the stipe to the gill and used as a respiratory substrate there. Proteolytic breakdown was apparent, preferentially in the stipe.

Water has a sink-source relation with mannitol because of the high amounts of mannitol present in mushrooms. Locations with high mannitol levels attracted water from locations with lower mannitol levels (cf. Chapter 2). If the mushroom can control its mannitol levels, it hereby obtains a mechanism to control the water distribution over the fruitbody and e.g. attracts water to locations where cells stretch.

In Chapter 3 (3), the influence of the magnetic field strength on MRI images of mushrooms was studied to come to quantitative proton density and T_2 images. Image contrast was found to be influenced by susceptibility inhomogeneities. Imaging of mushrooms could best be done at low magnetic field strength and short echo-times applying a multi-spin-echo imaging pulse sequence.

In Chapter 4 (4), the observed T_2 values of mushroom tissue appeared to be influenced by size and geometry of the hyphae. The amplitude images were not directly influenced by the earlier found susceptibility inhomogeneities where the T_2 images were influenced. Under optimal imaging conditions for mushrooms, the amplitude images directly reflect the water distribution in mushrooms.

Chapter 5 (5) describes the application of quantitative amplitude images for the study of changes in cell water balance, cell water potential and cell water permeability / cell integrity in mushrooms. Storage experiments reveal the redistribution of water from the stipe to the cap and gill and the loss of cellular integrity in the stipe. This coincides with the proteolytic breakdown of the stipe in favour of the cap and gill found in Chapter 2 (2) and the redistribution of dry weight from the stipe to the cap in Chapter 5 (5).

6.2 Unsuccessful and preliminary experiments

Various other experiments were conducted in the context of this Thesis, which did not lead to public presentations:

- ^{31}P spectroscopy on intact tissue,
- CPMG T_2 ^1H decay experiments by various short echo times combined with ^{13}C spectroscopy of intact tissue pieces at 9.4 T,
- ^1H MRI of water uptake in fresh and partially dried mushrooms.

The ^{31}P spectroscopy experiments suffered from extensive influence of susceptibility inhomogeneities. This resulted in spectra with extremely broadened resonances, which could not be identified.

The various experiments on excised tissue suffered from uncontrollable tissue degradation. Especially gill tissue could not be excised without extensive damaging the tissue ultrastructure. This inhibited spectroscopy experiments on excised tissue.

The CPMG experiments at 9.4 T resulted in fast amounts of data. The decay curves were analysed with various discrete and continuous multi-exponential fitting algorithms but the resultive T_2 distributions could not be interpreted in terms of a physiological meaningful model. The distributions appeared to depend heavily on minor changes in T_e and/or accidentally uncontrolled experimental influences. In addition, a thorough study of the behaviour of the applied fitting algorithms did not lead to a further understanding of the observed T_2 distributions. Since the analysis of decay curves of phantoms with known T_2's resulted in completely predictable T_2 distributions.

Figure 1 presents the results of a preliminary experiment, to map transport pathways for ion transport by a series of rapid spin echo images of two mushrooms placed in a contrast medium. The oldest, drier mushroom absorbs the solution uniformly whereas the fresh mushroom directs the solution to two specific locations in the gill. These two locations might indicate stretching cells, which open the cap by the induced mechanical force. These images do however not reflect the quantitative water distribution of the mushroom and the contrast fluid.

6.3 Suggestions for future research

NMR/MRI offers an interesting option for a continuation of this mushroom study. Since NMR/MRI quantifies the water distribution in fruitbodies (5) and a relation between the observed relaxation times and the cellular geometry could be established (3,4). Especially this last finding is interesting when cell stretching is the topic of further research. Imaging of the self diffusion of water is expected to provide a contribution to such a study because it visualises the differences in self-diffusion of water molecules, as affected by cellular compartment size and geometry. Since area's of stretching cells and dying cells are known to exist, diffusion contrast is expected to be influenced (8, 9).

The assignment of water pools to water in cellular compartments of the mushroom may provide location-specific information about the post-harvest physiology of the mushroom. The assignment can be accomplished by infiltration of mushrooms with contrast enhancing agents like Gd-DTPA or $MnCl_2$ with different membrane transport characteristics. The exchange rates of water and other compounds over the plasmalemma and the tonoplast can probably be determined from these experiments.

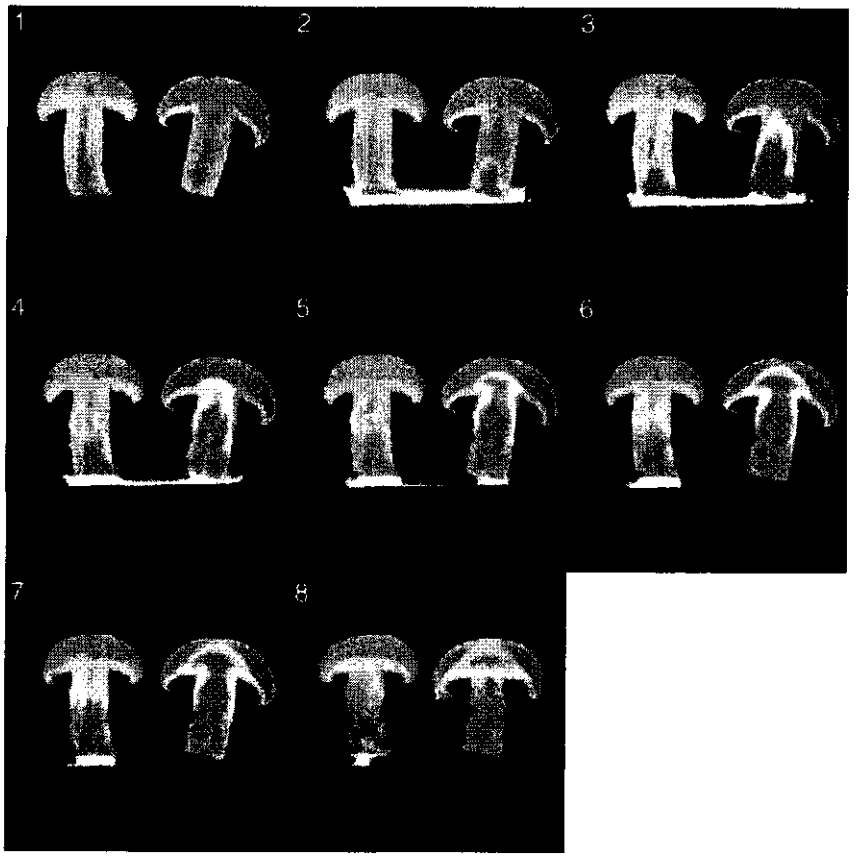

Figure 1, Uptake experiment with Gd-DTPA. Two mushrooms were placed with their cutting surface in a 70 mM Gd-DTPA solution and allowed to uptake the solution. The right mushroom was harvested 24 hours before the experiment and the left mushroom 10 min. Both mushrooms came from the same flight from the same crop. All images were acquired on a Bruker Biospec imager 47/40 (Bruker Medizin Technik GmbH, Rheinstetten, FRG) with Te = 6 ms, Tr = 103 ms and the total acquisition time = 4'24 min. Image 1 was recorded before placement in the solution and the images 2 to 8 respectively 0.5, 22, 44, 66, 88, 110 and 150 min after placement in the solution. The images demonstrate the uptake of the Gd-DTPA solution by both mushrooms with different speeds. The dried mushroom absorbs more solution than the fresh mushroom absorbs. The Gd-DTPA solution reduces T_2 first and T_1 afterwards (6, 7). This leads to enhanced signal intensity in the front of the Gd-DTPA stream and to reduced signal intensity at places where the Gd-DTPA has reached a maximum concentration. Remarkable are the two spots of enhanced signal intensity in the gill of the fresh mushroom at the end of the experiment. They might indicate a region with a higher osmotic potential, able to attract water in favour of other regions.

NMR can also be applied for the quantification of metabolites in parts of the mushroom. It should be noted however, that NMR is difficult at low concentrations of the observed compound. The difficulties with the susceptibility inhomogeneities were overcome (4) and are therefore not an impediment to further (water) ^{1}H-imaging of mushrooms. The imaging of other nuclei than ^{1}H becomes feasible after isotope enrichment, together with sensitivity improvement and elimination of susceptibility inhomogeneities. Mannitol in mushrooms is likely to be directly imaged with modern chemical selective imaging techniques, probably without isotope enrichment, but higher magnetic field strength will be required.

The last interesting option for a study of the role of mannitol in the mushroom can be the influence of magnetisation transfer on T_2 images. Since magnetisation transfer reduces T_2 of water protons near mannitol to undetectable low levels, the fraction of water, which is in the direct vicinity of mannitol, might be revealed. This provides an interesting option to monitor the mannitol distribution indirectly, synchronously with the water distribution and the relation between the two (10).

Summarising, it can be concluded that NMR has opened an interesting and promising new means to study the post-harvest physiology of mushrooms. The obtained information can be applied to define new quality parameters to the consumer product or to get a higher yield out of cultivars.

6.4 References

1) Flegg, P.B., Spencer, D.M. & Wood, D.A. (eds.); The Biology and Technology of the Cultivated Mushroom; John Wiley & Sons, Chichester (1985).

2) Donker, H.C.W. & Braaksma, A.; Changes in metabolite concentrations detected by ^{13}C-NMR in the senescing mushroom (Agaricus bisporus); Postharvest Biol. Techn. (1997); 10: 127-134.

3) Donker, H.C.W., Van As, H., Edzes, H.T. & Jans, A.W.H.; NMR Imaging of white button mushroom (Agaricus bisporus) at various magnetic fields; Magn. Reson. Imag. (1996); 14: 1205-1215.

4) Donker, H.C.W., Van As, H., Snijder, H.J. & Edzes, H.T.; Quantitative ^{1}H-NMR imaging of water in white button mushrooms (Agaricus bisporus); Magn. Reson. Imag. (1997); 15: 113-121.

5) Donker, H.C.W. & Van As, H.; Cell water balance of white button mushrooms (Agaricus bisporus) during its post-harvest lifetime studied by quantitative magnetic resonance imaging; Biochim. Biophys. Acta gen. sub. (1999); 1427: 287-297.

6) Ilg, M., Maier-Rosenkranz, J., Müller, W. & Bayer, E.; Magnetic resonance imaging in reversed-phase liquid chromatography; J. Chromatography (1990); 517: 263-268.

7) Ilg, M., Maier-Rosenkranz, J, Müller, W., Albert, K. & Bayer, E.; Imaging of the chromatographic process; J. Magn. Reson. (1992); 96: 335-344.

8) Umar, M.H. & Van Griensven, L.J.L.D.; Morphological studies on the life span, developmental stages, senescence and death of fruit bodies of *Agaricus bisporus*; Mycol. Res. (1997); 101: 1409-1422.

9) Braaksma, A., Doorn, A.A. van, Kieft, H. & Aelst, A.C. van; Morphometric analysis of ageing mushrooms (*Agaricus bisporus*) during postharvest development; Postharvest Biol. Techn. (1998); 13: 71-79.

10) Callaghan, P.T.; Principles of Nuclear Magnetic Resonance Microscopy; Clarendon Press, Oxford, (1991).

SUMMARY

The objective of the study described in this thesis was to explore the potentials of NMR for the study of water relations in harvested mushrooms (*Agaricus bisporus*). Since harvested mushrooms tend to continue their growth after harvest, their morphogenesis is heavily influenced by the external climatic conditions. Their respirative resources as well as their internal water can not be replenished after harvest and has therefore to be present in the mushroom before harvest.

The main metabolic pools and changes in these pools were studied in Chapter 2. Extracts of the cap, gill and stipe of the fruiting body of the mushroom (*Agaricus biporus*) were studied by ^{13}C-NMR spectroscopy. This technique enables changes in the main metabolite pools to be studied simultaneously as a function of storage time, temperature and postharvest development. An earlier reported reduction in dry weight of the stipe could be explained by a decrease in mannitol content. At 274 K storage temperature no postharvest development occurred, yet mannitol content decreased. It was concluded that mannitol is probably used as a respiratory substrate in gill tissue. Proteolytic breakdown was apparent, even during storage at 274 K, but occurred preferentially in the stipe. The products were most probably used by the gill and to a lesser extent by the cap to maintain metabolic activity as demonstrated by urea-cycle activity. Changes in the content of four amino acid pools (glutamate, glutamine, alanine and aspartate) proved to be tissue-specific, as were changes in the content of mannitol, fumarate and malate.

In Chapter 3, multi-echo imaging together with mono-exponential T_2 decay fitting was applied to determine reliable proton density and T_2 distributions over a mushroom. This was done at three magnetic fields strengths (9.4, 4.7 and 0.47 T) because susceptibility inhomogeneities were suspected to influence the T_2 relaxation times negatively and because the influence of susceptibility inhomogeneities increases with raising magnetic field strength. Electron microscopy was used to understand the different T_2's for the various tissue types in mushrooms. Large influences of the tissue ultrastructure on the observed T_2 relaxation times were found and explained. Based on these results, it was concluded that imaging mushrooms at low fields (around or below 0.47 T) and short echo-times has strong advantages over its high field counterpart, especially with respect to quantitative imaging of the water balance of mushrooms. These conclusions indicate to have general validity whenever NMR-imaging contrast is influenced by susceptibility inhomogeneities.

In Chapter 4, the influence of the tissue structure of mushrooms, e.g. tissue density (susceptibility inhomogeneity) and cell shape on the amplitude-, T_2- and T_1 images was analysed. This was achieved by vacuum infiltration of the cavities in the mushroom's spongy structure with Gd-DTPA solutions and acquiring Saturation Recovery-Multi Spin Echo images (SR-MSE images).

It was demonstrated that the intrinsic long T_2 values in the cap and outer stipe tissue strongly relate to the size and geometry of the highly vacuolated cells in these spongy tissues. All observed T_2 values were strongly affected by susceptibility effects. The T_2 of gill tissue was shorter than T_2 of the cap and outer stipe probably because these cells were less vacuolized and smaller in size.
The calculated amplitude images were not directly influenced by susceptibility inhomogeneities as long as the observed relaxation times remained sufficient long. They reflected the water distribution in mushrooms best if short echo-times were applied in a multi spin echo imaging sequence at low magnetic field strength.

In Chapter 5, the evolution and mechanism of redistribution of water in harvested mushrooms was studied using quantitative water density and T_2 MRI. It was revealed that when mushrooms did not lose water during the storage period, a redistribution of water occurred from stipe to cap and gills. When the storage condition resulted in a net loss of water, the stipe lost more water than the cap. The water density in the gill increased, probably due to development of spores.
Deterioration effects (i.e. leakage of cells, decrease in osmotic water potential) were found in the outer stipe. They were not found in the cap, even at prolonged storage at 293 K and R.H. = 70%. The changes in osmotic potential were partly accounted for by changes in the mannitol concentration. Changing membrane permeability's were indicated too. Cells in the cap had a constant low membrane (water) permeability. They developed a decreasing osmotic potential (more negative), whereas the osmotic potential in the outer stipe increased, together with the permeability of cells.

The NMR experiments described in this Thesis can find their future applications in the post-harvest quality control of mushrooms.

SAMENVATTING

Het proefschrift dat thans voor u ligt werd opgezet om de mogelijkheden van NMR bij de studie naar de waterverdeling in geoogste champignons (*Agaricus bisporus*) te onderzoeken. Omdat de ontwikkeling en de groei van de champignons zich voortzet na de oogst, worden deze eigenschappen beïnvloed door de externe klimaat omstandigheden tijdens het bewaren. Zowel de brandstof voorraad als ook de interne hoeveelheid water van de champignon kan niet meer aangevuld worden na de oogst vanuit het mycelium en moet daarom al voor de oogst in de champignon aanwezig zijn.

De belangrijkste metabolieten en de concentraties waarin zij aanwezig zijn werden onderzocht in hoofdstuk 2. Met ^{13}C-NMR spectroscopie werden extracten van de hoed, de steel en de lamellen onderzocht. In deze weefsels werd de concentratie van metabolieten onderzocht in relatie tot de bewaar periode, de bewaar temperatuur en de na-oogst ontwikkeling. Een afname van het drooggewicht in de steel werd bevestigd. Dit kon verklaard worden door een afname in de mannitol concentratie. Bij 274 K, werd geen na-oogst ontwikkeling waargenomen, toch nam de mannitol concentratie af. Waarschijnlijk werd mannitol gebruikt als brandstof in de lamellen. Zelfs bij deze lage bewaartemperatuur werd vermoedelijk afbraak van eiwitten waargenomen in de steel. De afbraakproducten dienden als brandstof voor de lamellen en in mindere mate voor de hoed. In deze twee weefsels werd activiteit van de ureum-cyclus waargenomen. Veranderingen in de concentraties van vier aminozuren (glutamine, glutamaat, alanine en aspartaat) bleken weefsel afhankelijk. Dit was ook het geval voor mannitol, fumarate en malate.

In hoofdstuk 3 wordt beschreven hoe multi-echo imaging met mono-exponentiele T_2 decay analyse gebruikt werd om betrouwbare proton-dichtheid afbeeldingen en T_2 afbeeldingen te verkrijgen van een champignon. Dit werd gedaan bij drie verschillende magneetveld sterktes (9,4 T, 4,7 T en 0,47 T) omdat susceptibiliteit inhomogeniteiten T_2 sterk doen afnemen bij hogere veldsterktes. Met behulp van elektronen microscopie werd de oorzaak van de grote T_2 afhankelijkheid onderzocht. Het bleek dat vooral de weefsel-ultrastructuur T_2 sterk beïnvloed. Daarom ging het afbeelden van champignons beter bij lage veldsterktes (0,47 T) met korte echotijden dan bij hogere veldsterktes en langere echotijden. Dit was vooral het geval wanneer kwantitatieve informatie over de waterverdeling in de champignon verlangd werd. Maar ook in het algemeen lijkt dit noodzakelijk te zijn wanneer MRI contrast sterk beïnvloed wordt door susceptibiliteit inhomogeniteiten.

In het hoofdstuk 4 werd de invloed van de weefselstructuur (weefsel dichtheid en cel-vorm) op de amplitude, T_1 en T_2 images onderzocht. Dit werd gedaan door de intercellulaire ruimtes te vacuum-infiltreren met een Gd-DTPA oplossing en vervolgens Saturation Recovery – Multi Spin Echo images (SR-MSE images) op te nemen. Het bleek dat de intrinsiek lange T_2 van de hoed en de buitenkant van de steel bepaald werd door de afmeting en de geometrie van de gevacuoliseerde cellen in dit

sponsachtige weefsel. Verder werden alle waargenomen T_2's sterk beïnvloed door magnetische susceptibiliteit effecten. De T_2 van de lamellen was korter dan de T_2 van de hoed en de steel. Dit is aannemelijk omdat deze cellen minder gevacuoliseerd en kleiner zijn.

In hoofdstuk 5 werd de ontwikkeling en het mechanisme van de water herverdeling in de geoogste champignon bestudeerd met behulp van kwantitatieve water-dichtheids- en T_2-afbeeldingen. Zelfs als de champignon in het geheel geen water verloor, werd toch een herverdeling van de steel naar de hoed en de lamellen aangetoond. Bij een overall verlies van water, verloor de steel meer water dan de hoed. Tegelijkertijd nam de weefseldichtheid in de lamellen toe, waarschijnlijk door de ontwikkeling van sporen.
Afstervingseffecten zoals het lekken van cellen en een afnemende osmotische waterpotentiaal werden aangetoond in de steel. Dit werd niet gevonden in de hoed; zelfs niet bij langere bewaartijden bij 293 K en een relatieve luchtvochtigheid van 70%. De veranderingen in osmotische potentiaal werden gedeeltelijk verklaard met veranderingen in de mannitol concentratie. Veranderende membraan permeabiliteiten zouden ook bijdragen aan de veranderingen in osmotische potentiaal. Cellen in de hoed hadden een constante lage water permeabiliteit. Hun osmotische potentiaal nam af (werd negatiever), terwijl de osmotische potentiaal van het weefsel in de buitenkant van de steel toenam (net als hun permabiliteit).

De NMR toepassingen die hier beschreven staan moeten bijdragen aan een beter begrip van de champignon. Naar verwachting vinden zij hun toekomstige toepassing in de kwaliteitscontrole van champignons.

CURRICULUM VITAE

Henk Cornelis Willem (Hank) Donker werd op 4 oktober 1964 te Haarlem geboren. Op 3 juni 1983 slaagde hij voor zijn eindexamen atheneum aan s.g. "De Amersfoortse berg" te Amersfoort. Na zijn eindexamen voer hij twee maanden als matroos aan boord van M.S. Lenneborg.

Op 28 augustus 1989 haalde hij zijn doctoraal examen chemie met als hoofdvak NMR spectroscopie bij prof. dr. R. Kaptein en als bijvakken fysisch-organische chemie, chemie didactiek en chemische informatica aan de Rijks Universiteit te Utrecht. Gedurende zijn studietijd vervulde hij diverse bestuursfuncties, zowel binnen de scheikunde faculteit als daar buiten.

In juni 1989 schreef hij een beleidsnota voor het Rijks Kwaliteits Instituut voor de Land- en Tuinbouw te Wageningen met als oogmerk te komen tot de oprichting van een NMR faciliteit binnen de Dienst Landbouwkundig Onderzoek. Aansluitend op deze nota adviseerde hij bij de aanschaf van een NMR spectrometer en schreef hij het projectvoorstel dat aan dit promotieonderzoek ten grondslag ligt.

Van 1 december 1989 tot 1 december 1993 was hij in dienst van de Landbouw Universiteit te Wageningen als AIO bij de vakgroep Moleculaire Fysica. Hij verrichtte daar het werk voor het proefschrift dat thans voor u ligt.

Na het vervullen van zijn militaire dienstplicht als pelotons commandant bij de 428ste infanterie beveiligings compagnie te Eefde kwam hij in dienst bij de Modulair Infogroep B.V. te 's-Hertogenbosch als programmeur annex systeem analist. Thans werkt hij bij Philips Medical Systems Nederland B.V. te Best als software engineer.

Naast zijn reguliere activiteiten is hij altijd een enthousiast scouting lid geweest in diverse staf teams voor diverse leeftijdsgroepen.